FFI PUBLICATION

A STUDY OF OBSERVED AND PREDICTED HF PROPAGATION CHARACTERISTICS AT HIGH LATITUDES

JODALEN Vivianne

19960404 006

A STUDY OF OBSERVED AND PREDICTED HF PROPAGATION CHARACTERISTICS AT HIGH LATITUDES

JODALEN Vivianne

FFI/PUBLICATION-96/01107

FORSVARETS FORSKNINGSINSTITUTT (FFI)
Norwegian Defence Research Establishment
P O BOX 25
N-2007 KJELLER, NORWAY

REPORT DOCUMENTATION PAGE

1) PUBL/REPORT NUMBER FFI/PUBLICATION-96/01107	2) SECURITY CLASSIFICATION UNCLASSIFIED	3) 168
1a) PROJECT REFERENCE FFIS/698/172	2a) DECLASSIFICATION/DOWNGRADING SCHEDULE	

4) TITLE

A STUDY OF OBSERVED AND PREDICTED HF PROPAGATION CHARACTERISTICS AT HIGH LATITUDES

5) NAMES OF AUTHOR(S) IN FULL (surname first)

JODALEN, Vivianne

6) DISTRIBUTION STATEMENT

Approved for public release. Distribution unlimited.
(Offentlig tilgjengelig)

7) INDEXING TERMS

IN ENGLISH:	IN NORWEGIAN:
a) HF radio propagation	a) HF radiobølgeforplantning
b) Ionospheric radio propagation	b) Ionosfærisk radiobølgeforplantning
c) Ionospheric absorption	c) Absorpsjon i ionosfæren
d) Predictions	d) Prediksjoner
e) Above-the-MUF propagation	e) Frekvensvarsling

THESAURUS REFERENCE:

8)   ABSTRACT

Prediction programmes at HF serve as tools for system design, frequency management and daily operations of communication systems. Models used in the prediction programmes of radio propagation through the high latitude ionosphere have relied on extrapolation from low latitudes, and they are inconsistent and incorrect.

An HF oblique incidence ionospheric sounder has been developed at FFI and data recorded on one auroral path (285 km) and one sub-auroral, mid-latitude path (1230 km) within Norway. The database contains several years of measurements around sunspot maximum, and it describes the effects of seasonal variations and different degrees of geophysical disturbances.

9) DATE 29 February 1996	AUTHORIZED BY This page only Nils Holme	POSITION Director General

FFI-B-22-1982

Abstract continued.....

Measured reliability of the channel and virtual height of reflection of the signals have been compared with predictions from ICEPAC for different seasons and levels of geomagnetic activity.

For the short auroral path, the prediction of reliability is too optimistic compared with data, and ICEPAC fails to predict the observed diurnal variation of reliability during geomagnetically disturbed periods. Predicted reliability at frequencies above the MUF is also too large compared with measured reliability.

For the longer sub-auroral/mid-latitude path, the discrepancy between data and predictions is unexpectedly larger than for the short auroral path. ICEPAC predicts this path to be entirely a mid-latitude path, whereas the data show both auroral and mid-latitude characteristics.

We suggest two modifications to the prediction programme in order to improve the performance of the programme for auroral paths:

- To incorporate a high-latitude D-region electron density model controlled by measured riometer absorption, and calculate the integrated absorption along a specific path using the Appleton-Hartree equation.

- To implement a method of calculating reliability that explicitly uses the probability of an ionospheric mode being present.

A significant improvement in the prediction of reliability has been achieved. The D-region model gives enhanced absorption at the lowest frequencies, particularly during disturbed conditions. The observed variation of absorption with time of day is now reflected in the predictions. The variation of absorption now reflects the pattern of particle precipitation from the magnetosphere. The new method of predicting absorption opens the possibility for exploiting the large existing global database of riometer absorption.

The explicit use of mode availability reduces the predicted reliability for frequencies close to the MUF considerably, in agreement with observations. We believe that above-the-MUF propagation is over-estimated in ICEPAC.

The two suggested modifications have not led to any improvement of predicted virtual height of reflection.

PREFACE

The purpose of the project has been to collect HF channel data on high-latitude oblique incidence paths over a period of several years. Data were recorded during the years 1987 to 1992, and data analysis carried out from 1990 to 1995. This report contains the main results of the analysis.

CONTENTS **Page**

A STUDY OF OBSERVED AND PREDICTED HF PROPAGATION CHARACTERISTICS AT HIGH LATITUDES

1 INTRODUCTION AND OUTLINE

The high frequency (HF) band (3-30 MHz) has traditionally been used for long distance radio communication because of the reflecting properties of the ionosphere. The ionosphere is a natural resource that is always present, but its dynamics and variability makes it a difficult and unstable propagation medium. Knowledge of ionospheric behaviour and trained operators have been absolutely necessary in order to communicate efficiently. Observations and theoretical work have led to models of the ionosphere as well as models of the propagation of radio waves via the ionosphere. The models have been combined in HF prediction programmes that serve as a daily aid for the radio operators, and they also give important guidelines in frequency management and in the design of HF radio equipment.

New techniques in HF communications, partly employed and partly under development, include real-time channel evaluation (RTCE) and automatic radio communication systems (ARCS). These advanced technologies will ease the work of the radio operator by automatically sounding the channels, selecting a channel and establishing communications.

In spite of the development of other efficient techniques for long-distance communications such as satellite communication and microwave links, military users in particular still have a strong interest in HF because of its reliability in times of conventional war. Efficient use of this natural resource will also in the future depend on the reliability of good models used in the design of equipment and in frequency management. The low and middle latitude ionosphere has been studied for many years, and a large, reliable data base exists. This database, together with physical models of the ionospheric layers, has made it possible to construct quite efficient prediction programmes for these latitudes. Developing good models have been difficult in polar regions where the medium is extremely variable in time and space. The ionosphere beyond 60 degrees north or south is strongly influenced by geophysical disturbances originating in the solar atmosphere and the Earth's magnetosphere. The highly complex physical mechanisms here are not fully understood. The polar regions are also not easily accessible, and as a consequence there is a lack of reliable observations. Up to now, the prediction programmes have relied upon extrapolation from middle to high latitudes, and experience shows that their performance is often poor in polar regions. ICEPAC (Ionospheric Communications Enhanced Profile Analysis and Circuit Prediction Program, Stewart (1)) represents a further developement of IONCAP (Ionospheric Communications Analysis and Prediction Program, Teters et al (2)), which in turn is the

culmination of several earlier prediction programmes developed by ITS (Institute of Telecommunication Sciences) in Boulder. ICEPAC contains a high latitude model, and was created in order to improve the predictions in the high-latitude and polar regions.

The NDRE has implemented a series of HF propagation tests in Norway, taking advantage of the fact that the auroral oval most of the time crosses the northern part of Norway. In 1987 an ionospheric oblique incidence sounder was deployed in the north of Norway in collaboration with the Naval Undersea Warfare Center-division Newport, Connecticut. Data was recorded across the HF-band for about five years around sunspot maximum. The aims of this experiment were to obtain a statistical description of the properties of ionospheric communication channels at high latitudes and to use these results in the evaluation and possible improvement of existing prediction programmes. IONCAP/ICEPAC was chosen as the prediction programme to be evaluated, and a collaboration with ITS initiated. This report gives the results from the evaluation, and suggests further improvements to the high latitude model that incorporate features observed in the experimental data.

Preliminary results from this study have been published in Jodalen and Thrane (3), (5) and (6) and Thrane et al (4). The preliminary results showed that large discrepancies between data and predictions exist in the modelling of radio wave absorption, and that absorption at high latitudes should be modelled as a function of geomagnetic activity. This work thus concentrates on incorporating a new method for calculating ionospheric absorption appropriate for high latitudes in ICEPAC. A review of selected aspects of ionospheric propagation and absorption is given in Chapter 2, and Chapter 3 discusses the influence of geomagnetic activity on HF communications. Chapter 4 presents basic principles of prediction programmes with emphasis on the implementation in ICEPAC. The HF test experiment is described in Chapter 5, and observations from the experiment are compared with ICEPAC predictions in Chapter 6. The performance of the prediction programme is discussed in the same chapter. A new high latitude absorption model developed by Friedrich and Torkar (7) is introduced in Chapter 7 as well as a revision of the propagation modelling. The new absorption model and propagation model is incorporated into ICEPAC, and new predictions are compared with our experimental data in Chapter 8. Finally, conclusions are drawn in Chapter 9.

2 SELECTED ASPECTS OF RADIO WAVE PROPAGATION

We assume that the reader has basic knowledge of HF communications, such as formation of the regular ionized layers in the ionosphere and the reflecting properties of the layers at radio frequencies below 30 MHz. We nevertheless describe a few aspects of HF communications that will be used and referred to throughout this work.

2.1 Heights of reflection

In an anisotropic medium such as the ionosphere, the energy of a radio wave may propagate in a different direction from that of the phase propagation (Davies (8), Goodman (9)). The wavelength λ, the phase speed v_p, and phase refractive index μ, refers to the direction of phase propagation. The packet velocity u is defined in the direction of energy propagation, and its velocity component along the phase propagation direction is called the group velocity v_g. The phase and group refractive indices are given respectively as

$$\mu = \frac{c}{v_p} \qquad \text{and} \qquad \mu' = \frac{c}{v_g} \tag{2.1}$$

The phase path P is defined as the distance in free space required to produce a given phase change φ. The phase path between points S and E is given as

$$P = \int_S^E \mu \cdot \cos\alpha \cdot ds \tag{2.2}$$

where α is the angle between the directions of phase propagation and energy propagation. The time of flight T_g of a wave packet travelling from S to E is found by integrating the inverse packet velocity:

$$T_g = \int_S^E \frac{ds}{u} = \int_S^E \frac{1}{v_g} \cdot \cos\alpha \cdot ds \tag{2.3}$$

The corresponding group path P' is

$$P' = c \cdot T_g = \int_S^E \mu' \cdot \cos\alpha \cdot ds \tag{2.4}$$

The arrival time of energy (T_g) is detected in time-of-flight measurements, and the corresponding group path calculated. Neither phase paths nor group paths represent real paths, only times of transit. The group height (virtual height) h' of a signal transmitted vertically and reflected is:

$$h' = \tfrac{1}{2} \cdot c \cdot T_g = c \cdot \int_0^{h_r} \tfrac{1}{v_g} \cdot dh = \int_0^{h_r} \mu' \cdot dh \qquad (2.5)$$

where h_r is the true height of reflection. Given a model electron density profile and the transmitted frequency, h_r and the μ' profile can be determined. The calculation of virtual height is normally simplified by assuming no magnetic field and no collisions between electrons and neutral particles.

Given these assumptions, three important laws give the relationship between vertical and oblique incidence propagation in a horizontally stratified ionosphere on a plane Earth:

The secant law states that the relationship between two frequencies reflected at the same true height, one with an angle of incidence φ on the ionosphere, the other reflected vertically, is given by $f_o = f_v \sec \varphi$.

Breit and Tuve's theorem states that the time required for a wave to propagate on an oblique path is the same as the time required to traverse a virtual triangular path at the free space speed of light.

Martyn's equivalent path theorem says that two frequencies fulfilling the secant law have the same virtual (group) height of reflection.

For accurate calculations, the curvature of the ionosphere and the Earth's magnetic field must be taken into account, and these laws require correction terms.

2.2   Sporadic E-layers

Sporadic E-layers are irregular layers occuring in the height interval 90-120 km. They are highly variable in time and space, and the critical frequency f_oE_s varies between 2 MHz and 30 MHz. Worldwide maps of f_oE_s exist that show the rate of occurence depending on location, season and time of day. In the auroral region, E_s is a night phenomenon independent of season. At mid-latitudes E_s occurs more often in summer than in winter and slightly more during day than during night. In the equatorial zone, the occurence of sporadic E is very large around noon for all seasons and is considered to be a regular feature of the ionosphere.

The nature of sporadic E-layers is not known in detail, and it is believed that several physical phenomena are the cause of sporadic E. Auroral sporadic E is produced by precipitating particles from the magnetosphere, and ionizing meteors and wind shears are suggested as the cause of other types of E_s. (Davies (8)).

2.3   Sub-auroral trough

The sub-auroral trough (Halcrow and Nisbet (10)) is a region of sharply decreased electron densities at F_2 heights situated 2-10 degrees equatorward of the auroral oval. The extention of the region and the amount of depletion is determined by the magnetic local time and geomagnetic activity. The trough exists at night, and the f_oF_2 is reduced with increasing geomagnetic activity. Thus, the MUF on a particular path may be reduced, and off great circle propagation may occur. One explanation of the trough region is a "mapping" of the plasma pause onto the ionosphere along magnetic field lines on the night side of the Earth (Rycroft and Thomas (11)).

2.4   Radio wave loss mechanisms

The attenuation of radio waves is caused by three basic mechanisms. First, the wave attenuates as $(D/\lambda)^2$ where D is path length and λ is wavelength, as the wave propagates away from the source. This is the basic free space loss (50-200 dB). Secondly, ground conductivity is important also in ionospheric communication. The ground conductivity influences the performance of the antennas, and on multiple-hop paths, the ground reflection will cause additional loss if the ground conductivity is poor. This is a relatively small loss (1-10 dB). Thirdly, the interaction of a radio wave with the ionospheric plasma and the neutral atmosphere gives ionospheric loss (50-200 dB). We will focus attention on ionospheric loss in this work, but also include other loss terms in the calculations where appropriate.

There exist several other loss mechanisms that are difficult to quantify. Examples are: focusing loss, losses due to sporadic-E, polarization mismatch loss, above-the-MUF loss and losses due to fading. These loss terms are often added and estimated as one excess system loss term. Above-the-MUF loss will be briefly described in Section 4.3.2.

2.5   Ionospheric loss - the Appleton Hartree equation

The phase refractive index μ of a medium is defined as the ratio between the phase speed of an electromagnetic wave in free space and in the medium, $\mu=c/v_p$. The wave polarization R of an electromagnetic wave is defined as the ratio between the electric field components E_x and E_y in a plane perpendicular to the direction of propagation $\vec{k}$, $R=E_x/E_y$. Both μ and R are normally defined as complex quantities. Assuming a set of properties of the radio wave and of the plasma, Appleton and Hartree developed a magnetoionic theory which describes the propagation of an electromagnetic wave in a cold plasma (Ratcliffe (12)). The theory describes the complex refractive index n of the medium, and the complex wave polarization R as a function of electron density N_e,

angular frequency ω, gyrofrequency ω_H, magnetic field B, and collision frequency ν. The theory is expressed in the form of two equations:

$$R = \frac{i}{2Y_L}\left[\frac{Y_T^{2}}{1-X-iZ} \mp \sqrt{\frac{Y_T^{4}}{(1-X-iZ)^2}+4Y_L^{2}}\right] \qquad (2.6)$$

$$n^2 = 1 - \frac{X}{1-iZ-\dfrac{Y_T^{2}}{2(1-X-iZ)} \pm \sqrt{\dfrac{Y_T^{4}}{4(1-X-iZ)^2}+Y_L^{2}}} \qquad (2.7)$$

where

$$X = \frac{N_e e^2}{\varepsilon_0 m_e \omega^2}, \qquad Z = \frac{\nu}{\omega}$$

$$\vec{Y} = \frac{e\cdot\vec{B}}{m_e\cdot\omega}, \qquad |\vec{Y}| = \frac{\omega_H}{\omega}$$

$$Y_T = \frac{eB_T}{m_e\omega}, \qquad Y_L = \frac{eB_L}{m_e\omega}$$

B_L and B_T are components of the magnetic field parallell to, and perpendicular to $\vec{k}$, respectively.

The two signs in the equations refer to the two different characteristic waves that can propagate in the medium. The influence of the medium on each of them is different, e.g. refraction and absorption. Under certain conditions, the equations can be simplified. If we assume that the direction of propagation is almost parallel to the magnetic field B, $Y_T \approx 0$, and the refractive index can be expressed as:

$$n^2 = (\mu - i\chi)^2 = 1 - \frac{X}{1 \pm Y_L - iZ} \qquad (2.8)$$

This is a good approximation if the angle between the B-field and the wave normal k is less than 40°. For HF communications this situation applies particularly well for long distance propagation along the magnetic meridians and also for propagation over short paths at high latitudes where the magnetic field is almost vertical.

Assuming that the direction of propagation is in the z-direction and assuming that the medium does not vary over the wavelength, the electric field of a plane wave $\left(\frac{\partial}{\partial x} = \frac{\partial}{\partial y} = 0\right)$ can be expressed as:

$$\vec{E} = \vec{E}_0 \cdot e^{i(\omega t - kz)} \qquad (2.9)$$

k is defined as a complex wave number $k = k_r - i\kappa$ in the direction of z that is related to the complex refractive index $n = \mu - i\chi$ through $n = k/k_0$. k_0 is the wave number in free space (real). Substituting $k = k_0(\mu - i\chi)$ into equation (2.9), we obtain:

$$\vec{E} = \vec{E}_0 \cdot e^{-k_0\chi z} \cdot e^{i(\omega t - k_0\mu z)} \tag{2.10}$$

The same equation will be obtained by inserting $k = k_r - i\kappa$:

$$\vec{E} = \vec{E}_0 \cdot e^{-\kappa z} \cdot e^{i(\omega t - k_r z)} \tag{2.11}$$

The E-field is expressed as a product of two factors; one factor describing an exponential decay of the amplitude, the second factor describing a harmonic wave propagating in the z-direction of a medium with a real refractive index μ. κ is the attenuation per unit distance in the direction of the wave number k, and is refered to as the *absorption index:*

$$\kappa = k_0 \cdot \chi \tag{2.12}$$

Looking at the real and imaginary parts of Equation (2.8) separately, the imaginary part can be written:

$$2\mu\chi = \frac{X \cdot Z}{(1 \pm Y_L)^2 + Z^2} \tag{2.13}$$

The attenuation of the wave per unit distance can be expressed as:

$$\kappa = \frac{k_0}{2\mu} \cdot \frac{X \cdot Z}{(1 \pm Y_L)^2 + Z^2} \tag{2.14}$$

$$\kappa = \frac{e^2}{2\varepsilon_0 mc\mu} \cdot \frac{N \cdot \nu}{(\omega \pm \omega_L)^2 + \nu^2} \tag{2.15}$$

The total ionospheric loss is found by integrating the absorption index κ along the ray path:

$$L_i = 4.6 \cdot 10^{-2} \int_s \frac{1}{\mu} \cdot \frac{N \cdot \nu}{(\omega \pm \omega_L)^2 + \nu^2} \quad \text{[dB]} \tag{2.16}$$

The physical processes behind this loss equation is as follows: As the radio wave propagates through the plasma, the electric field of the wave causes electrons to vibrate, and collisions with neutral particles cause dissipative attenuation of the radio wave. Appleton and Ratcliffe (13) have shown that the main part of the ionospheric absorption occurs in the D-region (60-95 km) well below the reflection level. In this region $\mu \approx 1$ and the absorption resulting from (2.16) is called *non-deviative.* Near the point of reflection, $\mu < 1$, and ray bending occurs. *Deviative* absorption (Piggott et al (14)) occurs whenever significant ray bending takes place, but at oblique incidence of the radio wave, reflection occurs at a non-zero value of μ and deviative absorption is less important.

2.6   Generalized magneto-ionic theory

The Appleton-Hartree magneto-ionic theory implicitly assumes that the collision frequency ν between electrons and neutral particles is independent of electron energy. Laboratory measurements (Phelps and Pack (15)) have shown that the collision frequency in nitrogen is proportional to the electron energy. Taking this fact into account, a generalized formula for the refractive index has been derived (Sen and Wyller (16)). The formula integrates over all possible electron velocities in a Maxvellian distribution, using the relationship $\nu \propto v^2$.

Both theoretical work and experiments (Thrane and Piggott(17)) show that collision frequency is proportional to atmospheric pressure p in the height range 50-100 km. The relation

$$\nu_M = 6.34 \cdot 10^5 \cdot p \quad \left[\tfrac{1}{s}\right] \tag{2.17}$$

can be deduced for an atmosphere with 78% nitrogen and 20.9% oxygen (Thrane (18)). ν_M is the average collision frequency of electrons with energy kT. The mean collision frequency for electrons in a weakly ionized gas is given as:

$$\overline{\nu} = \tfrac{3}{2} \cdot \nu_M \tag{2.18}$$

The Sen and Wyller theory gives a more accurate description of radio wave propagation in the lower ionosphere. The Appleton-Hartree theory is a good approximation in two limiting cases, provided that the proper value of the collision frequency ν_{AH} is being used (Molmud (19)):

$$\tfrac{\overline{\nu}}{\omega} << 1 \qquad \nu_{AH} = \tfrac{5}{2} \cdot \nu_M = \tfrac{5}{2} \cdot 6.34 \cdot 10^5 \cdot p \tag{2.19}$$

$$\tfrac{\overline{\nu}}{\omega} >> 1 \qquad \nu_{AH} = \tfrac{3}{2} \cdot \nu_M = \tfrac{3}{2} \cdot 6.34 \cdot 10^5 \cdot p \tag{2.20}$$

At high frequencies (3-30 MHz), the angular frequencies are in the range 10^7-10^8 rad/s, and the mean collision frequencies $\overline{\nu}$ in the D-region attain values from 10^7-10^5 Hz. As an example, for f=7 MHz and p=17.27 N/m² (CIRA (20)) at a height of 60 km at 70° north, the ratio $\overline{\nu}/\omega$ is 0.37. This means that for the high frequencies 3-10 MHz, the limiting case (2.19) does not apply particularly well in the lowest part of the D-region (60-75 km). The generalized theory should therefore be used for these frequencies and heights. However, referring to Figure 3 in Barrington and Thrane (21), the error in the calculation of absorption at 2 MHz by using the Appleton-Hartree equation with $\nu_{AH}=5/2 \cdot \nu_M$, can be shown to be less than 30% for the ordinary wave and less than 24% for the extraordinary wave at an altitude of 60 km. Depending on the altitude, the Appleton-Hartree formula overestimates or underestimates the absorption compared to the generalized formula.

2.7   Measuring absorption

Ionospheric absorption can be measured using different methods.

The A1-method utilizes frequencies below f_oF_2. It transmits a pulse vertically and measures the virtual height of reflection and amplitudes of the signal reflected once, twice and so forth from the ionosphere. The effective reflection coefficient of the combined ionospheric and ground reflections is determined from the amplitude measurements. Knowing the ground characteristics, the ionospheric reflection coefficient can be found which gives the relationship between transmitted and received power for one ionospheric reflection. The absorption is then determined.

The A3-method transmits a continous wave over a short oblique incidence path and records the field strength at the receiver. The method can not discriminate between echoes from different heights so normally a low frequency is selected that will be reflected once from the E-layer. Frequencies near the gyrofrequency are preferred, because the contribution to the signal strength from the extraordinary wave then will be small.

The f_{min}-method takes the minimum frequency observed on an ionogram as a rough measure of non-deviative absorption.

The A2 (or riometer)-method will be described a little more in detail. The riometer (relative ionospheric opacity meter) measures (at one particular frequency) the power of cosmic radio signals (wideband noise) that impinges on the Earth from the galaxy. This is a self-calibrating instrument for measuring variations in the cosmic radio noise level. With a directive antenna, the rotation of the Earth will provide a scanning of the sky which will give a variation of the received noise power with sidereal time when no disturbance is present (quiet day value). The quiet day curve also depend weakly on solar time through the background absorption of the undisturbed D-region. The absorption measured by the riometer, L_r, is the ionospheric absorption encountered when a disturbance is present, in addition to the quiet day value. The riometer absorption can be expressed as:

$$L_r = 10 \cdot \log \frac{J_q}{J} \tag{2.21}$$

where J is the recorded current proportional to the received power and J_q is the quiet day value. The measured ionospheric absorption is a decreasing function of frequency. The operating frequencies of a riometer are typically 20-50 MHz and absorption changes of about 0.1 dB can be measured. This frequency range has been chosen in order to ensure penetration of the ionosphere and to avoid measuring deviative absorption at lower frequencies. The absorption below 50 MHz is still measureable.

The different methods of measuring absorption use different ranges of frequencies. They are therefore sensitive to absorption in different height regions and might give slightly different results when compared (Ranta (22)). The A1 and A3-methods have been used extensively over the years to map the global morphology of absorption. The A2-method is a less accurate method since it measures only the deviation from the quiet day curve at a relativly high frequency. Large disturbances are required to produce an increase of riometer absorption. Thus the A2-method is best suited to measure absorption at high latitudes where large disturbances frequently occur.

2.8   Morphology of absorption

The morphology of absorption has been studied thoroughly over the years, and large, global databases exist. Absorption varies in a complex manner with latitude, longitude, time of day, season, sunspot number and geomagnetic activity. A review article on the topic is given by Thrane (23), and other literature is for instance George (24), Piggott (25) and Ranta (22).

Non-deviative (nd) ionospheric absorption at high frequencies is roughly proportional to $(\omega \pm \omega_L)^{-2}$ as can be seen from equation (2.16). This fact can be used to identify this type of absorption. The non-deviative ionospheric absorption is also proportional to $\int N \cdot \nu \, ds$, where N shows diurnal, seasonal and latitudinal variations, and ν shows seasonal and latitudinal variations. We shall discuss the most important mechanisms behind ionospheric absorption, and the resulting observed morphology.

2.8.1   Ionization and absorption caused by electromagnetic radiation

X-rays, UV and certain lines in the electromagnetic spectrum such as H-Lyman-α and H-Lyman-β cause ionization from 60 km to 500 km altitude. In the D-region where most of the absorption occurs, the main sources of ionization are X-rays ($\lambda < 10nm$) in the upper D-region, and H-Lyman-α ($\lambda = 121.6$ nm) in the lower D-region. O_2^+ and NO^+ are the most important ions formed in the higher D-region, and heavy cluster-ions such as $H^+(H_2O)_n$ exist in the lower D-region. Negative ions (O_2^-) are also formed in the lower D-region by reactions between electrons and neutral molecules.

The electron content of the D-region is determined by the ion production rate, recombination and transport of electrons by the dynamics of the atmosphere. When the sun rises (solar zenith angle decreases), the ion production rate increases, and absorption reaches a maximum around local noon. The density of negative ions decreases. Models of the ion production and recombination processes in the D-region (Thrane (26)), have been compared with observations and the dependence of HF absorption on solar zenith

angle χ has been determined to be $\cos^n\chi$, where n varies from 0.8 for small χ to 0.2 for large χ. At sunrise and sunset, the ionization of NO by H-Lyman-α will be the dominant source of ionization in the D-region. As the solar zenith angle decreases towards noon, the relative influence of solar X-rays and H-Lyman-β ($\lambda=102.5$ nm) will soon dominate the ionization process and cause an increase of n.

The latitudinal variation of the D-layer absorption can be explained in a similar way; at high latitudes, the solar zenith angle always remains large, and rapid increase of ionization by X-rays and H-Lyman-β never occurs (n remains small) (George (24)). In addition, the collision frequency varies with latitude according to global dynamic systems.

Absorption increases with increasing sunspot numbers because of increased fluxes of solar UV and X-rays.

There are basically three causes of seasonal changes of absorption: The solar zenith angle, the collision frequency and the density of NO in the D-region. At mid-latitudes global transport causes increased density of NO during winter which gives increased electron density and considerably increased absorption (winter anomaly). Possible explanations of the winter anomaly have been published in JATP (27), Thrane et al (28), and Thomas (29).

George (24) found, by studying absorption data at different geomagnetic locations, that there exists a geomagnetic control of the ionospheric absorption.

Solar flares are frequent around the peaks of sunspot cycles. They are characterized by increased radiation of wavelengths ranging from radio to X-rays. The larger flares cause sudden disturbances of the ionosphere (SID's), which gives increased absorption over the sunlit hemisphere where the solar radiation is the dominating source of ionization.

2.8.2   Ionization and absorption caused by particle precipitation

Precipitating electrons and protons from the solar wind is another source of ionization in the ionosphere. Coronal holes with open magnetic field lines on the sun cause a variable flux of particles. The energy of the particles ranges from a few keV to tens of MeV. They penetrate down to Earth through the cusp on the day side and from the magnetotail down to the auroral zones on the night side. Figure 2.1 (Hartz (30)) shows the spatial distribution of precipitating particles with energies from below 1 keV to above 40 keV.

Particle precipitation at high latitudes often completely masks the variations of ionization caused by solar radiation. It is a dominating source of ionization at night at latitudes beyond geomagnetic latitude 62°. The high latitude ionosphere is considered to be constantly disturbed, characterized by sporadic-E layers, visible aurora, magnetic activity

and large and variabel absorption. Various disturbances associated with particle precipitation have been discussed by Thrane (28), (23).
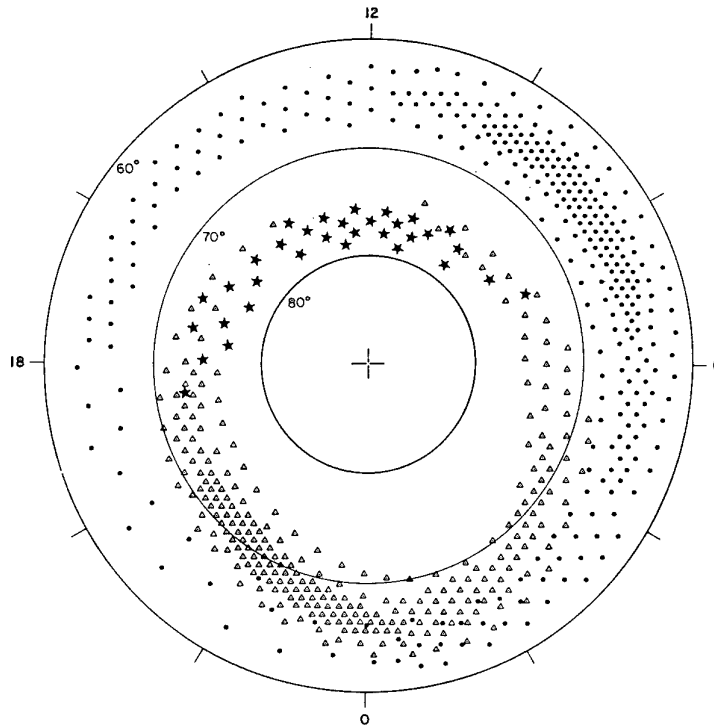
Figure 2.1   Particle precipitation pattern. Low energy precipitation (<1 keV) represented by stars, medium energy precipitation (1 keV - 40 keV) by triangles and high energy precipitation (>40 keV) by dots. Average flux is indicated by the density of the symbols. Coordinates are geomagnetic latitude and geomagnetic time (Hartz (30))

Two important types of absorption events at high latitudes should be mentioned:

A PCA (Polar Cap Absorption Event) is associated with major solar flares, and is very destructive for communication on frequencies in the HF band. During a PCA, high energetic solar protons (>10 MeV) impinges on the polar atmosphere causing the ion production rate to increase by orders of magnitude over the entire polar cap. Riometer absorption of 10-20 dB can be observed.

Auroral absorption occurs more frequently than PCA's. Auroral absorption is initiated by the solar wind causing magnetospheric disturbances. Energetic electrons (10 keV-300 keV) penetrate to the D and lower E region. Figure 2.2 shows the occurence probability of auroral absorption in the northern hemisphere for equinox and high sunpot activity (Holt (31)). Note that at 65°N and 08 geomagnetic time the absorption is maximum with a 34 % probability that the absorption exceeds 0.5 dB at 30 MHz. This would give considerably absorption at HF frequencies. Figure 2.2 will change slightly according to season and magnetic activity (Ranta (22)).
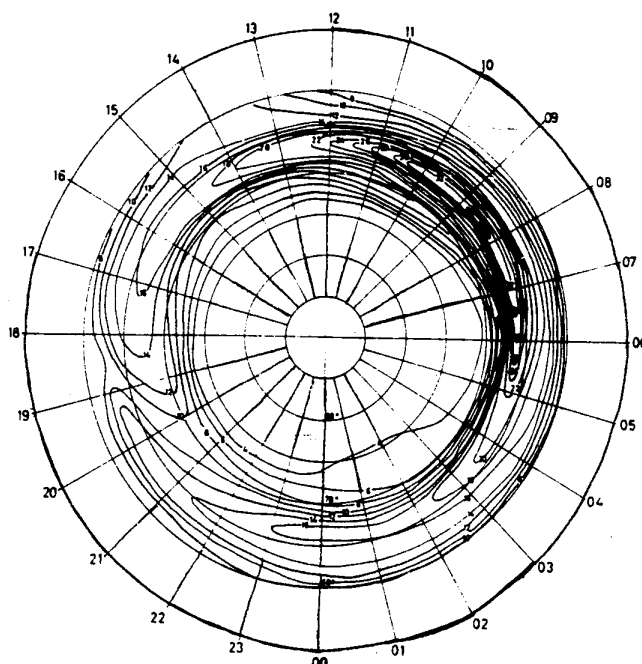
*Figure 2.2   Auroral absorption, percentage of total time with absorption exceeding
0.5 dB at 30 MHz as a function of geomagnetic time and latitude during
equinox months. Maximum solar activity (Holt (31))*

2.8.3   Observed variations of absorption at high latitudes

Ranta (22) has compared measurements of absorption from five riometer stations in
Finland at geographic latitudes from 60°N to 70°N and longitudes from 24°E to 27°E.
She has also compared the measurements with those of other authors and found
consistency. Since the HF experiment described in this work (Chapter 5) took place in
Norway at about 69°N and 16°E to 24°E, we feel that some of her conclusions from the
Finnish measurements are of importance to this work.

Figure 2.3 illustrates the diurnal variation of absorption in spring for the five riometer
stations. At high latitudes, between geomagnetic latitudes 62° and 77° there are two
diurnal absorption maxima, one in the morning and a smaller maximum around midnight.
An absorption minimum exists in the late afternoon. An explanation might be found in
Figure 2.1 showing that the precipitation of particles with energies above 40 keV
maximizes at geomagnetic latitudes 65-70° from 8 to 10 geomagnetic time. The
precipitation of particles with energies 1-40 keV maximizes from 21 to 00 geomagnetic
time.

Other observations in Ranta (22) are:

At latitudes below 62°, there is one day maximum around noon. At latitudes beyond 77°,
there is one night maximum.
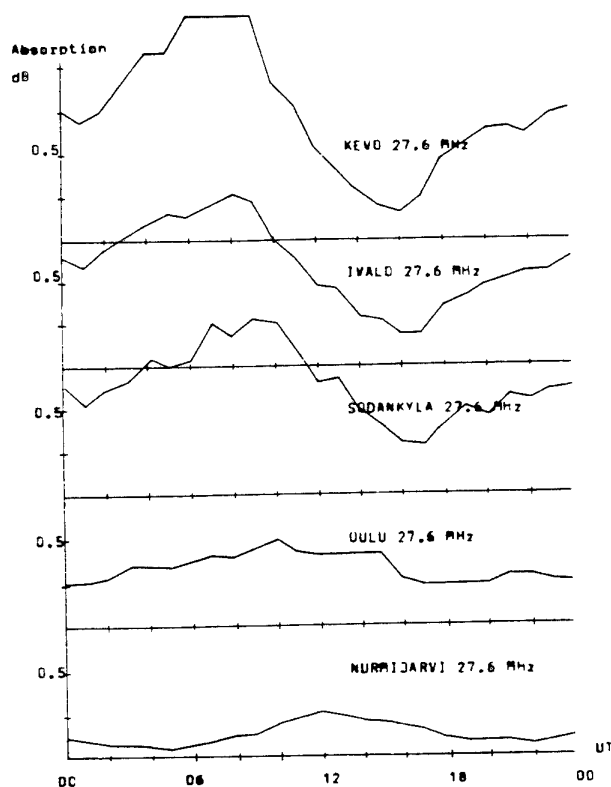
Figure 2.3 Diurnal variation of absorption during spring observed at the five Finnish riometer stations from Kevo at 69°N (geographic) to Nurmijärvi at 60°N (Ranta (22))

The two maxima at latitudes 62°-77° are more pronounced during equinox than during summer and winter.

The morning and midnight maxima of absorption are approximately equal in summer and winter, whereas the morning maximum is almost twice as large as the night maximum at equinox.

Correlation between average yearly absorption and sunspot number exists at middle latitudes, but correlation is much better with geomagnetic activity at high latitudes.

Absorption in Norway is maximum at 67° geomagnetic latitude.

The time of maximum and minimum absorption in the auroral oval is delayed as one moves southwards.

There are longitudinal variations of absorption (Rapoport (32)). Maximum absorption occurs at geograhic longitudes 20°-90°E and 180°-210°E. We did not find any explanation in the literature of the phenomenon.

3 GEOMAGNETIC ACTIVITY

Solar events and the solar wind interacts with the magnetosphere and the ionosphere in a complex way described in textbooks such as Davies (8), Goodman (9) and Egeland et al (33). The interaction causes an increase of energetic particles within the magnetosphere. Depending on the intensity of the solar event, the increased energy of the magnetosphere can be dissipated immediately (magnetic storm) or stored and dissipated later in the form of several smaller substorms. During the magnetic storms or substorms, currents are established (e.g. auroral electro-jet in the E-layer), or existing currents are altered (e.g. ring current in the magnetosphere). The magnetic field as measured by magnetometers, vary according to the variation of the currents.

One consequence of the energy dissipation is that particle precipitation creates visible aurora in an oval centered at the geomagnetic poles (auroral oval). The more energy that is dissipated, the larger the geomagnetic disturbance and the extention of the oval towards mid-latitudes.

3.1 Indices of geomagnetic activity

Different indices exist that either indicates the general level of magnetic activity or some specific geomagnetic disturbance in the magnetosphere.

The K-index measures the irregular variation associated with magnetic field disturbances. It is measured at a given observatory over a three hour interval and is defined as the largest amplitude range R of anyone of the three magnetic field elements D, H and Z or alternatively X, Y and Z (Figure 3.1). A given amplitude range R corresponds to an integer between 0 and 9 which is a quasi-logarithmic scale. Different amplitude ranges are assigned each observatory to ensure that a measured value of K at a mid-latitude observatory can be compared with a measured value of K at an auroral observatory. The measurement of K is more sensitive to auroral disturbances than to other types of magnetic disturbances, and this has to be borne in mind when comparing the activity level at different observatories.

The K_p-index ("p"-planetary) is probably the most widely used of all the indices. It is a worldwide average activity level index based on measurements of K at 12 stations between geomagnetic latitudes 48° and 63°. The seasonal differences between the measurements have been removed, and the K_p-index is the average number of the 12 measurements for each three hour interval. Eight K_p-values will be tabulated throughout the day. The scale has been extended to comprise 28 values; 0, 0+, 1-, 1+,......9-, 9. Again, the K_p-index is very sensitive to auroral activity and insensitive to some other types of disturbance (Jursa (34)).
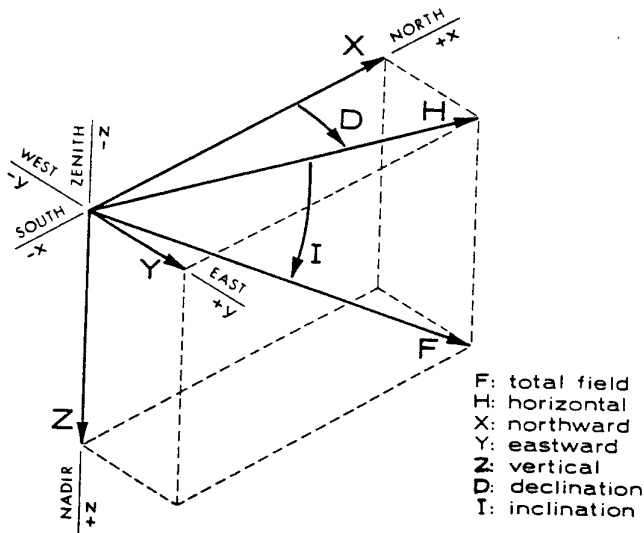
Figure 3.1   Geomagnetic field elements (Goodman (9))

The Q-index is calculated in a similar way as the K_p-index. The time resolution of this index is better than for the K-index; one value is recorded every 15 minutes. The index is computed from the more disturbed of the elements X and Y as the sum S of the absolute values of the maximum positive and maximum negative deviations from the normal (quiet) curve. For each interval in which S falls, the Q-index takes on an integer value between 0 and 11. The Q-scale is also quasi-logarithmic, but the geographical position of the measuring station has not been removed. Q must therefore be considered a local index that is not being averaged over several stations. The measurement of Q at one station only, is biased by the fact that the station cyclically moves towards and away from the auroral oval due to the rotation of the Earth. Ideally, it should be measured at an auroral latitude on its magnetic midnight meridian. The Feldstein and Starkov auroral oval boundaries (Section 3.2) are based on the Q-index. Because the amplitude range is being measured, the particular sensitivity to auroral disturbances also applies for this index. There are few measurements of the Q-index around the world so the availability of this index is quite limited. For the time being, Sodankylä in Finland and Kiruna in Sweden are the only places recording the Q-index. It is quite unfortunate that the Q-index no longer is being recorded at several places, since it has been perhaps the most successful single parameter describing auroral morphology.

The K_p and Q-indicies are very similar except for the time resolution and the fact that K_p is global and Q is local. So what is the relation between them? Feldstein and Starkov did not establish any relationship between the Q and K_p-index, even though they used both indices in the determination of the optical auroral oval boundaries as a function of geomagnetic activity. An analysis performed by the Air Force Global Weather Central, USA on the Feldstein and Starkov data, found this functional relationship between the two magnetic indices, where Q is measured near the magnetic midnight meridian:

$$Q = 3 \cdot K_p \qquad \text{for } K_p < 1 \qquad\qquad\qquad (3.2)$$

$$Q = K_p + 2 \qquad \text{for } K_p \geq 1$$

This approach for the conversion of the two indices has been adopted in the prediction program ICEPAC, and also in other ionospheric models. Hardy (35) used other sets of data and developed a relationship:

$$Q = 2 \cdot K_p - 0.35 \qquad\qquad\qquad\qquad\qquad (3.3)$$

A recent work (Dandekar (36)) claims, based on empirical knowledge, that Q is overestimated using the two equations above, especially at lower values of K_p. Dandekar suggests to use the relationship:

$$Q = 0.964 \cdot K_p - 0.3 \qquad \text{for } K_p \leq 2+ \qquad\qquad (3.4)$$

$$Q = 2.04 \cdot K_p - 2.7 \qquad \text{for } K_p > 2+$$

This formula will, according to Dandekar, give Q-values that will improve predictions of the auroral oval phenomena. The three different relationships are shown in Figure 3.2.
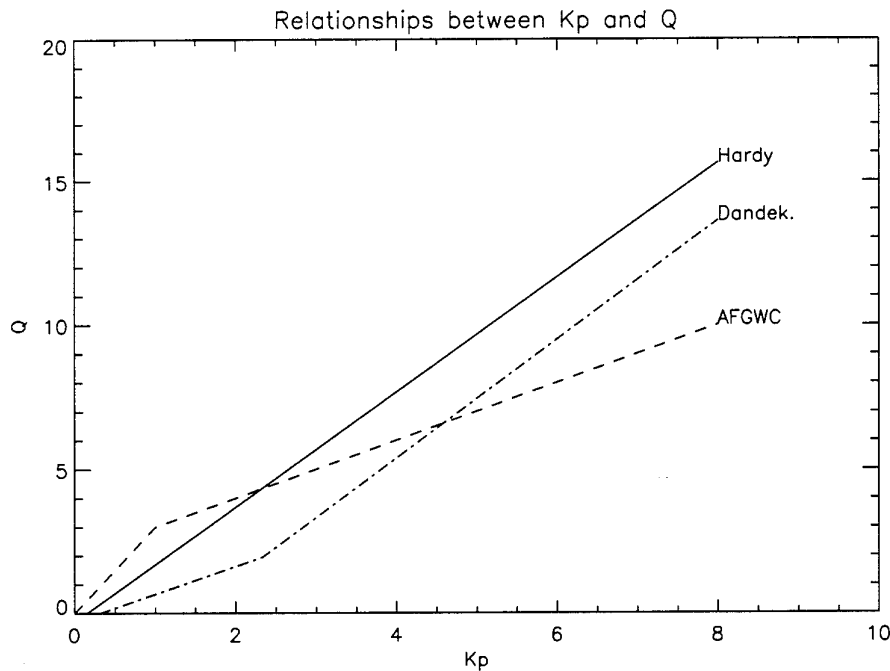

Figure 3.2 Different relationships between K_p and Q found in the literature (Dandekar (36))

There is a need to know both indices since in some ionospheric models (included the ICED-model), the K_p-index controls the mid-latitude trough and the Q-index the auroral

oval algorithms in the model. Besides, the low availability of the Q-index makes it convenient to have a conversion formula.

We have chosen to run ICEPAC with the "old" relationship (3.2), and *not* changing it to the probably more correct formula (3.4). The reason for this is that we want to focus attention on another improvement of ICEPAC that we are suggesting in this work.

3.2 The Feldstein and Starkov auroral oval

Feldstein and Starkov (37) have related simultanous measurements of Q on the magnetic midnight meridian and pictures of the aurora taken by all-sky cameras at many locations. The relationship between the auroral boundaries and the geomagnetic activity index Q has become known as the Feldstein and Starkov auroral boundaries. The oval boundaries depends upon the geomagnetic activity represented by Q, and time of day. The geographic latitude of the equatorward boundary Λ_{eq} of the auroral oval is found by a Fourier expansion (Starkov (38)):

$$\Lambda_{eq} = 72° - 0.9° \cdot Q - 5.1° \cos(\tfrac{360°}{24} t_{co} - 12°) \qquad \text{for } Q \neq 0 \qquad (3.1)$$

$$\Lambda_{eq} = 72.5° - 3.4° \cdot \cos(\tfrac{360°}{24} t_{co} - 18°) + 0.7° \cdot \cos(2 \cdot \tfrac{360°}{24} t_{co} - 45°) \qquad \text{for } Q = 0$$

where t_{co} is the time difference in hours between magnetic midnight and the actual meridian.

3.3 Using Q as an input parameter to ICEPAC

Note that the geomagnetic index Q in ICEPAC is the same Q as Starkov and Feldstein used in the determination of the position of the auroral oval as a function of time and geomagnetic activity. The Q in their work is the Q measured at auroral latitudes (geomagnetic latitude 65°) at the magnetic midnight meridian. So a local Q-index measured for instance at Kiruna should not be used uncritically in ICEPAC. Q-values from Kiruna will give correct predictions only for those hours at which the Kiruna site lies in the midnight sector of the Earth. It is better, since the availability of K_p is larger, to use the global K_p-index, and convert it to the midnight sector Q defined by Starkov and Feldstein. One of the formulas listed in Section 3.1 may be used for this purpose. The better time resolution of Q is lost in this way, but ICEPAC limits the time resolution to 1 hour anyway. The time resolution of Q will in this way be 3 hours, the same as for K_p. Work by Reilly (39), where the predictability and persistence of Q has been investigated, shows that the persistence of Q seems to be high for a three hour interval for the most frequently occuring Q-values. Therefore the loss of time resolution does not seem to be very important.

Reilly (39) has investigated 13 years of Q-data from one single station, Sodankylä (geomagnetic coordinates 63.4°N, 108.9°E), and determined distributions of occurences. The distributions have been related to sunspot numbers, season and time of day. The Q-index measured at Sodankylä shows a strong diurnal variation reproduced in Figure 3.3. Magnetic midnight is at 23 UT. The large variation between day and night is explained by the fact that Sodankylä moves in and out of the auroral oval with the rotation of the Earth. This leads to a serious under-estimation of both the Q-index and the duration of a disturbance in day time. Dandekar (40) has determined an empirical set of correction factors depending on time of day for the Q-data in Sodankylä. Using "detrended" Q-data, with correction factors specific for the measurement site, local Q-indices can be used as input to ICEPAC.
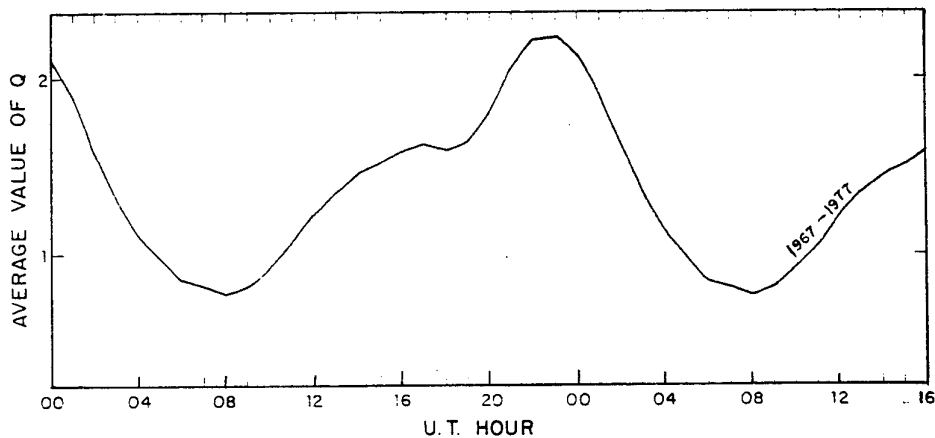
Figure 3.3   Diurnal variation of the average Q at Sodankylä, Finland. 10 years of data (Reilly (39))

A third approach to determine Q to be given as input to ICEPAC is to find Q_{eff} as described in Section 4.5.1, if satellite photos and electron/ion energy spectrometer data are available.

A difficulty arises in the practical use of ICEPAC after the Q-index was introduced as an input parameter. The sunspot number is predicted many months in advance and is available on datasheets or on Internet, but so is *not* the Q or K_p-index. The K_p or Q-index cannot be predicted months in advance since it varies from hour to hour. However, short-term forecasts of geomagnetic indices are issued regularly from solar-terrestrial observatories. With an increasing number of people and institutions connected to Internet, there are reasons to believe that the short-term forecasts will be of practical use to the radio operators in the future.

3.4 An estimate of the auroral oval coverage of Tromsø for the year 1969

There are two factors influencing the coverage of the auroral oval at a particular auroral location: 1) The time of day and 2) the actual extention of the auroral oval at that particular time. These two factors will independently cause a variable degree of disturbance above for instance, Tromsø. Dandekar (40) has determined the percentage time of day that a specific geomagnetic latitude λ is poleward of the equatorial oval boundary as a function of Q, using the Starkov Equation (3.1). Table 3.1 gives the calculated values.

λ	Q Index 0	1	2	3	4	5	6	7	8	9	10
57											6
58										8	21
59									13	21	29
60								13	23	29	38
61							15	25	31	38	44
62						17	25	33	38	46	50
63					17	25	33	40	46	50	56
64				17	27	33	40	46	50	58	63
65			21	29	33	42	46	52	58	63	71
66	6	21	29	35	42	46	52	58	65	71	79
67	21	29	35	42	48	54	58	65	71	79	94
68	29	38	42	48	54	58	67	71	79	100	100
69	38	42	50	54	60	67	73	83	100	100	100
70	44	50	54	60	67	75	83	100	100	100	100
71	50	54	63	67	75	83	100	100	100	100	100
72	56	63	69	75	85	100	100	100	100	100	100
73	63	71	77	88	100	100	100	100	100	100	100
74	71	79	88	100	100	100	100	100	100	100	100
75	79	92	100	100	100	100	100	100	100	100	100
76	94	100	100	100	100	100	100	100	100	100	100
77	100	100	100	100	100	100	100	100	100	100	100

Table 3.1   Percentage of day that geomagnetic latitude λ is poleward of the equatorial oval boundary as a function of Q (Dandekar(40))

The actual distribution of Q-values at a certain location has to be determined through measurements. Dandekar (40) has calculated probabilities of different values of Q and cumulative probabilities for Q based on Q-data from Sodankylä. The diurnal variation of the data has been removed by using the correction factors for Sodankylä. Table 3.2 gives the detrended probabilities p(Q) and cumulative probabilites $P(Q_{observed} \geq Q)$ for the year 1969:

Q	0	1	2	3	4	5	6	7	8	9	10
p (%)	36	24	12	10	7	5	3	2	1		
P (%)	100	65	41	30	20	13	8	5	3	1	1

Table 3.2   Probabilities and cumulative probabilities for Q at Sodankylä. Data from the year 1969 (Dandekar (40))

The product of the percent period in Table 3.1 and the cumulative probabilites in Table 3.2 gives the average percent of time that the auroral oval is equatorward of a given geomagnetic latitude caused by Q-values larger or equal to the selected number.

The distance between Tromsø, Norway (66.8 N, 117.7 E geomagnetic coordinates) and Sodankylä is 400 km, with Tromsø placed to the north-west of Sodankylä. A rough assumption is that the correction factors for the diurnal variation are the same in Tromsø and Sodankylä, and that the same Q will be measured at the two sites. Using the Q database at Sodankylä, we calculate the average annual percent of time that the auroral oval covered Tromsø in 1969 for different values of Q:

Q>	0	1	2	3	4	5	6	7	8	9	10
Time (%)	21.0	18.9	14.4	12.6	9.6	7.0	4.6	3.3	2.1	0.8	0.9

Table 3.3   Annual percent of time that the auroral oval covers Tromsø caused by different degrees of geomagnetic activity

During 21.0 % of the time in 1969 the southern border of the auroral oval was south of Tromsø integrated over all 24 hours. During 7.0 % of the time the southern border was south of Tromsø because Q≥5.

4   HF COMMUNICATIONS PREDICTIONS

With the advanced technology now existing for HF-communications and remote sensing, real-time channel evaluation (RTCE) and model updating are relatively frequently in use. These are helpful tools for establishing communications based upon the actual state of the ionosphere. Short-term predictions, or forecasts, typically update the ionospheric model based on RTCE data to provide accurate predictions for time periods of tens of minutes. The forecast will not represent average conditions because of high temporal and spatial variability of the ionosphere. For the purpose of design of equipment and planning, e.g. frequency management, long-term predictions of the average state of the ionosphere and average circuit performance are needed. Predictions of circuit parameters is no better (but potentially worse) than our knowledge of the underlying ionosphere. Textbooks such as Davies (8), Goodman (9) give detailed motivations for and descriptions of both short and long-term prediction methods. In this chapter, only long-term predictions will be described, and only those aspects that are of interest to this work.

There exists a wide range of different prediction programmes that use slightly different algorithms in the computation of circuit parameters. For instance, emphasis may have been put on the geophysical regions in which the programs are in use (e.g. Australia or auroral oval). Nevertheless, the basic prediction methods are to a large extent the same. We will describe briefly the general prediction methods common to many prediction programmes. The more detailed description of certain circuit parameters will refer to the prediction programmes IONCAP/ICEPAC developed at ITS in Boulder, specifically.

4.1   Long-term predictions - general principles

Inputs to the prediction programme are typically: Geographic coordinates of the transmitter and receiver, sunspot number, an index of geomagnetic activity, frequency, time of day, transmitted power, noise level at the receive site, antenna parameters, a required signal-to-noise ratio for a specific signal quality and a required reliability to meet a specific grade of service.

From the geographic coordinates, the path geometry is calculated, and the geographic/geomagnetic positions of certain points along the path are determined. The number of points is determined from the length L of the path: L≤ 2000 km implies one point, 2000 km < L ≤ 4000 km implies three and L > 4000 km implies five points. The number of points is not explicitly related to the probable number of hops, but experience has shown that the following is a useful approach: When only one point is used, the midpoint is chosen. When three points are needed, the midpoint, and two points each 1000 km from each end of the path are chosen. The five points are chosen as the midpoint, two points each 1000 km from the end points and two points each 2000 km

from the end points of the path. For very long distance communications, L > 8000 km, it is difficult to distinguish between the different propagating modes, and a separate model for propagation predictions is used.

Each point is now classified according to geomagnetic position and time (i.e. the ICED-model described in Section 4.5) and ionospheric parameters such as critical frequencies, heights of maximum electron density and semi-thickness of layers are found for each point using numerical maps. The ionospheric parameters at the different points are combined and complete electron density profiles are computed at one to three control points depending on the path length. If the path is less than 2000 km, only one electron density profile is computed at the path midpoint.

The control point with the "most pessimistic" ionosphere (minimum f_oF_2 or minimum f_oE if the f_oF_2-values are equal) is selected as the control point that determines the MUF. Maximum usable frequencies (MUF's) are found for each layer. If the path is long enough, a multihop mode may be chosen as the layer MUF. The largest layer MUF is selected as the circuit MUF.

The electron density profiles at the control points are converted to ionograms, and reflectrixes are calculated for each ionogram. Reflectrixes show the relationship between oblique frequency, take-off angle and virtual reflection height (thereby also the hop-distance). Now the possible number of hops are found for each frequency. For each of the possible modes, losses and signal strength with distributions are calculated. E_s-modes are examined separately.

The probability of ionospheric reflection at a certain layer for a specific frequency can be calculated by assuming a Gaussian distribution of the layer MUF.

Finally, reliability and other system parameters are calculated for each possible mode separately, and a most reliable mode is selected. Circuit reliability of all modes combined is found by assuming a random phase and adding the powers from all modes. The least usable frequency LUF is determined as the minimum frequency at which the calculated circuit reliability is above a required reliability.

The method described here will give a prediction valid for one particular communication path. With fast computers the method can be repeated for many receive locations, and broadcast coverage areas can be found. General and specific descriptions of prediction methods can for instance be found in Davies (8), Goodman (9), and CCIR 252-2 (41).

4.2   Predicted parameters of interest to this work

We need to define and explain some of the output parameters from ICEPAC (Stewart (1)) that are used in this work. They will later be compared with HF experimental data in Chapter 6.

<u>Virtual height of reflection.</u> From the electron density profile, a vertical ionogram is calculated by integration of the group refractive index (Equation 2.5). Using the secant law (Section 2.1) with a correction for a curved ionosphere, one obtains a set of possible oblique rays that are reflected from the same true/virtual height as the equivalent vertical frequency. For the particular oblique frequency considered, a subset of rays can be found that gives the coverage area with corresponding virtual heights (reflectrix). For a particular path, the modes able to propagate are selected from this second rayset.

<u>MUF.</u> There are many definitions of MUF and related terms (Goodman (9)). In this context of prediction, MUF is a parameter based upon monthly median values of the ionospheric characteristics. The probability that a sky-wave path exists at the circuit MUF is 50% since the ionospheric parameters represent average conditions.

In ICEPAC, layer MUF's and circuit MUF are determined at the midpoint of the path if there is only one control point. If there are more than one control point, MUF's for the E, F_1, and F_2-layers are determined based on the "most pessimistic" electron density profile. A E_s-layer MUF is also calculated, but is not taken into account when selecting the largest layer-MUF as the circuit MUF. The statistical distribution of the F_2-MUF about the monthly median is tabulated as a function of latitude, sunspot number, season and time of day (Davies and Groome (42)).

<u>Absorption.</u> This parameter will be treated thoroughly in Section 4.3.

<u>Noise and interference.</u> There are three types of external noise included in ICEPAC; galactic, atmospheric and man-made noise. They are all statistical parameters with a log-normal distribution about the mean. The galactic noise model is described in CCIR 258-4 (43) and the atmospheric noise model in CCIR 322-3 (44). The general level of man-made noise is specified by the user of the program and includes the noise from power lines, industrial machinery, ignition systems etc. The combination of the three noise sources is done by a statistically accurate method, and the log-normal distribution that approximates the sum is determined. It is important to note that interference from other users of the HF spectrum and channel occupancy, which is a major problem in the HF-band, is *not* included in the noise model, or taken care of by any other means in the prediction programme.

<u>Circuit reliability.</u> For each possible propagating mode, mean signal power and noise power can be found. The distributions are log-normal. The required signal-to-noise ratio (RSNR) is specified by the user for a particular type of service as the minimum required

signal power in the occupied bandwidth relative to the hourly median noise power (in dB) in a 1 Hz bandwidth. Based on the RSNR given as input to the programme, mode reliabilities can be found. The most reliable mode is then selected. Circuit reliability is calculated by adding the mean powers of *all* modes, assuming that the relative phase relationships between the contributing modes are random. The mean signal-to-noise-ratio of the sum is compared with the required signal-to-noise, and circuit reliability determined as the probability of the actual SNR being larger than the required SNR. If a specific mode does not propagate efficiently, for instance because of large Above-the-MUF losses, the contribution of that mode to the overall reliability will be insignificant. The circuit reliability (in this work called reliability) expresses the fraction of days (over a month) that the signal-to noise is larger than the required value. See also Section 4.3.2.

4.3   Prediction of losses

For each possible ionospheric mode, the parameter "system loss" is calculated. In ICEPAC the system loss is defined as the loss a radio wave will experience from the point it enters the transmitting antenna circuits until it escapes the receiving antenna circuits. Thus the antenna gains are included in the total system loss, but antenna transmission line loss is not.

The components of the total system loss in ICEPAC are:

1) basic free-space transmission loss (standard formula),
2) ionospheric absorption (described in detail in Section 4.3.1),
3) ground reflection loss (standard formula),
4) above-the-MUF loss (described in Section 4.3.2),
5) a possible auroral loss and
6) transmitting and receiving antenna gains.

4.3.1   Prediction of ionospheric loss

The ionospheric absorption equation used in most prediction programmes is a semi-empirical relationship derived from observations on high frequency circuits (Laitinen and Haydon (45)). The basis for the formula is an equation derived by Appleton which gives the non-deviative absorption on a vertical incidence path due to the ionization in a simple Chapman layer. The Chapman layer is formed in an exponential, isothermal atmosphere, and the radio frequency in use must be much greater than the collision frequency. The equation is:

$$L_i = 4.13 \cdot \frac{4\pi^2 e^2}{mc} \cdot \frac{N_0 \nu_0 H}{(\omega \pm \omega_L)^2} \cdot \cos^{1.5}(\chi) \qquad (4.1)$$

where N_0 is the maximum electron density of the layer and v_0 is the collision frequency at the height of maximum electron density, both at a solar zenith angle $\chi=0$. H is the scale height of the atmosphere.

Data from HF circuits at middle and low latitudes indicate that ionospheric absorption in the height 60-120 km prevails until $\chi=102°$, so the cosine-term of the equation has been modified to $\cos^{1.3}(0.881\chi)$. Analysis of data taken over a period of several years have shown that the absorption depends on sunspot number, SSN. To incorporate this dependence, Equation 4.1 has been multiplied by $(1+0.0037 \cdot SSN)$. For simplicity, ω_L has been substituted by ω_H, the gyrofrequency at 100 km altitude, and least square curve fitting was used to make the equation usable also for frequencies which are not sufficiently greater than the collision frequency. In the earlier versions of IONCAP the final equation used in the prediction of ionospheric loss of the ordinary wave on an oblique incidence path is as follows:

$$L_i = \frac{677.2 \cdot n \cdot \sec\varphi \cdot (1+0.0037 \cdot SSN) \cdot (\cos^{1.3} 0.881\chi)}{(f+f_H)^{1.98}+10.2} \tag{4.2}$$

n is number of hops, and φ is the angle of incidence of the wave on the ionosphere. Deviative losses are considered to be averaged into Equation 4.2 for those modes with reflection heights less than that of the layer MUF. A complete description of the development of Equation 4.2, which has also been adopted by the CCIR, is given in Laitinen and Haydon (45) with revisions made by Lucas and Haydon (46).

The observations used in the fit of (4.2) are from F_2 layer modes only. Further corrections to the equation are therefore needed. For D/E-region modes a loss term is added which can be positive or negative depending on the height of reflection within the E-layer to account for the effects of E-region electron density on non-deviative absorption. To prevent the ionospheric absorption from becoming artificially large when the true height of reflection is below 90 km, the collision frequency parameter 10.2 in the denominator is increased for these reflection heights.

For low angle rays, the deviative absorption is considered to be averaged into Equation 4.2, but for high angle modes (Pedersen rays), where the height of reflection is higher than that of the layer MUF, a deviative loss term is added.

Sporadic-E layers are not included in the electron density profile. Modes passing through it will experience a type of loss called the E_s-obscuration loss (Phillips (47)). E_s-obscuration loss is set equal to zero for D/E-modes, but for F-modes a mean statistical E_s obscuration loss is obtained from statistical maps of f_oE_s.

In ICEPAC, a different form of the absorption index

$$I=(1+0.0037 \cdot SSN) \cdot \cos^{1.3}(0.881\chi) \tag{4.3}$$

has also been used. f_0E is now available as a numerical map which includes the variation in zenith angle and solar activity. The alternative formula used in ICEPAC is:

$$I=-0.04+\exp(-2.937+0.8445 \cdot f_0E) \tag{4.4}$$

It was shown by Thrane et al (4) that the use of this equation in an auroral ionosphere can produce excessive ionospheric loss which has no physical relevance. Equation 4.3 gives a smoother, more realistic result but it does still not reproduce the auroral absorption observed at high latitudes.

To summarize, Equation 4.2 is based on an assumption that the D-region is a Chapman layer. Numerous modifications have been made according to measured data, and deviative losses are incorporated into the equation. In contrast to the Appleton-Hartree absorption loss equation (Equation 2.16, Section 2.5), Equation 4.2 contains no explicit height dependence of absorption, electron densities and collision frequencies.

4.3.2   Above-the MUF loss

Above-the MUF loss has been discussed for many years within the HF community. The amount of literature on this topic is large, for instance: Phillips and Abel (48), Wheeler (49), Bradley and Bedford (50), Bradley (51), Bradley et al (52), Argo (53) and Hagn et al (54). In our work, this area of discussion came into focus when we found that different users of the ICEPAC program had modified their versions of ICEPAC according to their own opinions on the subject. We had to choose a version of ICEPAC, and therefore some insight into the problem was necessary.

The background for the discussion is the following: The MUF is a statistical parameter with a certain distribution depending on hour, latitude etc. Even when the instantaneous MUF has been determined using ionosondes, observations have shown that as the frequency increases from just below to just above the MUF, the signal does not drop to zero instantanously. The signal power is reduced, but propagation *is* possible on frequencies above the MUF. The propagation mechanism at these frequencies is not by ionospheric refraction, but rather by scatter from ionospheric inhomogenities and two-hop ground backscatter (Hagn et al (54)). Argo (53) claims that this Above-the MUF propagation is not well documented.

The current version of ICEPAC does not model this scatter propagation independently from the propagation by reflection. The probability that a mode exists at frequencies near the mode MUF, is not used in the calculation of mode reliability. Instead, a loss term, above-the-MUF loss (a-t-M-loss) has been added to the total loss at frequencies above the mode MUF. The a-t-M-loss increases rapidly with increasing frequency above the mode MUF. The signal strength and circuit reliability decreases correspondingly.

Different forms of the a-t-M loss have been suggested and implemented in the different programs (Hagn et al (54)). Using the method described above, the calculated probability of the SNR exceeding a certain required SNR, P_{SNR}', expresses the total time a specific grade of service can be expected, independently of the available modes. CCIR 252-2 Supplement (55), CCIR 894 (56), and IONCAP/ICEPAC use this method of calculating circuit reliability R_c, expressed as

$$R_c = P_{SNR}^l \qquad (4.5)$$

An older, but phenomenologically more correct approach (Argo (53)), calculates the circuit reliability as the joint probability of the mode availability q and the probability of the SNR exceeding the required SNR, *provided* that the mode exists, P_{SNR}:

$$R_c = q \cdot P_{SNR} \qquad (4.6)$$

CCIR 252-2 (41) and earlier versions of IONCAP/ICEPAC use this method. The two methods give significantly different values for the circuit reliability.

It is important to distinguish between the two definitions of mean/median signal strength; is it the mean over all days of a month, or the mean over the time that the signal is detected? Normally, circuit reliability is used by radio operators and frequency planners, and they want it to express the probability of achieving a certain SNR averaged over a month. Either of the formulae (4.5) and (4.6) can be used for this purpose. System designers are more interested in the parameter SNR and its distribution only when modes *are* propagating. It is therefore important for them to use the definition of the signal strength distribution that includes the effect of propagation, P_{SNR}'. There should be consistency between the definition of signal strength that a prediction programme uses and the way empirical data used in the programme have been measured. For instance, the measured absorption and its distribution depends on the nature and continuity of the experiment. The same applies to a-t-M losses.

IONCAP/ICEPAC is an accepted, well established prediction programme, and many authors support the approach of using Above-the MUF losses. Because the source code of ICEPAC, (version released in the summer of 1994) was made available to us directly form ITS in Boulder, we decided to start out using this version of ICEPAC in our work, but we will come back to a discussion of whether or not the ICEPAC approach is best.

4.3.3   Comparison of the different losses

To compare the magnitude of the different losses we choose one particular path Andøya-Alta (285 km) in the north of Norway for which HF test data has been collected. Data and predictions will be compared in later chapters.

The transmitter and receiver antennas used in the prediction are both horizontal dipoles found in the ICEPAC antenna library. The antenna gains are 5 to 6 dB depending on which mode is propagating on each frequency. The transmitted power is set to 300 W. This path is a typical one-hop path. Basic free-space transmission loss is the largest loss (90-110 dB) contributing to the total loss. It is calculated using standard formulas depending only on frequency and total path traversed. Figure 4.1 shows the contributions from the different types of losses at various frequencies for the most reliable mode propagating (March 1988, SSN=71). Basic free-space transmission loss is omitted in the figure because it is order of magnitude larger than the other losses. The abbreviations of the losses are explained in the figure text.

Four situations are shown: Q=0, noon and midnight, and Q=8, noon and midnight. The corresponding MUF's are 7.5 MHz, 3.5 MHz, 7.4 MHz and 7.7 MHz, respectively. For Q=8 a large auroral E-layer is causing the relatively high MUF at night. At the MUF, the above-the-MUF loss is 3 dB, and it increases rapidly at larger frequencies. At frequencies sufficiently below the MUF, this loss term is zero.

The non-deviative loss decreases with increasing frequency. There is little difference between Q=0 and Q=8, but pronounced larger non-deviative absorption during daytime than at night. This is so because Equation 4.2 is solar driven, not driven by the actual product of electron density and collision frequency in the ionosphere.

The residual auroral loss contributes significantly to the total loss. It is independent of frequency, but depends on time of day and geomagnetic conditions. For high geomagnetic activity, Q=8, this loss term is exceeding the non-deviative loss by 4-6 dB at night. During day this auroral loss adjustment is independent of geomagnetic activity.

The correction loss term will always be zero for low angle F-region modes. For high angle F-region modes this term will include a correction for deviative loss. For low angle D/E-region modes this term will be negative to correct for the low-electron density regions that are traversed. This is observed for Q=8, midnight. For high angle D/E-region modes the correction term will include both effects; deviative loss and corrections for the electron densities in the E-region. This loss term is contributing little to the total loss for this path.

E_s obscuration loss is also approximately zero and it affects only F-region modes that have a probability of traversing a sporadic-E layer.
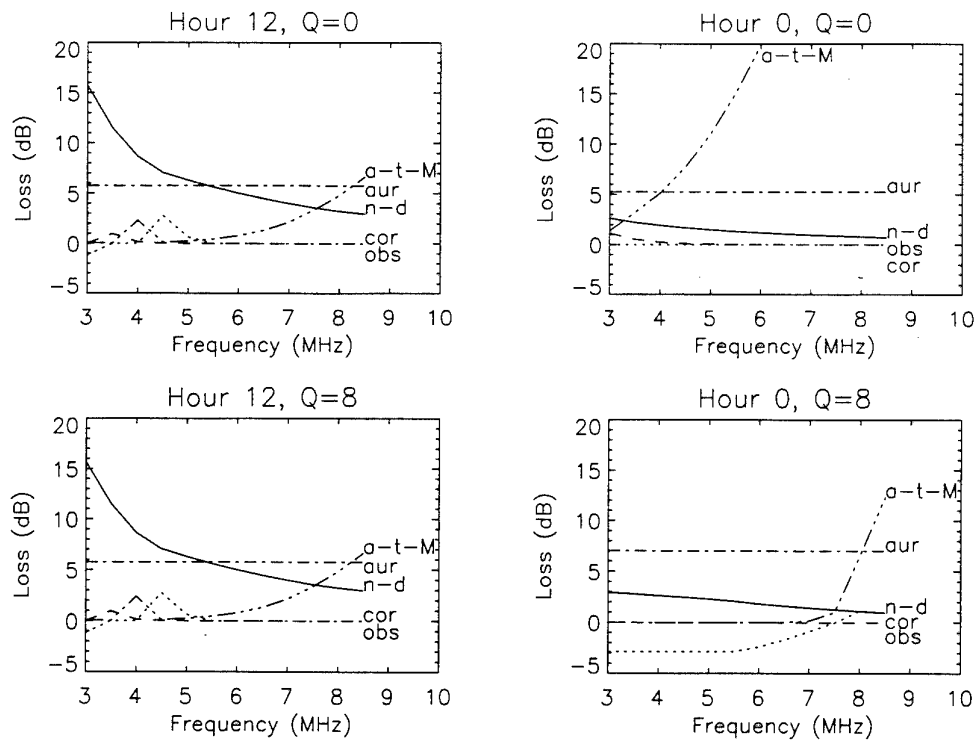
Figure 4.1 ICEPAC predictions of different types of losses for the most reliable mode as a function of frequency, time of day and geomagnetic conditions

a-t-M:	above-the-MUF loss
aur:	residual auroral loss adjustment to median signal level
n-d:	non-deviative loss
cor:	correction loss term including the effect of deviative loss on high angle modes, and E-region electron density on D/E-reflected modes
obs:	E_s obscuration loss

To conclude, geomagnetic activity has very little effect on daytime predictions. This is expected since the path is then south of the auroral oval. At night, geomagnetic activity causes the electron density profile to change. However, geomagnetic activity does not increase the non-deviative loss as expected from theoretical calculations and from experience.

4.4   Predictions of the most reliable mode

Depending on the path length and frequency, up to three hops may be considered. For each hop combination (1-hop, 2-hops, 3 hops), up to six possible modes can be found (high/low angle E, F_1 and F_2 reflections) by examining the reflectrix table. 1-hop E_s and 2-hops E_s with a fixed reflection height are also modes that may propagate. This sums up

to a maximum of 20 possible modes that are considered for propagation. On a short path (of special relevance to this work), the number of candidate modes are usually a lot less (5-10). For each of the modes, signal to noise ratioes and mode reliabilities are calculated at the receiver. The selection criteria of the most reliable mode are the following: The mode with the highest mode reliability is selected. If the reliabilities are the same within 0.05% for two modes, the mode with the lower number of hops is selected. If the number of hops is the same for two modes, the mode with the highest signal-to- noise ratio is selected.

Certain output parameters from the prediction programme such as delay, virtual height of reflection, loss, angle, mode and probability of mode propagation refers to this *most reliable mode*, whereas other parameters, such as circuit reliability, signal strength and signal-to-noise ratio refers to a power sum of the possible modes (random phase approximation).

4.5   The ICED model

ICEPAC is the last version of a series of prediction programmes developed at the ITS in Boulder. The previous version, IONCAP, has been one of the most widely used prediction codes. Its features are described in Teters et al (2).

The low and middle latitude model used in ICEPAC is basically the same as the IONCAP model, but two modifications have been made that refer to all latitudes (Thrane et al (4)):

- Chapman layers are used for the E, F_1 and F_2 -layers instead of parabolic layers. This causes a slight increase of the predicted MUF's as well as a lowering of the predicted reflection heights. These changes are due to increased electron densities below the maximum of the layer.

- New coefficients recently approved by URSI are implemented. These coefficients are created on the basis of a semi-empirical model (using top-side ionosonde data) in order to improve the predictions above the oceans and other areas where there is a lack of ground based observations.

The main improvement relative to IONCAP has been obtained for high-latitude and polar cap propagation predictions. The ionospheric model used in ICEPAC is the ICED (Ionospheric Conductivity and Electron Density) profile model described by Tascione et al (57). It specifies the location of the auroral oval in corrected geomagnetic coordinates using the effective Q-index (Section 4.5.1) as a measure of the global geomagnetic activity.

The ICED model specifies the electron densities from 90 km to 1000 km, every 1° in latitude from 20°N to 80°N and every 5° in longitude, as a function of solar activity,

solar zenith angle, geomagnetic activity and magnetic local time. It does not contain any electron density model of the high-latitude D-region. The ICED-model divides the ionosphere into four latitudinal regions: the polar cap, the auroral zone, the sub-auroral trough and mid/low latitudes.

At low and mid-latitudes, the electron density profile contains an E-layer, an F_1-layer during sunlit hours, and an F_2-layer. Their representations are found from numerical maps and adjusted for solar zenith angle, geomagnetic time and sunspot number.

The sub-auroral trough region is characterized by a depletion of the F_2-region. The driving parameter for the F_2-electron densities in this region is the K_p-index. A large geomagnetic disturbance will cause a large depletion. The E and F_1-regions are not affected.

In the auroral zone, the E-layer can be produced by solar ionization, particle precipitation, or both. During daytime the E-region is purely solar, determined from numerical maps. The E-layer caused by precipitating particles at night/sunrise/sunset is determined from the amount of geomagnetic disturbance (Q-index). The F_1-layer in the auroral zone has a constant, fairly small value. The form of the F_2-layer is common for the auroral zone and the polar cap, and is derived from numerical maps applying certain modifications according to the precipitating particle flux.

In the polar cap, the E and F_1-layers are constants with the f_oE being largest.

4.5.1   Qeff used in the ICED model

Because the Q-index data are so scarce, satellite photos combined with data from electron/ion energy spectrometers can be used to locate the auroral oval equatorward boundary. This value Λ_{eq} is inserted into Equation 3.1 to determine an *effective* Q-value, Q_{eff}, which is based on the "current" state of the high-latitude ionosphere. Q_{eff} can then be used to calculate Λ_{eq} at other local times.

In ICEPAC, the Q_{eff} can be given as input to the program, if available.

4.6   Limitations of long term prediction programmes

Before increasing the complexity of a prediction programme, the improvements by doing so should be carefully examined. If the calculations or models in one part of the program are rather coarse, there may be no use making other parts very accurate.

Normally some general simplifications and assumptions have been made in long term prediction programmes. The most important are:

Samples of the ionosphere are taken at certain control points along the great-circle path. The radio propagation is calculated according to the state of the ionosphere in these control points. Horizontal gradients of the electron density along the ray path are therefore ignored. This is a simple, semi-empirical method used in long term predictions that has been shown to give fairly good estimates of average conditions. Nevertheless, reflections might occur off the great-circle path, and to predict such asymmetric propagation, more complex raytracing algorithms are necessary.

The detailed effects of the Earth's magnetic field and collision frequency on the raypaths has been neglected. That means that the radio wave is not split into an ordinary and extraordinary wave as it propagates through the ionosphere. The equivalence relationships mentioned in Section 2.1 are valid only when the magnetic field is neglected. The calculated true and virtual heights are therefore not strictly correct, but the simplification made in the predictions does not give errors of importance to operators and system designers. The magnetic field and collisions have been accounted for in calculations of absorption by using an effective frequency corresponding to the propagating frequency plus the gyro frequency, and by using an estimated collision frequency.

5 HF TESTS USING AN OBLIQUE INCIDENCE SOUNDER

5.1 Experimental method

Ionospheric HF communications has been an area of research for many years at the Norwegian Defence Research Establishment (FFI) (Skaug (58), Thrane(59), Thrane and Bradley (60)). A new experiment in this field was designed in 1986, and the project was called Short Wave Oblique Incidence Spread Spectrum Sounding Project (SWOSSOP). The project was a collaboration between NUWC (Naval Underwater Warfare Center) in Massachusetts and FFI. The oblique incidence sounder used conventional as well as direct sequence spread spectrum (DSSS) radio techniques.

The aims of the experimental study were (1) to obtain a statistical description of the properties of ionospheric communication channels within and close to the auroral zone; (2) to study the influence of geophysical disturbances on the reliability of the ionospheric channel; (3) to determine the degree to which the ionospheric channel can carry a broadband signal; (4) to compare the experimental results with the current ionospheric models, as represented by the prediction codes; and (5) to use the experimental results to evaluate and improve predictions at high latitudes.

The first part of the tests took place within the auroral zone. The transmitter was located at Andøya (69.30 N 16.02 E), and the receiver was in Alta (69.90 N 23.20 E), a distance of 285 km. The tests were conducted between January 1987 and December 1988 on this path. In July 1989 the HF test transmitter was moved to Kløfta (60.07 N 11.12 E). The new path, Kløfta-Alta, is 1230 km long and is a mid-latitude path most of the day. Data were collected over this path from January 1990 to June 1992. The two paths are shown in Figure 5.1. The right part of the figure show two possible propagation modes for the long and short path, respectively.

The observations were organized in an hourly schedule and ran 24 hours a day. A standard message was transmitted every hour on nine frequencies, and on five different bandwidths for each frequency. The Bit Error Rate (BER), the relative amplitude and time delay of up to five multipaths, as well as the signal and noise level were recorded automatically for each transmission.

The database contains observations recorded over several years, but, unfortunately, technical and logistic problems have caused gaps in the sequence of recordings. For example, there is a lack of data during wintertime for the short path. Nevertheless, the database covers diurnal and seasonal variations, different levels of geomagnetic activity, and sunspot numbers from 35 to 158. A complete table listing the periods of measurements can be found in Appendix A.

A detailed description of the measuring system and the first results from the data analysis can be found in Jodalen et al (61).
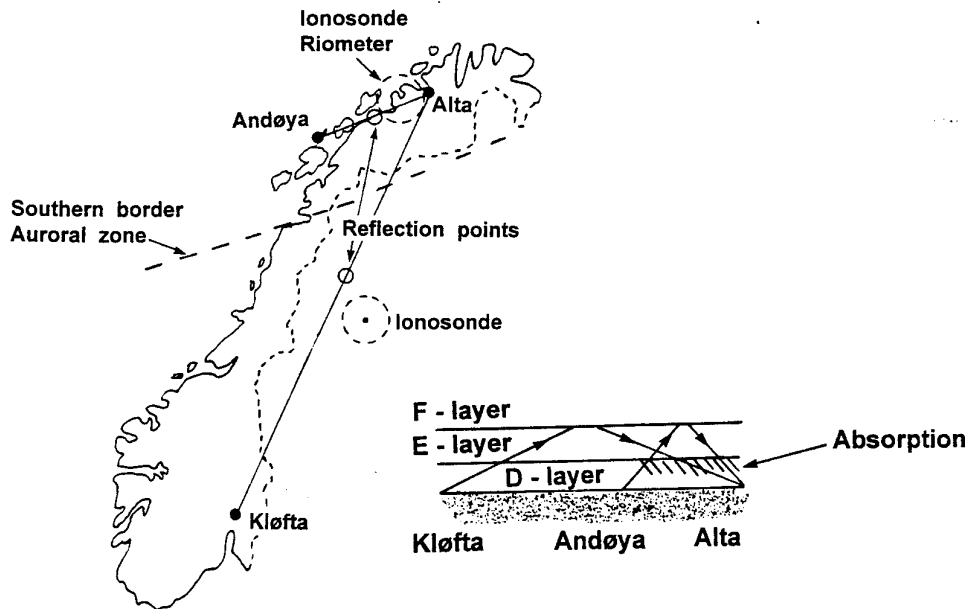
Figure 5.1   Location of transmitter and receiver for short and long paths

5.2   Tecnical description

5.2.1   System components

Figure 5.2 shows two block diagrams of the transmitter and receiver system.
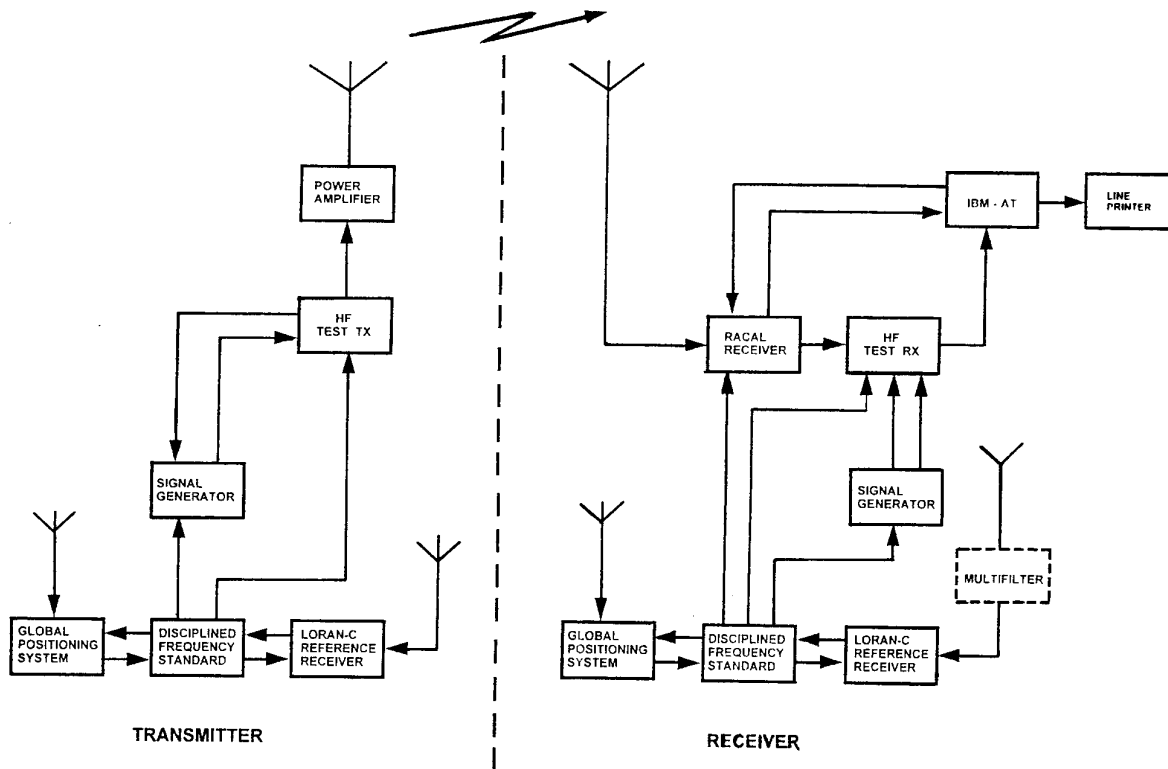

Figure 5.2   System modules

The HF test transmitter and test receiver were designed and built at FFI specially for this purpose. They control the timing, the scheduling of different frequencies and bandwidths, the modulation/demodulation and coding/decoding of the standard message. The RF signals are received by the Racal receiver which converts them to a 455 kHz Intermediate Frequency and passes them on to the HF test receiver. For each hour the message is sent on nine different frequencies; 3.0, 4.5, 6.0, 8.5, 10.5, 12.5, 14.5, 17.0 and 19.0 MHz, and for each frequency, using five different bandwidths; 0.5 kHz (conventional), 5, 20 80 and 160 kHz (spread spectrum). Thus the total number of messages transmitted each hour is 45. The message is 15120 data bits long of which the data content forms the last 14931 bits. The modulation method used is differentially encoded PSK (DPSK), and the signals are detected non-coherently. The encoding of the message is necessarily slightly different for the conventional signal than for the direct sequence spread spectrum signal.

Direct sequence spread spectrum messages.
DSSS systems are characterized by relatively low data rates, high interference rejection and low probability of interception capabilites. Thus they have traditionally been used in military applications. For the spread spectrum messages in our experiment, a spreading code (Pseudo Noise sequence) consisting of 31 bits (chips) is used for each data bit. The messages will occupy different bandwidths determined by the different chiprates utilized and the modulation method. The corresponding data rates will therefore also be different ranging from about 80 bits/sec at 5 kHz bandwidth to 2500 bits/sec at 160 kHz bandwidth. The first 63 databits of the preamble of the message are used for detecting the "phase" of the received signal at chip level to be able to sample the narrow correlation peaks at the right time. These 63 databits are not data modulated i.e. they are all 1's, so the same spreading code is sent 63 times. At the receiver, which is shown in Figure 5.3, the incoming analogue signal is downconverted to baseband by splitting it in an in-phase and quadrature component, sampled at a rate of eight times the chiprate and correlated with the 31-bit reference code in order to remove the code content and retain the data information in form of correlation peaks. To obtain "Chip-sync" during the first 63 databits, the output of the two correlators is squared, added and sampled. A transversal filter then delays the samples corresponding to several data bits and adds them in order to increase the probability of detection and decrease the false alarm rate. If the averaged correlation peaks exceed a threshold level, synchronization at chip level is obtained and the DPSK demodulator is enabled. Synchronization at chip level is a time critical task in spread spectrum systems, and is necessary in order to proceed with the reception. The next 63 data bits of the preamble are data modulated using a 63 bits PN-sequence. One spreading code is sent if the data bit is 1, and the inverted spreading code if the data bit is 0. This sequence of 63 data bits is used to detect the "phase" of the message at data bit level. The in-phase and quadrature signals after the quadrature correlators are now used for demodulating first the 63 data bits in the preamble, and, if "Message-sync" occurs, the data content of the message. The 63 demodulated data bits are passed on to a digital correlator that correlates the demodulated signal with
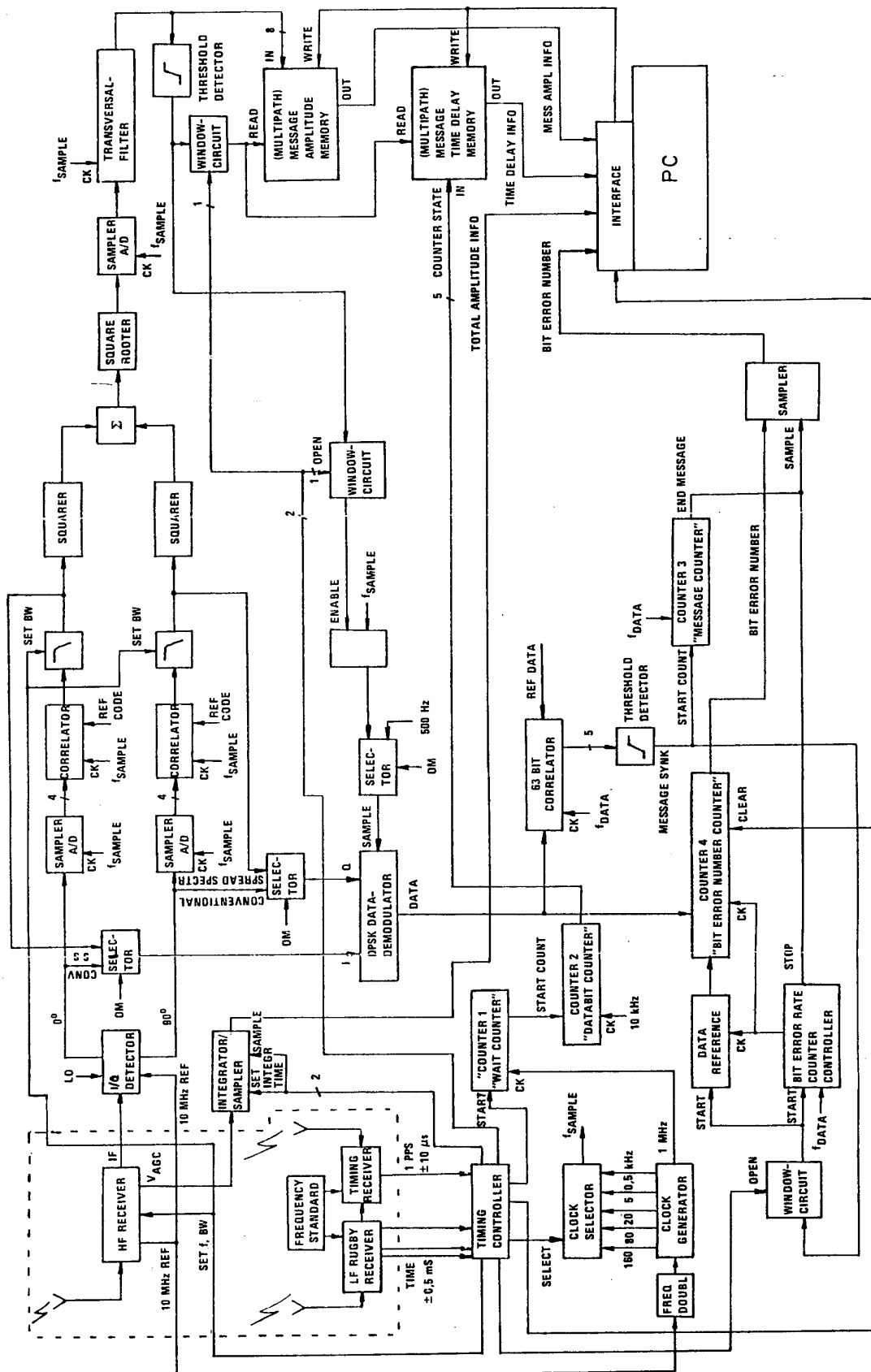
Figure 5.3   Block diagram of receiver

the known 63 bits PN-sequence. If the correlation peak exceeds a threshold, "Message-sync" has occurred, and the start of a message is detected. The received data bits can now be compared with the reference, and bit errors counted. The 14931 data bits comprising the data content of the message are data modulated in a similar way to the message-sync preamble, using a 63 bit repeating PN-sequence. The message contains no "End"-information; the bit error counting is stopped at a fixed number of data bits after the "Message-sync" occurs. A PN-sequence was chosen because of its good orthogonal qualities.

Conventionally encoded messages.

The data bits are not represented by spreading codes. For conventional radio signaling, the demodulation is a less time-critical task than for spread spectrum signaling. The DPSK-demodulator gets its synchronization directly from the timing controller, and no digital correlation of the inphase and quadrature components is necessary to obtain "Chip-sync" since the data bits are not encoded. The demodulation is performed directly on the phase-split signal, and the demodulated data sequence is passed on to the 63 bit correlator to obtain "Message-sync". As for the spread spectrum messages, when "Message-sync" is obtained, a counter starts counting bit errors on the incoming data. The data bits are also here modulated using a 63 bits repeating PN-sequence.

A synchronized clock is important for time delay measurements. Different synchronization schemes have been used for the short path and the long path. For the short path two cesium-standards were used. The maximum drift and offset value for these standards is ± 10 μsec/month. Because of the drift, the standards had to be synchronized at regular intervals, and that was achieved with a rubidium manpack clock. The measured drift of the cesium-standards was always less than the maximum values. For the long path, manual synchronization was inconvenient, so a different scheme of synchronization was selected. Two independent systems were chosen; a Loran-C Reference Receiver and a Global Positioning System (GPS)-satellite receiver. The two systems were combined because the Loran-C signals do not provide absolute time which is needed for the transmission schedule of our HF-circuit. The number of GPS-satellites was still not adequate at the time of the measurements to provide a time reference at all times, but when signals *are* received, the GPS gives absolute time. The Loran-C Disiplined Frequency Standard provides several frequencies as outputs and these were used for continous timing and control in our system. The accuracy is 10^{-11}. The GPS-system was used as a controlling device for the Loran-C system. It provides time with an accuracy of 0.1 μsec and several frequencies as output. The GPS-receiver was regularly turned on during the measurements, and the frequencies from the Loran-C Reference Receiver were controlled against the GPS-frequencies. The difference between them was never larger than 1 μsec.

On the short path, two broadband, folded dipole antennas were used. They were installed as flat-top antennas with the maximum of their antenna gain pointing along the path. A

200 ohm resistance that provided the broadband characteristics caused some losses in the antenna. The length of the antenna was 60 m and a 300 W amplifier was used. For the long path, the 300 W amplifier was not available, so the power had to be reduced to 150 W. The folded dipole antennas were first used on this longer path, but the combination of a reduction in power and large losses in the antennas caused poor reception. The transmitting antenna was therefore exchanged to a directional rhombic broadband antenna, pointing towards the receiving site. The antenna legs were about 40 m. The receiving antenna was changed to an active (transistorized) vertical HF antenna, which is used for omnidirectional reception of low-angle sky waves.

The received messages were stored in binary format on an AT. For each day of measurements, two files were created; one that contained the conventionally modulated messages, and one that contained the spread spectrum messages.

5.2.2   Measured parameters

Bit errors are counted as described in Section 5.2.1. The minimum bit error rate (BER) that can be measured is $6.7 \cdot 10^{-4}$. For the spread spectrum messages where up to five multipaths can be recorded, bit errors are counted only for the strongest multipath. Relative amplitudes of the correlation peaks corresponding to the five different multipaths are stored separately.

The AGC-voltage from the Racal receiver adjusts the signal power to a certain level. A measurement of the total power in the channel is done by sampling the AGC-voltage at one instant of time during message reception. If several multipaths are present at the moment of sampling, the signal power should be distributed among the paths according to the relative amplitudes of the multipaths. Similarly, the noise power is measured prior to the first reception of a message by sampling the AGC-voltage at the receiver.

The conventional signaling is not able to resolve multipaths, since no spreading codes are used. Time delay measurements can therefore not be obtained with reasonable accuracy for these messages. For the spread spectrum messages this is possible, with an accuracy increasing proportionally to the bandwidth. The accuracy is therefore best for the 160 kHz bandwidth, but for the higher bandwidths/chiprates, the calculation of time delay becomes ambigous since there are several data bits in transit at the same time on the path. Only for the 5 kHz bandwidth can the time delay be calculated unambigously. The chiprate for this bandwidth is 2.5 kbit/s, which gives a resolution of multipaths of 400 µs. The accuracy to which the time delays can be determined is 1/bandwidth=200 µs. This corresponds to a height resolution of 30 km on a vertical incidence path. The delay range is 12.5 ms. For the time delay measurements we shall consider only this bandwidth, since the ambiguity and added complexity in the calculations for the longer bandwidths is not worth the increased accuracy. Besides, the measurements using the larger bandwidths did

not turn out well for reasons that we will come back to. The time of flight of one particular data bit within a message can be measured because the system allows very precise synchronization between transmitter and receiver. The position in time of the resulting correlation peak relative to the known transmission time defines the time of flight for that particular ionospheric path. Due to the slow time response in the transversal filter and of the AGC-voltage in the Racal receiver, one has to choose a data bit when the receiver system has stabilized. A counter delays the time delay measurement a certain number of data bits after "Message-sync" has occured. Time delays of maximum five different multipaths are stored for each message.

5.3   Deficiencies of the experimental system

The system was designed and put together in 1986 by two NDRE-engineers working full time over a period of a few months. The development phase was ended one year before the data analysis started. This is clearly not a good approach to design a field experiment, since experience must be gained for each experiment, and the measuring techniques adjusted accordingly. This is particularly so for ionospheric radio experiments where the transmitter and receiver are not co-located, and the media in between is highly variable. The analysis of our HF test data revealed a few major weaknesses of the system design that made some aspects of the recorded data not usable.

Direct sequence spread spectrum communication systems normally use a constant chip rate. The ratio in dB between the chip rate and the data rate is called the processing gain (PG) of the system and is determined by the number of chips in the selected code sequences. For a fixed bandwidth (chip rate) of the transitted signal, a large PG of the system means long code sequences and low data rate. Such a system is robust against noise bursts. DSSS systems use large bandwidths, and because of the PG of the system, the signal power density on the air can be low. Our HF test sounder is not a traditional DSSS system since it has constant PG for all bandwidths. The length of the code is fixed to 31 chips. The system will therefore not test the applicability and advantages of a spread spectrum system at HF for communication purposes. This was also not an expressed goal of the experiment, but should be borne in mind if comparisons with other experiments are made and if new experiments are to be designed.

The channel noise is measured prior to reception of each message, and the signal plus noise is measured during reception of a message. Both measurements are performed by sampling the AGC-voltage from the Racal receiver at one particular instant of time. The total noise power will increase considerably with increasing bandwidth, whereas the total signal power will remain the same for different bandwidths. At HF, the spectrum is very crowded and signals from all over the world may interfere within the signal bandwidth. The spectrum is also dynamic and might change character in seconds. In such an environment, signal and noise power should be measured over a period in time and

averaged, to reduce the effect of interference. It is not acceptable to measure these parameters by a snapshot in time as done in our HF tests. The data analysis revealed enormous spread in the data, so these measurements unfortunately had to be discarded.

Laboratory experiments show that two signals having different statistics (amplitude distribution) will produce different distributions of the correlation peak amplitude when passed through a correlator. Using the same fixed threshold for detecting correlation peaks for both signals, is therefore not correct. In our system, the same threshold is used for all bandwidths. The statistics of the noise will be different for each bandwidth, so when the signal plus noise is sampled and correlated at the receiver, a varying threshold for detection should have been implemented in order to measure propagation effects (the coherent bandwidth) at the same probability of false alarm. The threshold for each bandwidth can be determined by measuring only noise in the actual bandwidth and fixing the threshold at the level of a specific probability of false alarm. If the noise statistics for all bandwidths had been equal, a fixed threshold could have been used. Looking at the data, the number of messages received at 5 kHz spread spectrum signaling is about the same as for the 0.5 kHz conventional signaling. For increasing bandwidths the number of messages received, reduces steadily. There are nevertheless short periods in time where messages have been received *only* at the largest bandwidth, 160 kHz. This is expected to be caused by rapid time fading of the ionosphere and the very short duration, 5.86 seconds, of these messages. Because the threshold has been fixed at a certain level for all bandwidths, determining the coherent bandwidth of the ionosphere seems impossible.

I will also call it a "deficiency" of the system that an experiment like this has not been properly documented after completion. Sorting out the signal processing techniques used, has at times been a very frustrating and time consuming job.

6 COMPARISONS OF DATA AND PREDICTIONS

Data from the HF test sounder have been analyzed and reported previously. In Jodalen et al (61) we compared individual days of recorded data with ionograms, we looked at seasonal variations of measured quantities such as availability of the channel and virtual height of reflection, and we made the first comparisons with the prediction program IONCAP. In Jodalen and Thrane (3), (5) and Thrane et al (4), the data was compared with predictions from ICEPAC, and the influence of geomagnetic activity on propagation was emphasized. References (3), (4) and (5) made preliminary comparisons of the data with ICEPAC predictions, here we shall compare the data sets more thoroughly using a quantitative measure of the similarity. Only data sets from the short path will be compared in this chapter, while data sets from the long path can be found in Appendix B. We will first repeat the necessary definitions and terms in order to understand the comparisons, but a more detailed description can be found in Jodalen et al (61).

6.1 Methods of comparison

Because of the obvious deficiencies of the experimental system described in Section 5.3, only three measured quantities are useful; the bit error rate (BER) for the narrowband messages, time delay for the 5 kHz bandwidth and the occurence and relative amplitude of the multipaths. In this work we concentrate on virtual height of reflection derived from the measured time delay and reliability derived from the measured bit error rate, and compare these parameters with ICEPAC predictions.

We shall focus on the influence of geomagnetic activity on propagation in our comparisons, and we have used Bartels diagrams to select days where the geomagnetic activity has been low (Q≤4) and high (Q>4). Any finer division was difficult since the Q-index might change considerably in course of a day.

One observation period consists of 10 to 40 days, not necessarily consecutive, but days that show a marked tendency of either low or high geomagnetic activity. Each observed period is compared with predictions for Q=3 or Q=6. The predictions are made for the month within the period that contains the largest number of measurements. Each data set in the next section consists of one period of low observed Q with corresponding prediction, and one period of high observed Q with corresponding prediction. Both periods are from the same season.

6.1.1 Virtual height of reflection

To derive the virtual height of reflection, a one hop mode is assumed for both the short (285 km) path and the long (1280 km) path. This is in good agreement with predictions. Simple geometry and Breit and Tuve's theorem is used to calculate the virtual height of reflection from the measured time delay. Even though the delays of up to five multipaths have been measured, we have chosen to show in the subsequent figures only the strongest mode as a simple cross and possibly a second mode, if it exists, as a dot. The strongest mode is likely to be a one hop mode, whereas the nature of the additional modes is more uncertain. The figures in the next section display the virtual height of reflection for the 5 kHz messages from the selected period of time. There is one panel for each frequency. Days of low geomagnetic activity (defined later) are displayed in the left column, and days of high geomagnetic activity in the right column. For the short path, the maximum frequency displayed is 8.5 MHz, since there are very few data messages received at frequencies above 8.5 MHz on this path. The number of points reflects the number of messages received for that particular period. The accuracy to which the virtual height of reflection can be calculated, is roughly 30 km. The median of the data is drawn as a continous line, and the predicted virtual height is shown as triangles. The predicted virtual height is calculated for the most reliable mode independent of the reliability of the mode. Thus a reflection height is predicted even if the reliability is zero.

6.1.2 Reliability

Whereas the 5 kHz spread spectrum messages have to be used to display virtual height of reflection, the conventional 0.5 kHz messages will be used to display reliability because of the unsatisfactory thresholding for the spread spectrum messages, pointed out in Section 5.3. Inspecting the data shows in any case that the characteristics of the 0.5 kHz and 5 kHz messages are very similar.

From the number of bit errors counted for each message, reliability is defined as the percentage of the transmitted messages during the selected time period that are received with a BER smaller than 10%. The choice of 10% as a limit for the "acceptable" BER is somewhat arbitrary, but chosen so as to include most of the received messages. Certainly, this is not an acceptable limit for most communication purposes, but error rates in this order are frequently encountered on radio channels without channel coding. However, this selected, "acceptable" BER is used in the calculation of a required SNR to be given as input to ICEPAC, as we describe in the following:

Circuit reliability as calculated by ICEPAC was defined in Section 4.2. For correct comparison between data and predictions we must find the value of the required signal-to-noise ratio (RSNR) to be given as input to ICEPAC, that corresponds to our definition of observed reliability. The predicted reliability is very dependent on this input

parameter, i.e. an increase of the RSNR of 3 dB corresponds to a decrease of the reliability of 4-5 %.

To find the RSNR that corresponds to a certain BER after symbol decision is not a straightforward task, as pointed out in the following:

- If the noise at the receiver is white Gaussian, there is a one-to-one correspondence between channel SNR and output BER, determined by data rate, bandwidth and modulation scheme. However, the noise at HF is not white.

- There are rapid time variations on an HF channel, and the amplitude of the received signal, which is a sum of multipaths, will fluctuate in time. The amplitude is often assumed to be a Rayleigh-distributed random variable.

- The signal-to-noise ratio per bit E_b/N_0 will therefore also be a random variable. If the amplitude of the received signal is Rayleigh distributed, E_b/N_0 will be exponentially distributed.

- The mean E_b/N_0 has a one-to-one correspondence with the mean BER, but this formula is different from the formula in white noise. When flat fading (all frequencies fade in unison) is encountered, the mean E_b/N_0 has to be larger to produce the same BER.

- The influence of frequency selective fading is even more serious for the BER. In this case, a data rate larger than the multipath spread of the channel causes intersymbol interference. Additional transmitted power cannot then counteract the effect of distortion in the frequency spectrum of the signal.

ICEPAC does not take into account signalling rates and probabilities of spectrum distortion, but instead calculates a monthly mean SNR at the input of the receiver. If frequency selective fading occurs on a real path, the BER will be large, even if the SNR is large. In such a case, ICEPAC will incorrectly predict a high reliability of the channel.

However, ICEPAC can incorporate the effects of flat fading, if the appropriate RSNR is specified. For a correct specification in our case with DPSK-modulation, we should assume a Rayleigh distribution of the received amplitude and calculate the mean BER as a function of mean E_b/N_0. From this curve we could then select the mean RSNR corresponding to a BER of 10%. Instead, we have chosen to use a table given by Teters et al (2) that lists the RSNR for radio teletype service for given character error rates and modulation formats. The table includes the effect of Rayleigh fading, assuming a certain fading range which is not given. The exact meaning of the numbers in the table is not made clear in (2), but our interpretation of the numbers leads to the following calculations:

Character error rate can be converted to BER (P_B) by the formula

$$P_B = \frac{2^{k-1}}{2^k - 1} \cdot P_E \qquad (6.1)$$

where k is the number of bits per character and P_E is the character error rate (Sklar (62)). By plotting the tabulated RSNR's corresponding to different character error rates in a BER versus E_b/N_0-plot, the required E_b/N_0-value corresponding to a BER of 10^{-1} can be read off the diagram. Character error rates for *DPSK* were not listed in the given table, so FSK was chosen. This would bias the performance curve to give a too large RSNR since DPSK performs better than FSK. E_b/N_0 is related to S/N (where N is the noise in the occupied bandwidth) by:

$$\frac{S}{N} = \frac{E_b}{N_0} \cdot \frac{R}{BW} \qquad (6.2)$$

where BW is the bandwidth used and R is the data rate. S/N_0, which is the measure used in ICEPAC, can be obtained by multiplying with the bandwidth BW:

$$\frac{S}{N_0} = \frac{E_b}{N_0} \cdot R \qquad (6.3)$$

The value of E_b/N_0 at a BER of 10^{-1} can therefore be transformed into S/N_0 which is given as input to ICEPAC as the RSNR. In our calculations, k=5 in Equation 6.1. This results in $P_B = 0.516 \cdot P_E$. For a BER of 10^{-1}, $E_b/N_0 = 18$ dB on the extrapolated curve. $E_b/N_0 = 18$ dB corresponds to approximately $S/N_0 = 42$ dB for a given bandwidth of 0.5 Hz using Equation 6.2 and 6.3.

Reliability of data and predictions is presented in separate three-dimensional plots in the next section. The reliability is plotted as a function of hour of the day (UT) and frequency (MHz). The predictions are computed for one particular month, whereas the data are selected from a period not necessarily exactly overlapping the same month, but close enough so that seasonal trends do not cause discrepancies between data and predictions. Since reliability is defined as a percentage, it does not matter if the number of days in each observational period is different.

There are uncertainties associated with our interpretation of the table in Teters et al (2) that lists recommended RSNR's for given character error rates and modulation formats. The gain of the antennas selected from the standard antenna library in ICEPAC might also not correspond exactly to the gains of the actual antennas used in the measurements. Therefore, our choice of 42 dB as the RSNR might not be very accurate, and comparing the absolute levels of predicted and observed reliability should be done with caution.

Emphasis should rather be put on relative differences in diurnal and frequency variations between data and predictions.

6.1.3 Similarity coefficient

We have defined a "similarity coefficient", k(N), between predictions and data that expresses the normalized correlation between N measured and N predicted datapoints. It is defined as:

$$k(N) = \frac{\sum_{n=1}^{N}(x(n)-\bar{x})\cdot(y(n)-\bar{y})}{\sqrt{\sum_{n=1}^{N}(x(n)-\bar{x})^2}\cdot\sqrt{\sum_{n=1}^{N}(y(n)-\bar{y})^2}} \qquad |k(N)| \le 1 \qquad (6.4)$$

where N is the number of points to be correlated, x(n) is in our case the observed reliabilities, $\bar{x}$ is their mean value, y(n) is the predicted reliabilities and $\bar{y}$ their mean value. The normalization makes this measure independent of the absolute levels. In the next section, the similarity coefficients are calculated for each hour, for the four lowest frequencies (N=4), for each frequency for all hours (N=24), and for all hours and all frequencies (N=96). This measure will show where ICEPAC fails, that is, whether the differences between data and predictions are largest at certain times of day or at certain frequencies.

6.2 Datasets compared

6.2.1 September/October/November 1987

13 days with quiet, and 24 days with disturbed geomagnetic conditions have been selected from this period around autumn equinox.

Virtual height.
Figure 6.1 shows the measured and predicted virtual heights of reflection.

The interpretation of virtual heights larger than 300 km on this path is ambiguous. They may represent multiple-hop paths.

For f=3.0 MHz, reflections occur both from the F_2-layer and from the E-layer at all times of day. As the frequency increases above the E-layer MUF, the solar E-layer is not able to reflect the waves. They are instead reflected from the F_2-layer. At night, the auroral E-layer is dense enough to reflect the radio waves even at higher frequencies.

The only fundamental difference between the predictions for Q=3 and Q=6 is that for Q=6 auroral E-layer reflections are predicted more frequently for the hours around midnight.

In general, ICEPAC performs reasonably well during daytime for both levels of geomagnetic activity. The predictions are poor at pre-midnight hours for Q=6 where the data shows that more E-layer reflections occur than predicted. The data also reveal that prediction is difficult at f=3.0 MHz.

Reliability.
Reliability of data and predictions are shown for low geomagnetic activity in Figure 6.2 and high geomagnetic activity in Figure 6.3. A noteable difference between the two plots of data is the pronounced reduction of reliability for the hours 4-8 UT for Q>4.

The two predictions are very similar, but the MUF is slightly larger around midnight and at 17 hours for Q=6. Both predictions exhibit a day time solar zenith angle dependence of the MUF, whereas this feature was only observed for Q≤4.

Similarity coefficients.
The predictions of MUF and of reliability are too optimistic both for quiet and disturbed conditions. The total normalized similarity coefficient between data and predictions (Equation 6.4) over all frequencies and hours is 0.66 for Q=3 and 0.56 for Q=6. Similarity coefficients for each hour over all (4) frequencies are plotted in the left part of Figure 6.4. The similarity coefficients are in general larger for Q=3 than for Q=6. The similarity coefficients for each frequency over all hours shown in the right part of Figure 6.4 shows the same trend. In addition, they are in general lower than the similarity coefficients in the left part of the figure. We believe that the low similarity coefficients for each frequency expresses the discrepancy between diurnal variation of data and predictions.

Q≤4 (data), Q=3 (predictions) Q>4 (data), Q=6 (predictions)
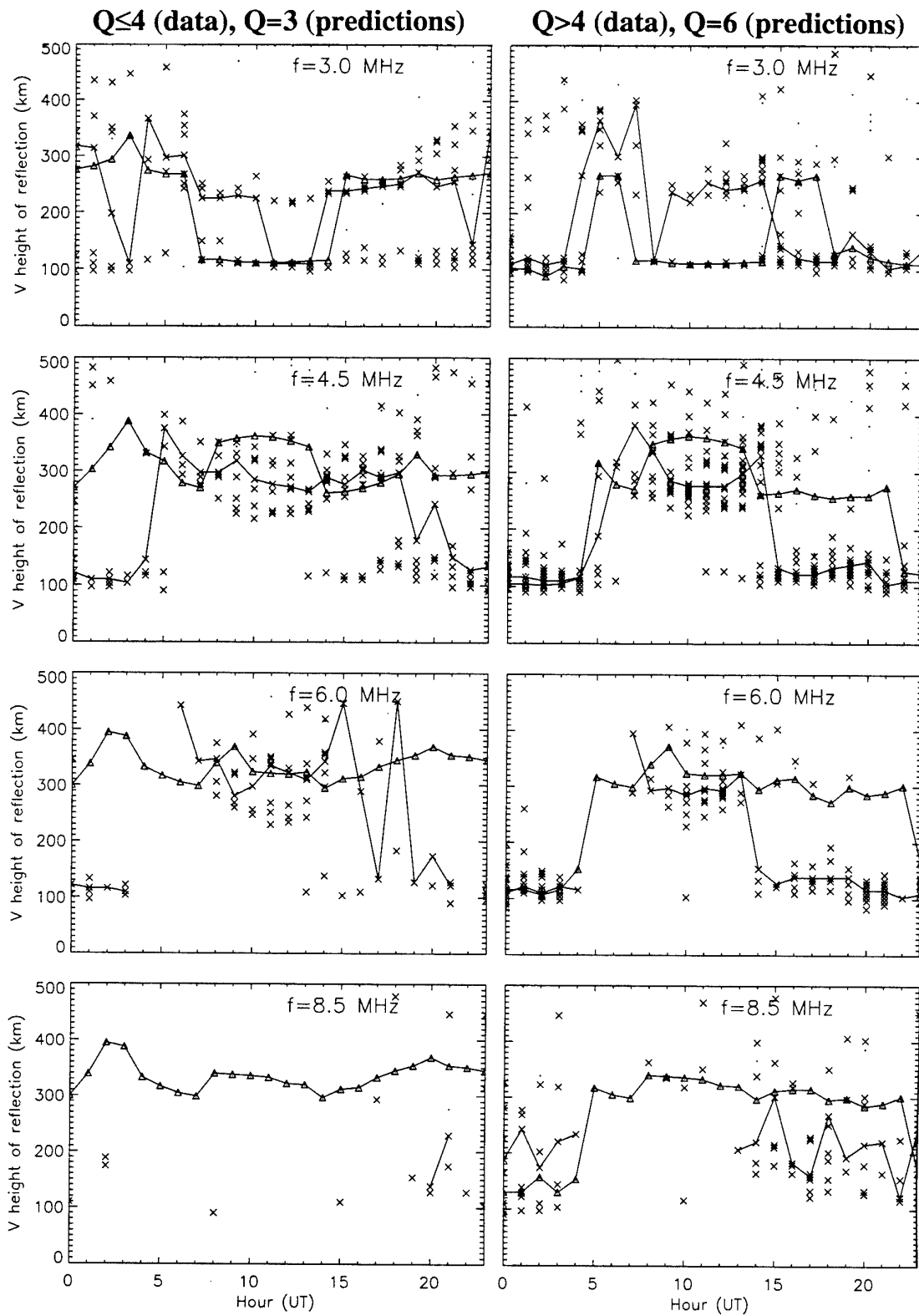
Figure 6.1 Virtual height of reflection, Andøya-Alta (285 km), September/October/
November 1987. Median of data drawn as a continous line. Small dots
*indicate multipath. Predicted virtual height shown as triangles. SSN=39*

Q≤4:
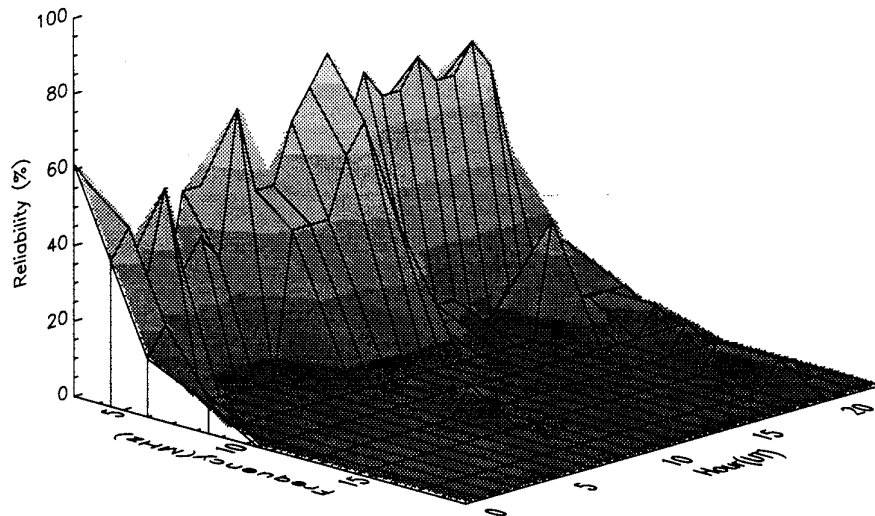
Q=3:
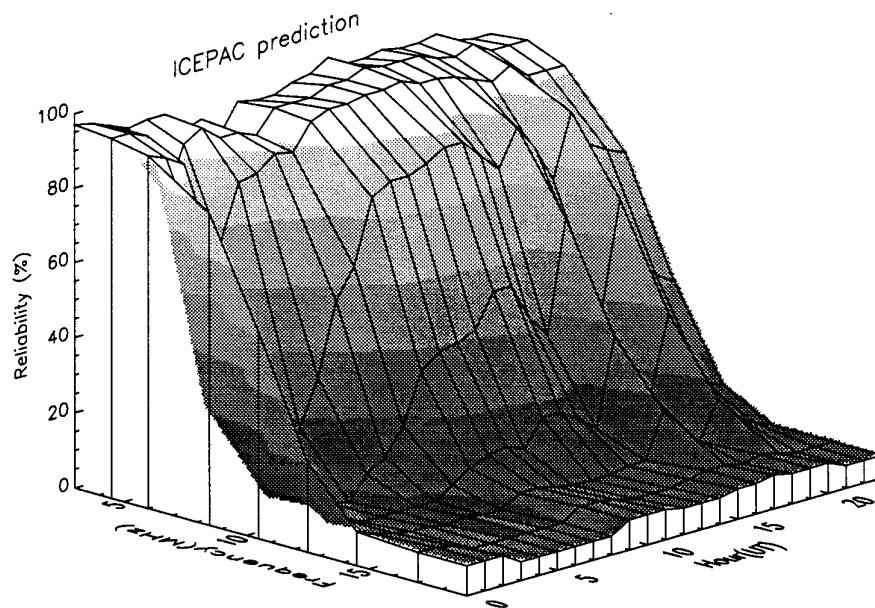
Figure 6.2 Reliability of data for September/October/November 1987 above, prediction for September below (SSN=39). Andøya-Alta (285 km)

Q>4:
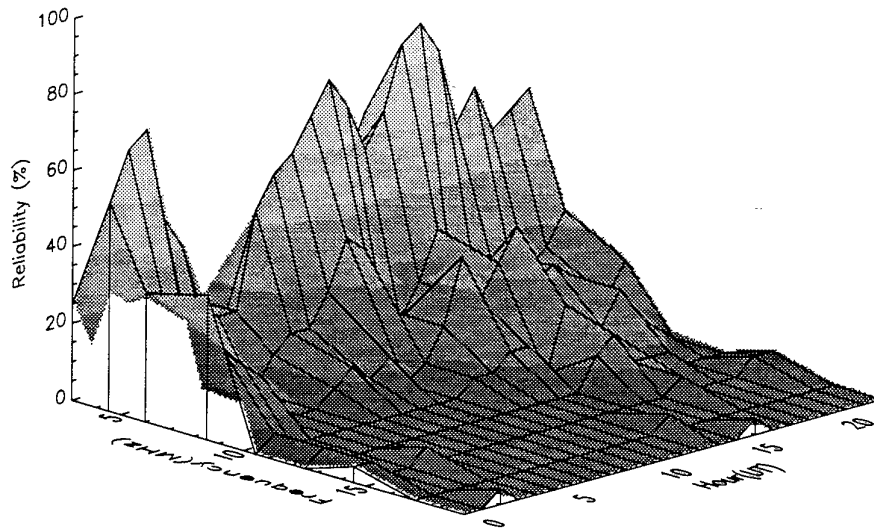
Q=6:
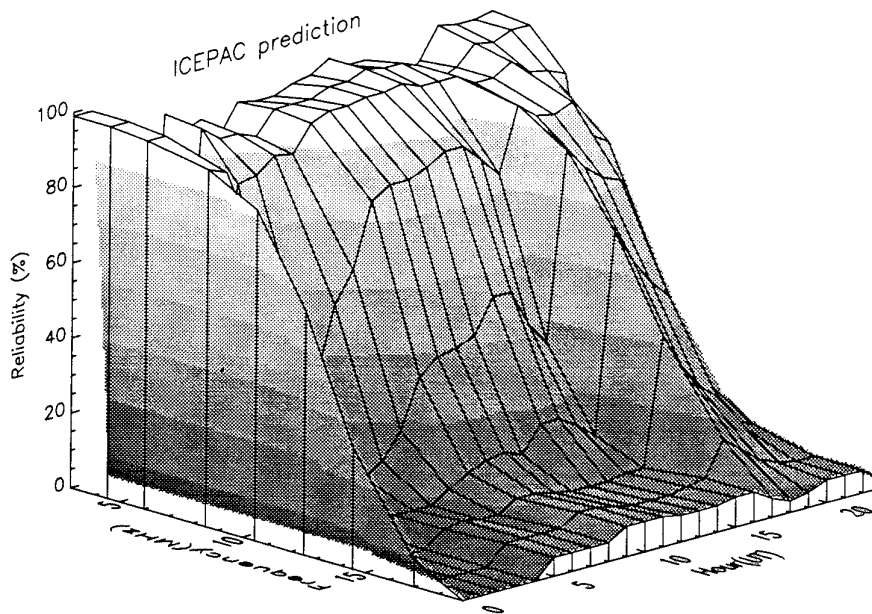
*Figure 6.3   Reliability of data for September/October/November 1987 above,
prediction for September below (SSN=39). Andøya-Alta (285 km)*
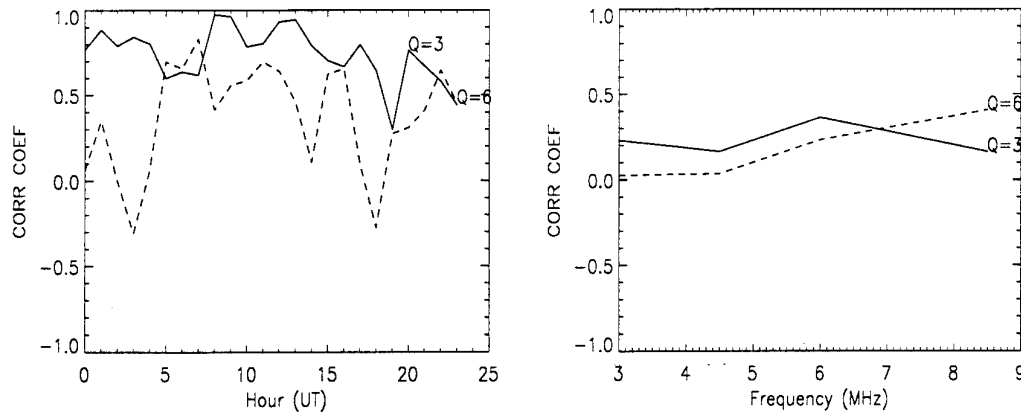
*Figure 6.4   Similarity coefficients (corr coef) between reliability of measured data and
reliability predicted by ICEPAC. Andøya-Alta (285 km), September/
October/November 1987, SSN=39*

6.2.2   March/April 1988

16 geomagnetically quiet days and 17 disturbed days were selected around spring
equinox.

Virtual height.

The approximately same number of days for the two periods enables us to see a
distinction between the two reflection patterns in Figure 6.5. More messages have been
received for Q≤4 than for Q>4. The quiet period shows a more well defined, solar zenith
angle dependent diurnal variation. The data of the disturbed period shows a wide spread
of reflection heights during daytime, but fairly well defined auroral E-layer reflections at
night.

The comments made earlier concerning the predictions of virtual height for the
Sept/Oct/Nov1987 data set, also applies to this data set.

Reliability.

Observed and predicted reliability in Figures 6.6 and 6.7 display the same features as for
the previous data set.

Similarity coefficients.

The overall similarity coefficients are for Q=3 0.71, and for Q=6, 0.54. The similarity
coefficients for each hour over all frequencies, and for each frequency over all hours are
shown as the left and right part of Figure 6.8, respectively. Again, the characterization is
the same as for the previous data set.

Q≤4 (data), Q=3 (predictions) **Q>4 (data), Q=6 (predictions)**
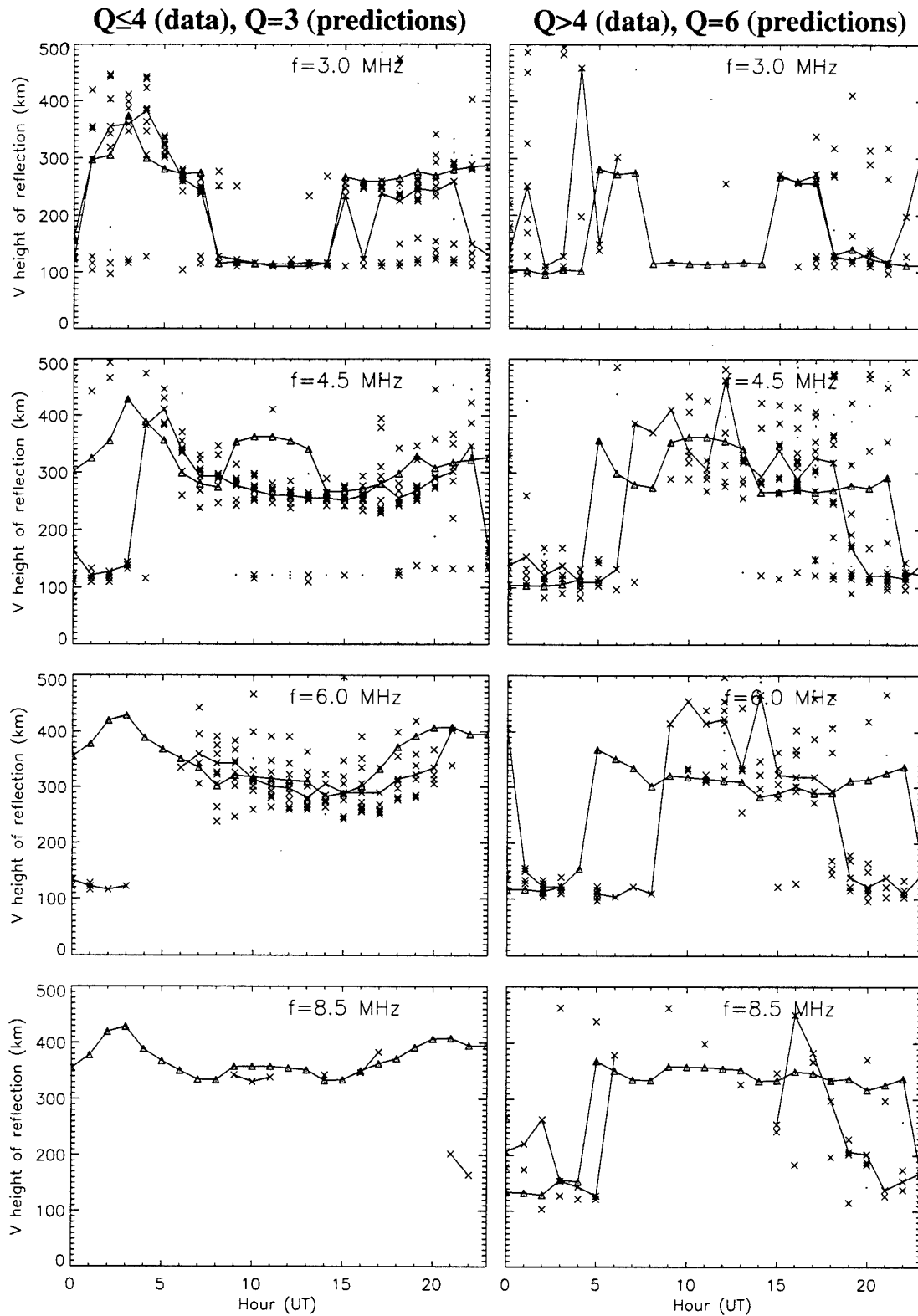
Figure 6.5   Virtual height of reflection, Andøya-Alta (285 km), March/April 1988.
Median of data drawn as a continous line. Small dots indicate multipath.
Predicted virtual height shown as triangles. SSN=71

Q≤4:
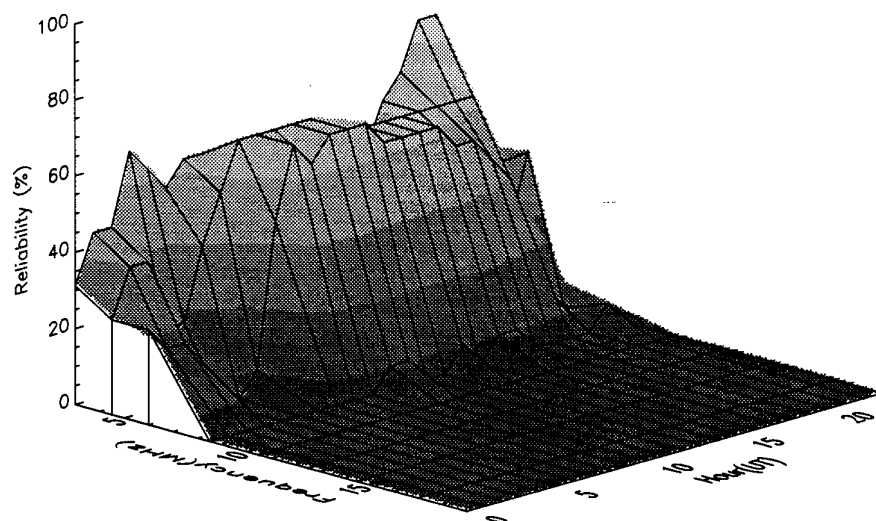
Q=3:
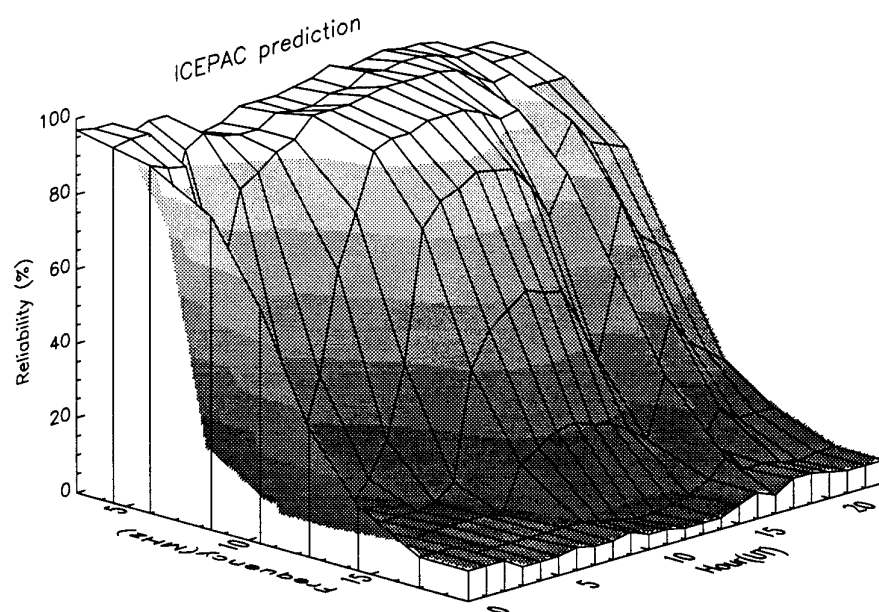
Figure 6.6   Reliability of data for March/April 1988 above, prediction for March
below (SSN=71). Andøya-Alta (285 km)

Q>4:
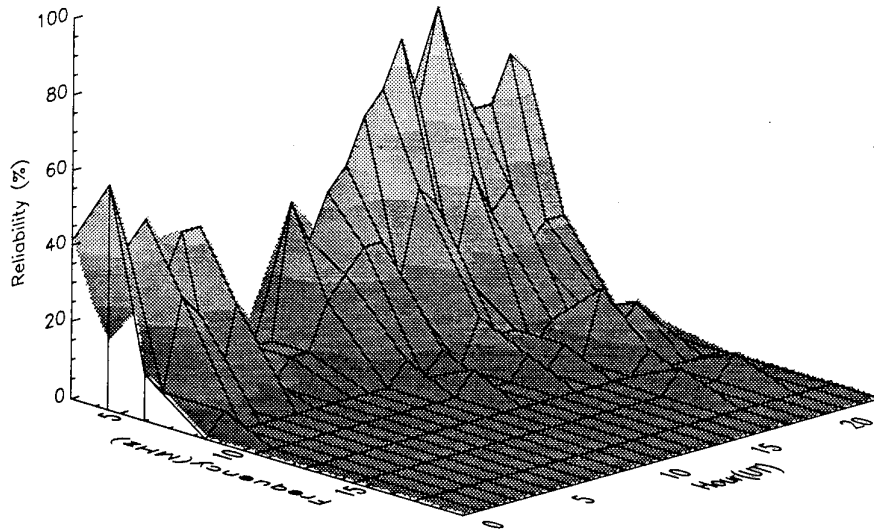
Q=6:
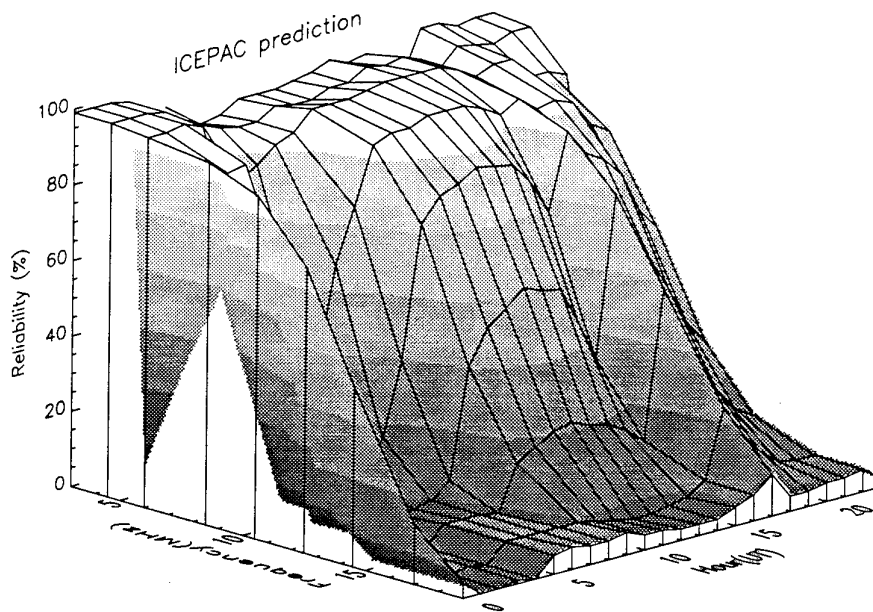
Figure 6.7   Reliability of data for March/April 1988 above, prediction for March
below (SSN=71). Andøya-Alta (285 km)
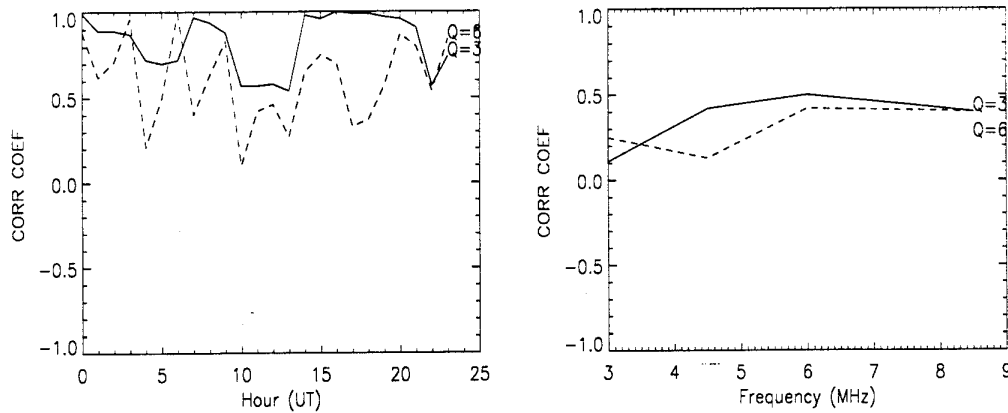
Figure 6.8   Similarity coefficients (corr coef) between reliability of measured data and reliability predicted by ICEPAC. Andøya-Alta (285 km), March/April 1988, SSN=71

6.2.3   June/July/August 1988

From this summer period, 19 days constitute the quiet period and 22 days the disturbed period.

Virtual height.

Inspecting the plot of virtual height (Figure 6.9), the reflection pattern is different from the two equinox data sets shown previously. The solar E-layer is denser, which gives more E-layer reflections at all frequencies. The strong solar E reflects all of the transmitted messages at 3 MHz during day time and makes the lowest frequency easier to predict.

For this data set the number of received messages seem to be almost equal for Q≤4 and Q>4. The spread of the reflection heights is also similar for quiet and disturbed conditions, except possibly for f=6 MHz where the spread is slightly larger for Q>4.

The predictions of virtual height perform reasonably well for both Q=3 and Q=6 for this summer period.

Reliability.

Neither the measured nor the predicted reliability in Figures 6.10 and 6.11 exhibit any pronounced solar zenith angle variation of the MUF. This is due to the midnight sun at this time of year.

The reduction of reliability in the morning hours 5-9 UT for Q>4 can be seen also for this data set.

The predictions for August 1988, Q=6, shows a black-out of communications a few hours around midnight. The reason is as pointed out in Thrane and Jodalen (4), that a large auroral E-layer (f_oE) causes ICEPAC to calculate excessive ionospheric absorption, which has no physical relevance.

Similarity coefficients.

The similarity coefficients between data and predictions are particularly small for the hours around midnight for Q=6. The similarity coefficients for each frequency over all hours is also very small, and k(24) for Q=3 at certain frequencies is smaller than for Q=6. The total similarity coefficient over all frequencies and hours is 0.65 for Q=3 and 0.48 for Q=6.

Q≤4 (data), Q=3 (predictions)   **Q>4 (data), Q=6 (predictions)**
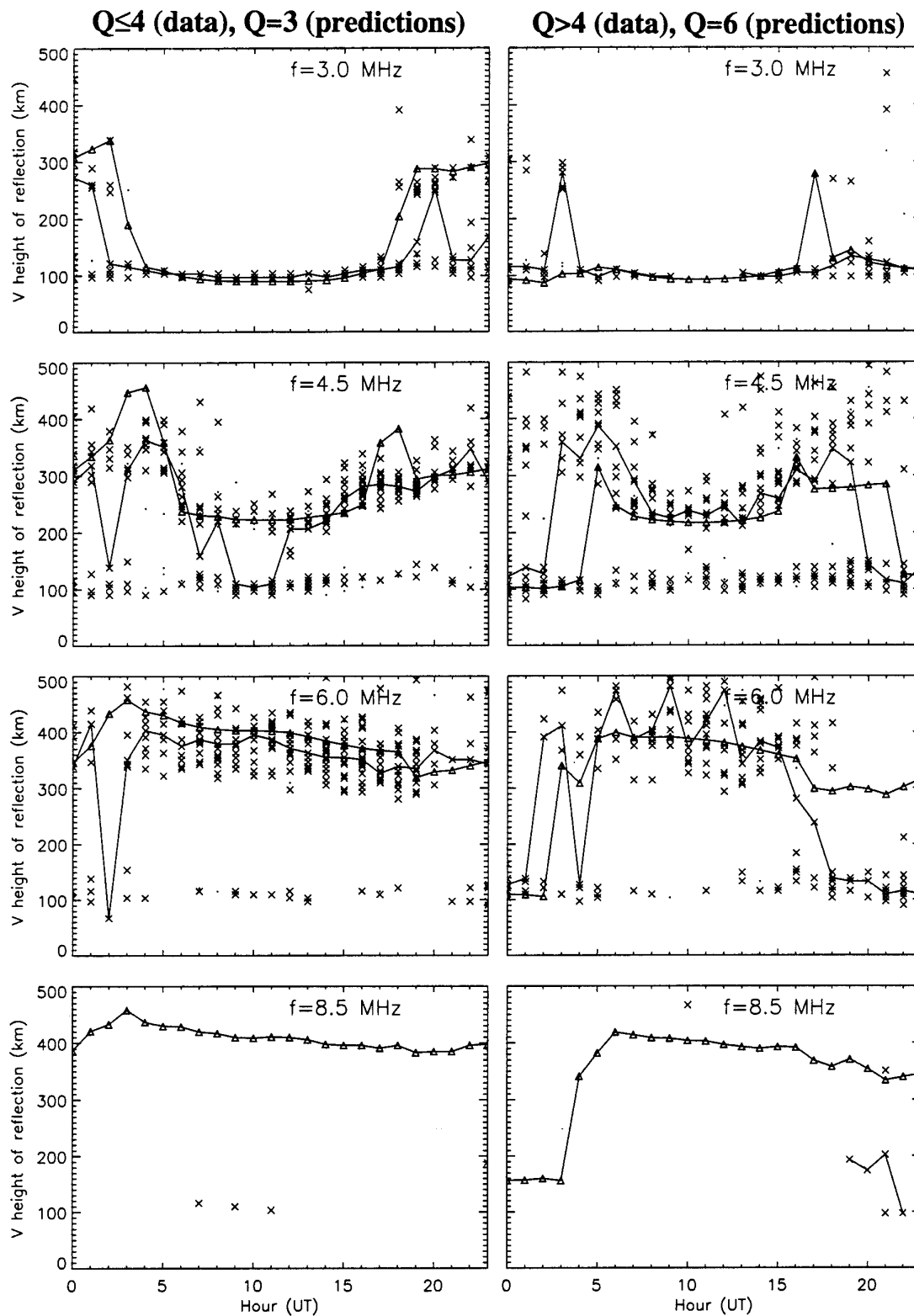
*Figure 6.9   Virtual height of reflection, Andøya-Alta (285 km), June/July/August 1988.
Median of data drawn as a continous line. Small dots indicate multipath.
Predicted virtual height shown as triangles. SSN=109*

Q≤4:
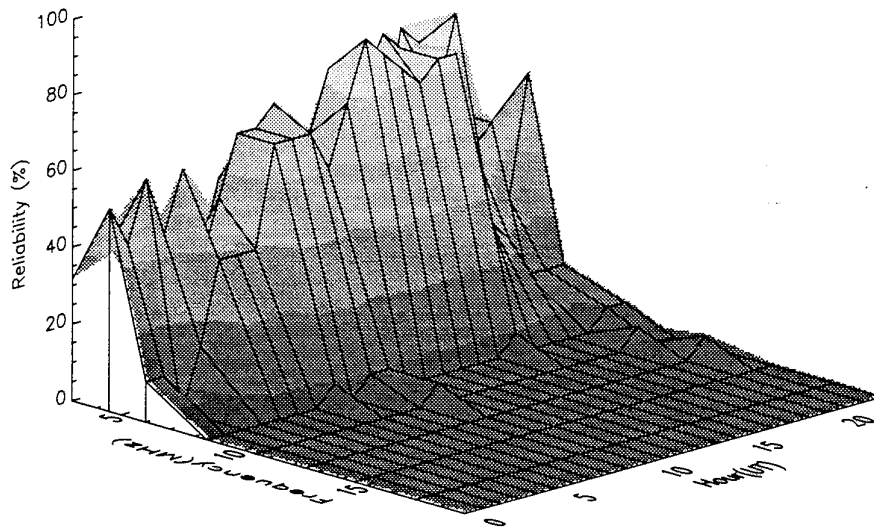
Q=3:
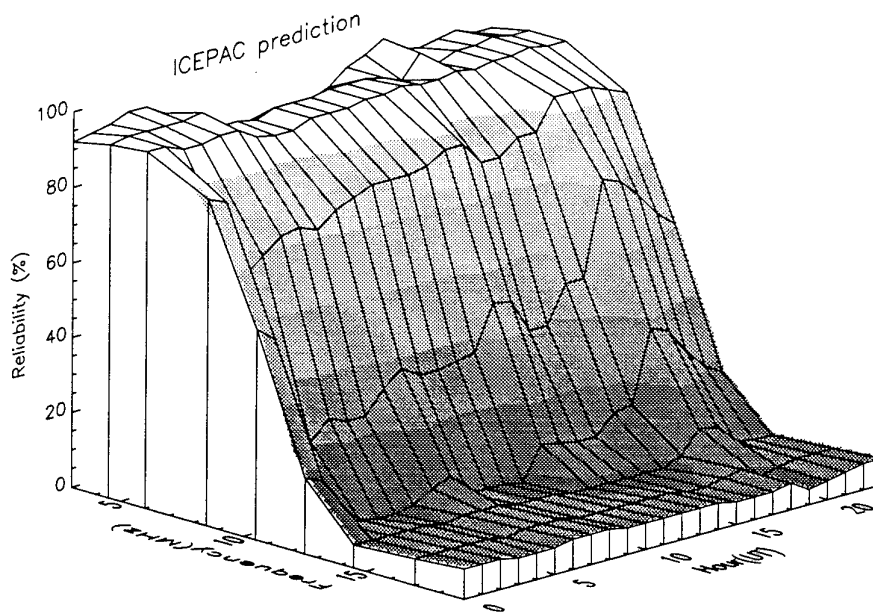
Figure 6.10   Reliability of data for June/July/August 1988 above, prediction for July
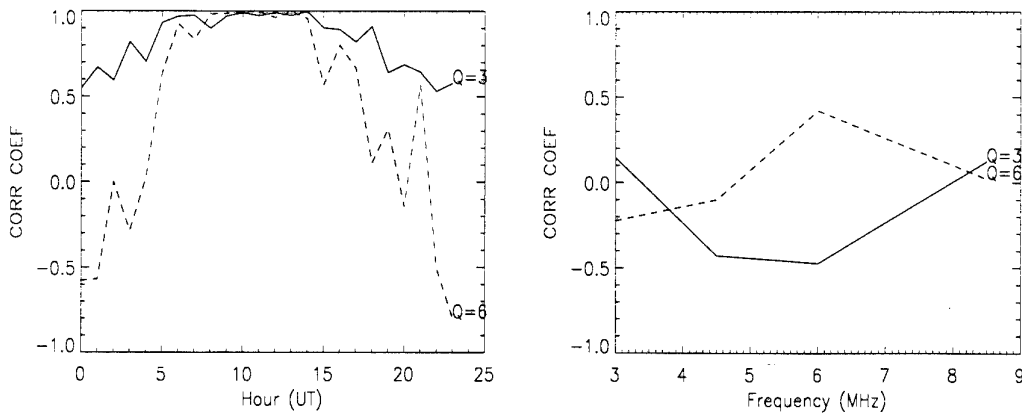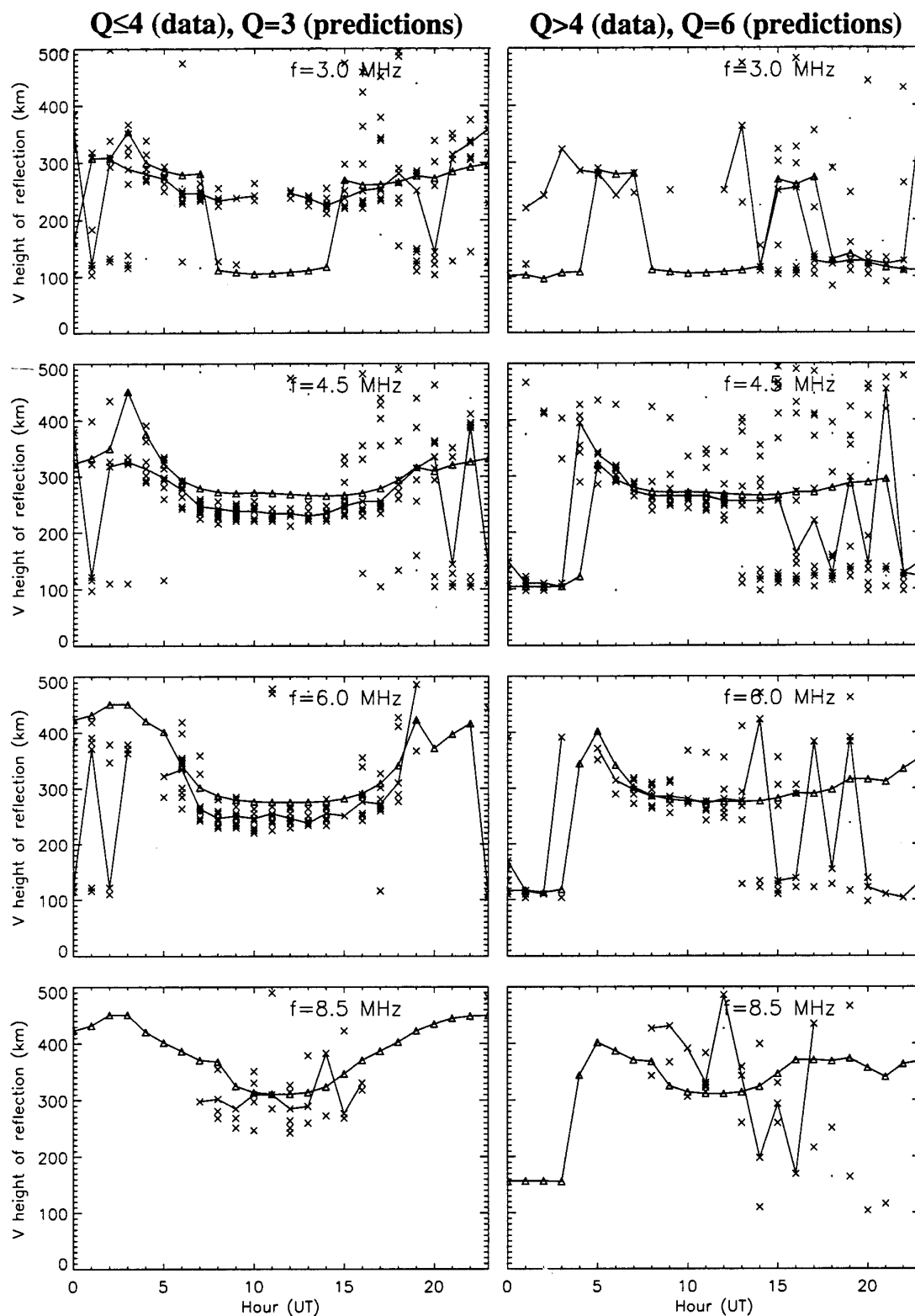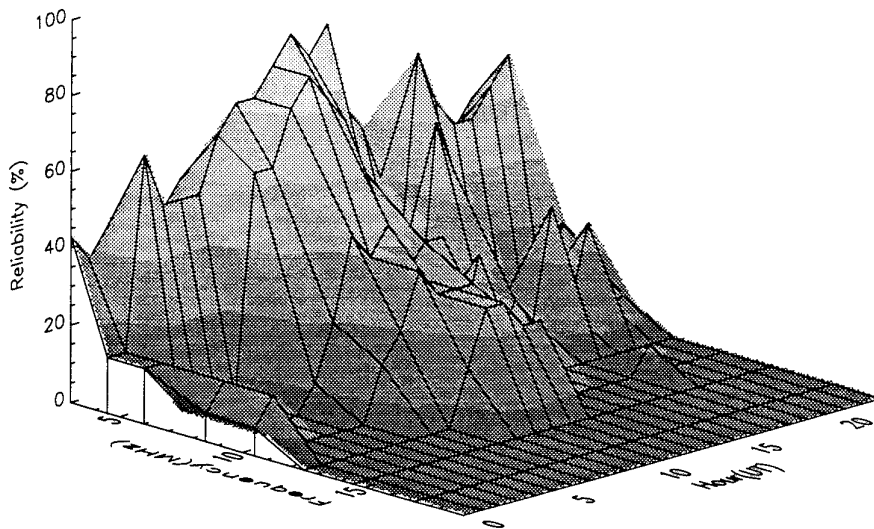*below (SSN=104). Andøya-Alta (285 km)*

Q>4:
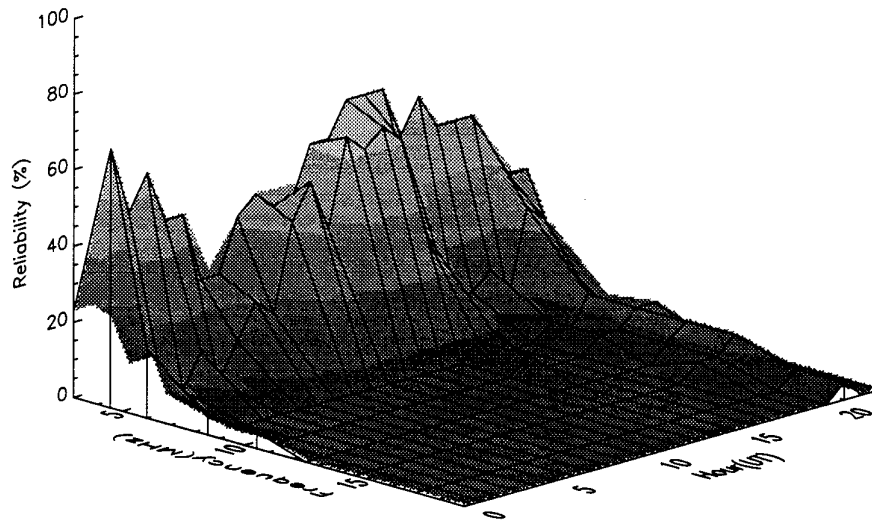
Q=6:
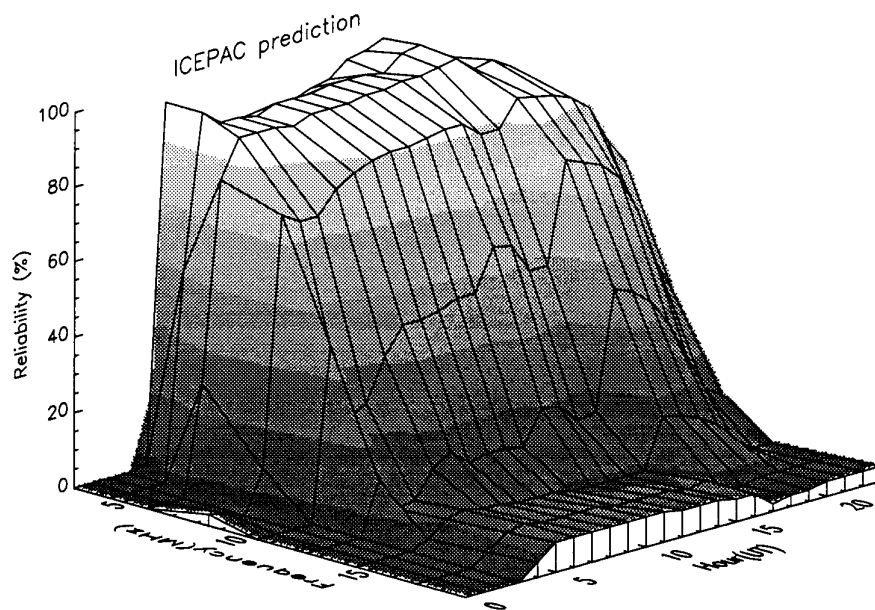
*Figure 6.11   Reliability of data for June/July/August 1988 above, prediction for August
below (SSN=114). Andøya-Alta (285 km)*

*Figure 6.12 Similarity coefficients (corr coef) between reliability of measured data
and reliability predicted by ICEPAC. Andøya-Alta (285 km), June/July/
August 1988, SSN=109*

6.2.4 October/November 1988

Due to equipment failure, we have no data from wintertime on the short path. Instead,
we show here a second data set from around autumn equinox. 14 days constitute the
quiet period and 16 days the disturbed period. Virtual height is displayed in Figure 6.13,
reliability of data and predictions in Figure 6.14 and 6.15 and similarity coefficients in
Figure 6.16.

Inspecting the figures, basically the same features are observed for this data set as for the
two other equinox data sets, Section 6.2.1 and 6.2.2. The total similarity coefficient is
0.63 for Q=3 and 0.61 for Q=6.

Q≤4 (data), Q=3 (predictions)

Q>4 (data), Q=6 (predictions)

Figure 6.13   Virtual height of reflection, Andøya-Alta (285 km), October/November 1988. Median of data drawn as a continous line. Small dots indicate multipath. Predicted virtual height shown as triangles. SSN=125
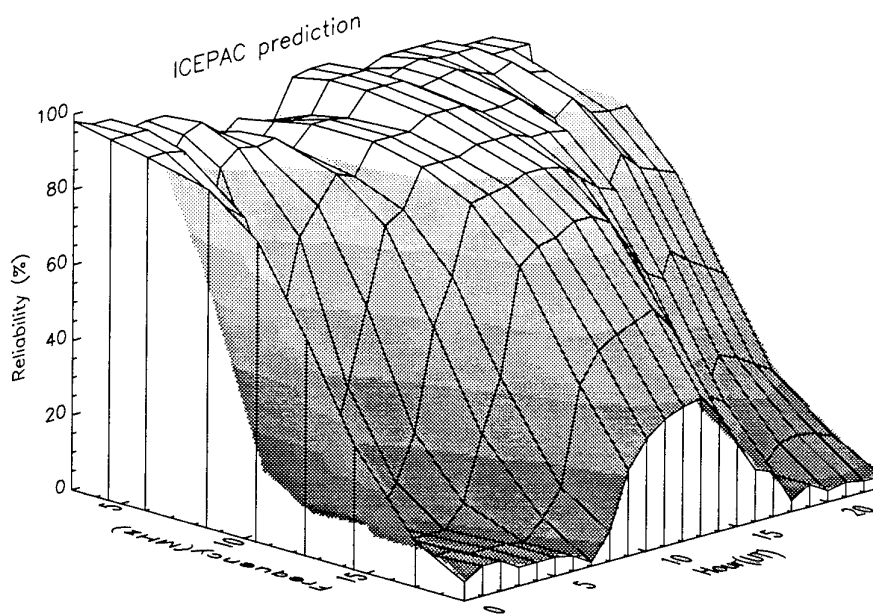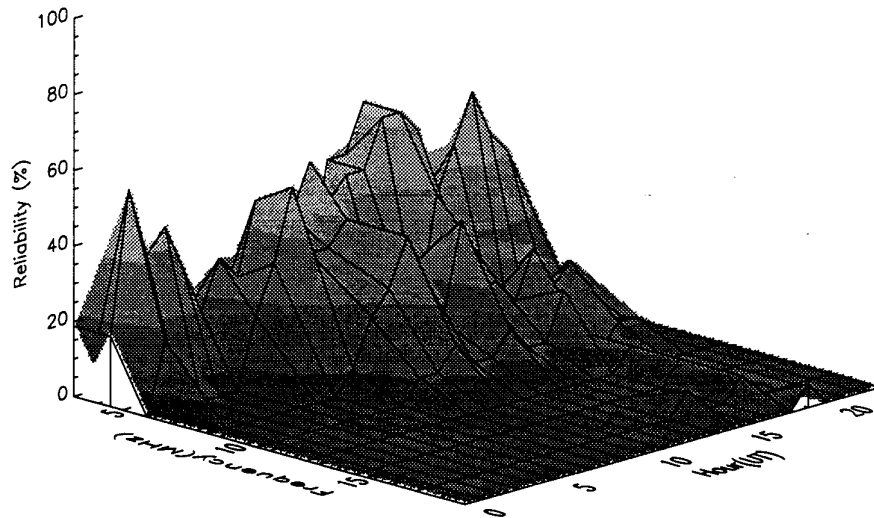
Q≤4:

Q=3:

*Figure 6.14   Reliability of data for October/November 1988 above, prediction for
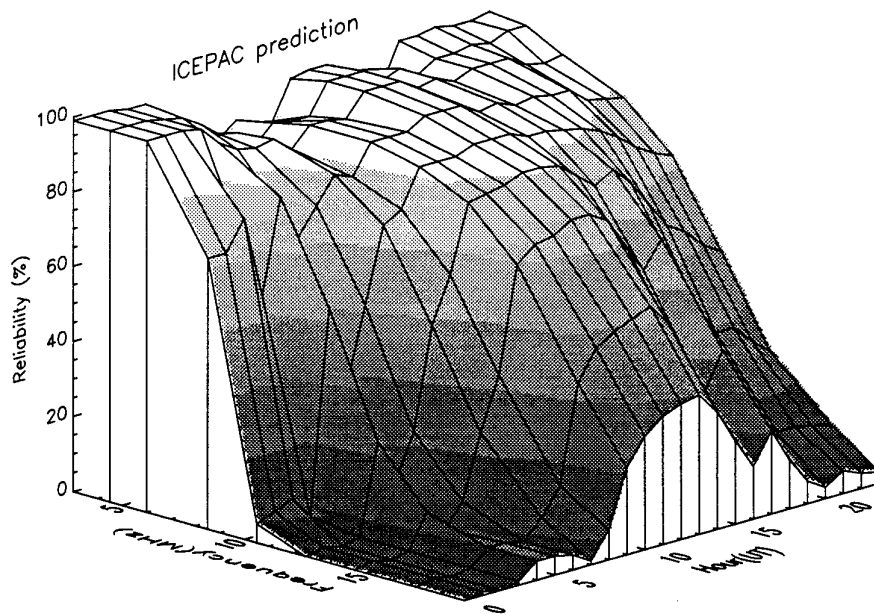October below (SSN=125). Andøya-Alta (285 km)*

Q>4:

Q=6:

Figure 6.15   Reliability of data for October/November 1988 above, prediction for October below (SSN=125). Andøya-Alta (285 km)
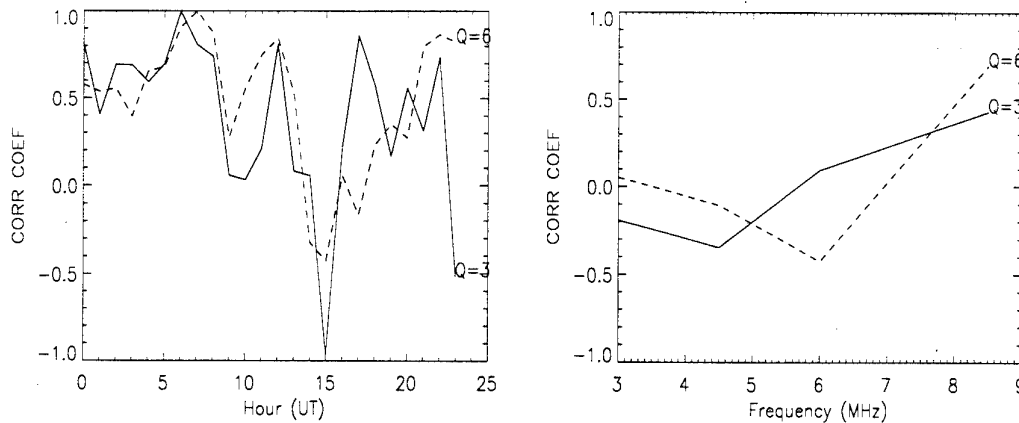
*Figure 6.16   Similarity coefficients (corr coef) between reliability of measured data
and reliability predicted by ICEPAC. Andøya-Alta (285 km), October/
November 1988, SSN=125*

6.3   Discussion

Virtual height.

From the four data sets in the previous section, we may sum up the observations:

- More messages have been received during the quiet periods than during the disturbed periods. An exception is the summer data set, where approximately an equal number of messages have been received.

- For the summer data set, the reflection patterns are very similar for the quiet and disturbed periods, whereas for the equinox data sets, the quiet periods show a more well defined, regular solar zenith angle variation than the disturbed periods. The data of the disturbed periods show a wide spread of reflection height during day time. More night-time auroral E reflections are noticed for all data sets for Q>4.

For daytime, these comparisons between reflection patterns show that communication is less reliable for disturbed than for quiet periods, as well as more dynamic with a wider range of electron densities in the E and F-regions. In contrast, communication during disturbed conditions is more reliable at night due to dense auroral E. These differences between disturbed and quiet conditions are less pronounced in summer. We believe that the increased electromagnetic radiation in summer masks some of the auroral disturbances.

At all times of day some virtual heights are larger than 300 km and their interpretation is thus ambiguous. A typical solar E-layer around noon is not dense enough to reflect a two-hop mode because of a small angle of incidence. We therefore believe that the

ambiguous F_2-virtual heights around noon are true F_2-reflections. In contrast, a typical auroral-E at night is dense enough to reflect a two-hop mode for frequencies up to and including 6.0 MHz. So the ambiguous F_2-virtual heights at night can very well be two-hop E-reflections.

The predictions of virtual height agree well with the data for the summer data set and during daytime for the equinox data sets. ICEPAC predicts, but underestimates, the observed increase of occurence rate of auroral E reflections during disturbed conditions.

Reliability.
The most striking feature of the plots of measured reliability in the last section is the reduction of reliability in the morning hours for Q>4. It can be explained by the morning absorption at high-latitudes. Tromsø, which is the approximate mid-point of the test path, has a geomagnetic latitude of ~67°N. According to Ranta (22) this is the latitude at which maximum absorption occurs in Norway. The soft-to-medium precipitating particles from the solar wind (<10 keV) that cause increased magnetic activity and visible aurora in the F-region around midnight, are followed by harder particles (<300 keV) that penetrate to the D-region and cause increased absorption of radio waves in the morning, see Figure 2.1, Section 2.8.2. Figure 2.1 also shows that minimum precipitation at 67°N is expected between 18-22 geomagnetic time. In the data sets, maximum reliability occurs for these hours (16-20 UT) except for the summer data set where the maximum occurs earlier.

The latitude of Tromsø is approximately the same as that of Kevo in Finland. Figure 2.3 in Section 2.8.3 (Ranta (22)) shows a maximum of absorption from 6 to 9 UT which corresponds exactly to our observed maximum of absorption from 5 to 8 UT. The second, smaller maximum of absorption around midnight in Figure 2.3 is also observed in our data (minimum reliability).

The minimum reliability in the morning hours for Q>4 is more pronounced for two of the equinox data sets than for the summer data set. This is in agreement with Ranta (22). In contrast, the third data set from equinox, October/November 1988, shows a smaller reduction of reliability in the morning hours, similar to the summer data set. A possible explanation is that half of the days are in November, which would make the data show winter characteristics, such as less pronounced variation with time of day.

Again in agreement with Ranta (22), the morning and midnight maxima of absorption are of the same magnitude for the summer data set, whereas for the equinox data sets, the morning maximum is larger.

The data from the quiet periods show a solar zenith angle variation with maximum reliability and MUF around local noon.

The diurnal and seasonal differences described here between quiet and disturbed conditions are not incorporated in the predictions of reliability. Besides, the predictions are in general too optimistic, both in the prediction of reliability and of MUF.

Similarity coefficients.
Table 6.1 gives the normalized similarity coefficients over all frequencies and hours for all data sets.

- The overall similarity coefficients are in general larger for Q=3 than for Q=6, as expected.

- The individual similarity coefficients for each frequency and each hour displayed in the last section were also in most cases larger for quiet conditions.

- The individual similarity coefficients for each frequency over all hours are in general smaller than similarity coefficients for each hour over all frequencies.

These results show that predictions of diurnal variation, and in particular, propagation predictions during disturbed conditions need to be improved.

k(N) for time period:	Q=3	Q=6
September/October/November 1987, SSN=39	0,66	0,56
March/April 1988, SSN=71	0,71	0,54
June/July/August 1988, SSN=109	0,65	0,43
October/November 1988, SSN=125	0,63	0,61

Table 6.1   Similarity coefficients between measured and predicted reliability on the short path for all hours and frequencies

General remarks.
The HF experiment was operated in 1987, two years before the maximum of sunspot cycle 22. This makes the geomagnetic conditions comparable to the year 1969, two years before the maximum of sunspot cycle 20. In 1969, the auroral oval covered Tromsø approximately 21 % of the total time (Section 3.4). The probability of auroral coverage is largest at night, and we have observed typical auroral phenomenon in our data sets at night. Auroral absorption can, however, also be observed at locations equatorward of the auroral oval.

The present prediction algorithms of virtual height can probably be improved somewhat for disturbed conditions, particularly for hours before midnight. However, it is more important to develop an improved, realistic prediciton of reliability where the fundamental differences between quiet and disturbed conditions are incorporated. The modelling of absorption should be controlled by the solar zenith angle during quiet conditions, whereas it should be controlled by precipitating particles from the solar wind during disturbances.

The method of comparison merits a comment: Signal strength data were not available and we have used bit error rates as a measure of the signal-to-noise ratio. This measure includes in addition to absorption, also flat and frequency selective fading, interference and white noise that will all degrade the measured BER. The *predicted* signal-to-noise ratio includes expected absorption and different sources of noise (man-made, atmospheric, galactic) that together have a white noise distribution. The predicted reliability contains protection against a certain range of flat fading because the required SNR in the table given by Teters et al (2) is used. Since the measured data contain more sources of impairment than the predictions, deducing signal characteristics from the BER and comparing them with predicted SNR may give wrong conclusions. Anyway, measurements have shown Clutterbuck (63) that the amount of interference in the northern part of Norway is very small, and should therefore not be a major source of signal degradation. Frequency selective fading might occur even if our signalling rate is as low as 250 bits/s. In spite of the difficulties encountered when comparing measured BER to predicted signal-to-noise ratioes, we feel that our similarity analysis has to some extent overcome these problems and provides a meaningful comparison of data and predictions.

6.4   Results from the long path

For the long path the distance between transmitter and receiver was 1230 km. The geographical positions of the transmitter and receiver were 60.07 N, 11.15 E and 69.90 N, 23.20 E, respectively. The signals now propagated in the south-north direction from a mid-latitude location into a high-latitude region, possibly disturbed by auroral events. The degree of auroral disturbances on this path is expected to be less than on the short path. The MUF for this path is in the range 6 MHz to 20 MHz. The most probable mode is nevertheless a one-hop mode, according to predictions, and the same methods of analysis are used for the long path as for the short path. However, for the long path the time delay of a two-hop E-mode is about 4.56 ms, which corresponds to a virtual height of 285 km on a one-hop path. Thus, virtual heights above 285 km are ambiguous. One difference from the short path is that *all nine* frequencies are encountered in the calculation of similarity coefficients.

The measurements were conducted on the long path from the beginning of 1990, which was less than a year after the maximum of sunspot cycle 22, until 1992. Here we will report on the main results from the long path, figures and a detailed description of each data set can be found in Appendix B.

The interpretation of the propagation results for this 1230 km path turned out to be much more difficult than for the short path. A larger number of different modes can propagate on a longer path, and besides, the transmitter is almost certainly south of the auroral disturbed region, whereas the receiver site will quite often be covered by the

auroral oval. Thus the propagation paths may or may not experience auroral disturbances. The ICED-model classifies the midpoint of this path in the following way:

- For Q=3, the midpoint is entirely a low/mid-latitude location at all times. For hours around midnight this low/mid-latitude location is in addition classified as a sub-auroral trough point experiencing a depletion of the F_2 electron densities.

- For Q=6, the midpoint of the path is mostly classified as a low/mid-latitude location, but for the winter, spring and autumn data set, a few hours around midnight are classified as auroral night. The midnight hours for the summer data set are classified as auroral day and auroral sunrise/sunset points. The sub-auroral trough covers the midpoint of the path also for Q=6, but a few hours earlier in the evening and a few hours later in the morning than for Q=3. The classification of the midpoint as a sub-auroral trough point is similar for all seasons (all data sets).

The long path is a mid-latitude path in the predictions most of the time, and there is hardly any difference between predictions for Q=3 and Q=6 for the same season. This applies to both virtual height and reliability. There are however, differences between predictions and observations, as noted in the following:

Virtual height.
Most of the measurements do not show any difference between reflection patterns (virtual height) for quiet and disturbed conditions. The autumn data set does not fit this description, but we believe the reason is that most of the data for the quiet period are from November and most of the data from the disturbed period are from September, so that the difference may be due to seasonal changes.

Data points here plotted as single-hop modes with virtual heights larger than 285 km may instead be multi-hop modes reflected lower in the ionosphere. Some of the F_2-reflections around noon can, according to this, be considered as ambiguous. Since the solar E-layer is non-existent or weak in winter and at equinox, and absorption at mid-latitudes maximizes around noon, we believe that the observed virtual heights between 285 km and 400 km around noon *are* one-hop F_2 reflections. The observed reflections at night at 400-500 km altitude are more likely caused by multiple E-reflections from auroral E. However, the largest frequencies in the measurement set are expected to penetrate even a dense auroral E-layer on a two-hop path. These observed reflections may also be caused by irregular ionization in the F_2-region (spread-F).

For frequencies at and above 10.5 MHz at night, ICEPAC predicts a steady E_s-layer at an altitude of 110 km. The observed virtual heights are also in the E-region, but 30-40 km higher. Whether the observations are auroral-E reflections or sporadic-E reflections is impossible to say. This difference between observations and predictions is particularly clear in the summer data set, where the E-layer is particularly strong.

The predictions perform very well during daytime for the winter data set and for November. Thus the "winter anomaly" of particularly large f_oF_2 in winter seems to be correctly modelled in ICEPAC.

Predicting virtual heights is most difficult in spring and fall. Large differences between data and predictions exist for these data sets at all times of day.

Reliability.
The overall predicted reliability on the long path is too optimistic, as for the short path. The measurements show a lower reliability for disturbed conditions than for quiet conditions for the winter, spring and summer data set. The observed reliability is larger during day than at night.

The predictions overestimate the probability of propagation at night, particularly at the lowest frequencies. The predicted MUF at night is fairly correct. We believe that the main reason for the large reliabilities at night is the absence of correct absorption calculations for this sub-auroral/mid-latitude path. The path is too far south for a high occurence rate of auroral E layers which caused the night propagation on the short path. It nevertheless experiences auroral D absorption which is frequently observed in regions equatorward of the auroral oval. As a test of the absorption calculations in ICEPAC, we implemented a *non-auroral* model of the D-region (Friedrich and Torkar (64)) in a similar way to the high latitude model which will be described in the next chapter. It did not give significantly increased absorption values relative to the values predicted by ICEPAC, so we believe that an auroral absorption model is needed also on this path.

The MUF around noon is predicted fairly correctly for the winter data set, in contrast to the spring, summer and autumn data sets where the MUF is under-estimated.

Similarity coefficients.
The total similarity coefficients over all hours and frequencies for all data sets are given in Table 6.2

k(N) for time period:	Q=3	Q=6
January/February 1990, SSN=151	0,18	0,08
March/April 1990, SSN=152	0,47	0,34
June/July/August 1991, SSN=146	0,58	0,44
September/November 1990, SSN=142	0,43	0,49

Table 6.2   Similarity coefficients between measured and predicted reliability on the long path for all hours and frequencies

The coefficients for the long mid-latitude path are in general smaller than the coefficients for the short high-latitude path, which was not expected. Increasing the number of data points to be correlated (N=216 as opposed to N=96 for the short path) does not alter the general level of k since the similarity is normalized to the mean (Equation 6.4). The

similarity coefficients for each hour over all frequencies are also in general smaller than for the short path. This is the reason for the smaller total similarity coefficients. On the long path, we used a horizontal rhombic antenna instead of the horizontal dipole on the short path. The rhombic antenna has a strong main lobe with high gain at a certain azimuth and elevation angle, whereas the dipole has a rather broad lobe with small gain. Running ICEPAC, antenna models were selected from the standard antenna library, and the selected antenna may not be exactly matched to the real antenna. The January/February data set gave an example of a drastic reduction in predicted reliability caused by negative antenna gains at certain frequencies. The measurements did not show any reduction of reliability, and the corresponding similarity coefficient became small. Including more frequencies in the calculation of similarity coefficients for each hour, as we have done on the long path, makes the coefficient more sensitive to differences between actual and predicted antenna characteristics. The result is smaller similarity coefficients for each hour. Another reason for the smaller similarity coefficients for each hour at night is the lack of predicted absorption at the lowest frequencies.

However, k(24) for each frequency over all hours are in general better than for the short path, which implies a more correct prediction of diurnal variation for the mid-latitude path.

To sum up, some observations on this path indicate that the signals experience *high-latitude* characteristics:

- The reliability is larger in quiet than during disturbed conditions.

- Large absorption is observed at the lowest frequencies, particularly at night.

- There are E-layer reflections at night, which indicate auroral-E or sporadic-E, both a high-latitude phenomenon.

- On a typical mid-latitude location, the winter anomaly of absorption would give enhanced absorption during winter. This is not observed in our data. It was also not observed by the Finnish riometer chain ranging from auroral latitudes to mid-latitudes (Ranta (22)).

Other observations indicate the characteristics of a *mid-latitude* path:

- There is no clear minimum of reliability (maximum of absorption) in the morning hours as we observed on the short path.

- The prediction from ICEPAC, which classifies this path as low/mid-latitude, gives a larger similarity coefficient for each frequency (better diurnal variation) than for the short auroral path when compared with data.

The observations described in this section show that predictions at sub-auroral/mid-latitudes need to be improved in certain areas, for instance reliability at night and virtual height of reflection in spring and fall. The data collected on our long path gives however, an ambiguous picture of a mid-latitude channel obscured by high-latitude characteristics. We believe that predictions of a more typical low/mid-latitude channel would be more accurate compared to data collected on the same path, as would predictions on a typical high-latitude path. In the further chapters we therefore concentrate on suggesting improvements to high-latitude paths on the basis of observed typical characteristics of our short high-latitude path.

7   FURTHER DEVELOPMENTS OF ICEPAC

Despite the inclusion of the ICED-model in ICEPAC, there are still significant discrepancies between HF-measurements and predictions at high latitudes as pointed out in Chapter 6. We believe that some of these shortcomings can be improved by present day knowledge, and in this chapter we make some suggestions for improvement.

HF-communications over long distances rely totally on the ionospheric medium, and strong limitations are imposed on communications by the variability of the ionosphere in time and space. One example of a limitation caused by the ionosphere is the daily variation of the MUF, which is unique to communications at HF. Another example is the ionospheric absorption experienced by HF waves in the lower part of the ionosphere. The variability of the ionosphere is particularly large at high latitudes causing severe signal distortions such as multipath spread and Doppler spread, also known from other communication bands. Absorption, multipath and Doppler spread at HF has not yet been modelled properly for high latitudes, and is therefore a source of inaccuracy in prediction programmes. The ICED-model does not specify a model of the D-region where most of the ionospheric absorption occurs, so the ICED-model does not assure a proper modelling of high-latitude absorption. There is also no attempt in ICEPAC to predict the occurrence of Doppler spread and multipath. At present, only a few investigations on time and frequency dispersion of the high latitude ionosphere have been done (Wagner and Goldstein (65), Basler et al (66)), so the statistical database is very limited. New experiments in this field are now running (Davies and Cannon (67)). Our focus in this section will be on the ionospheric absorption at high latitudes. There exists a large statistical database on high latitude absorption, and this knowledge should be incorporated into future prediction programmes.

The purpose of this work is to incorporate a model of the high latitude D-region in ICEPAC and calculate absorption based on Equation 2.16. The approach can be illustrated by Figure 7.1.

As shown in the left part of the figure, a geophysical disturbance originating on the sun will cause increased geomagnetic activity. This can be measured by magnetometers and expressed by the K_p-index or the Q-index (Section 3.1). The ICED-model selects electron density profiles $N_e(h)$ for the E and F-region according to the amount of disturbance expressed by Q, and ICEPAC predicts the propagation characteristics from the selected electron densities. Comparing the ICED-model electron density profiles with electron density profiles measured by EISCAT (European Incoherent Scatter Radar) (Baron (68)), we found that they agreed very well. Also, the prediction of virtual height on the short path in Chapter 6 was quite satisfactory. Thus we conclude that the ICED-model gives a good estimate of the upper E and the F-region electron densities.
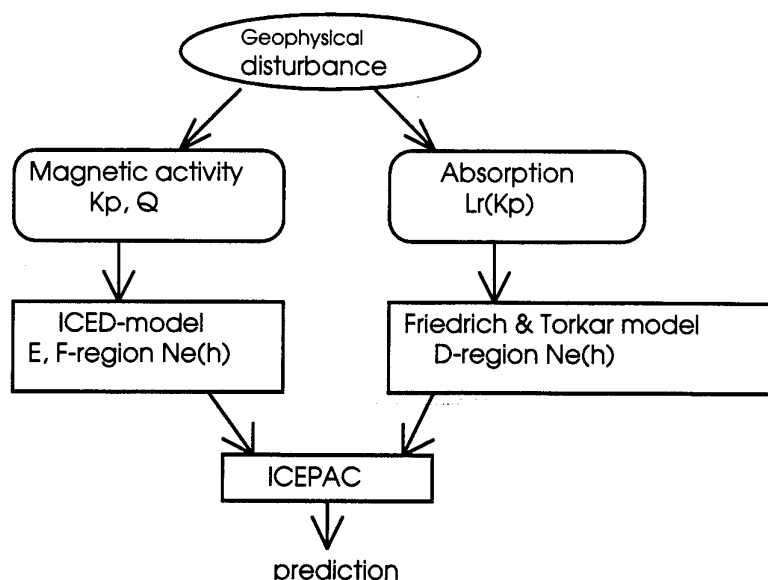
Figure 7.1   Basic principles of incorporating a D-region model in ICEPAC

We want to introduce an electron density model for the D- and lower E-region in the predictions. Enhanced absorption of radio waves is known to be associated with geophysical disturbances at high latitudes (right part of Figure 7.1). The absorption is measured by riometers and expressed as the departure in dB from the quiet-day-curve (L_r, Section 2.7). Friedrich and Torkar (7) have investigated the lower ionosphere 60-110 km using rocket measurements of electron density and simultaneous riometer measurements. They have correlated the measured electron density values at different neutral density levels (=different altitudes) with the absorption values measured at the ground, and developed models based upon an observed statistical relationship between electron density and riometer absorption (Section 7.1). The driving parameter for the statistical electron density profiles is the riometer absorption. Large absorption measured at the ground corresponds to large electron densities in the D-region. The electron density profiles are of course also dependent on time of day.

By introducing a statistical D-region model depending on the riometer absorption, combining this model in a proper way with the ICED model for the upper E- and F-region and using the correct formula in the calculation of ionospheric loss, we believe that the prediction of signal strength at high latitude can be improved. As soon as statistical electron density profiles in the D-region are included in ICEPAC with absorption as the driving parameter, the large existing database of absorption can be exploited. Or alternatively, if absorption is being measured as part of real-time channel evaluation, the real-time absorption value can be used to determine the real-time electron densities in the D-region.

7.1 A statistical model of the D-region electron density

Dr. Martin Friedrich and Dr. Klaus Torkar, Technical University of Graz, Austria have studied electron densities in the D-region for several years. As a result of this work, an empirical model of the low latitude D-region (Friedrich and Torkar (64)) has been adopted, but not yet published as the Interim Model of the D-region in the IRI (International Reference Ionosphere). This model defines the electron densities at constant neutral density levels as a function of solar zenith angle. They have also related electron density to riometer absorption at high latitudes in a systematic way. A statistical model of the high latitude D-region electron density was originally developed in 1983 (Friedrich and Torkar (7)). Since then, more data have been collected and incorporated into the model, and a new set of model coefficients have been published in Friedrich and Torkar (69). Here we will only describe the basis of the model and the features which are important for understanding how the model can be used in future prediction programmes. The high-latitude electron density model will here be referred to as the F & T-model.

The nature of ionospheric absorption was described in Chapter 2. The electron densities found in the high-latitude ionosphere are produced both by regular solar radiation that varies throughout the day, and by irregularly precipitating particles from the solar wind. The ionospheric absorption obtained by integrating through a given electron density profile using Equation 2.16 with $\mu=1$ is the *total* non-deviative ionospheric absorption L_i (integral absorption) for the raypath, regardless of whether the source of ionization is solar radiation or particle precipitation. L_i therefore comprises two types of ionospheric absorption; the "normal" absorption L_q, which a radiowave travelling through an undisturbed solar driven ionosphere will encounter, *and* the excess absorption L_r, caused by precipitating particles (disturbed particle-driven ionosphere). This can be expressed as:

$$L_i = L_r + L_q \quad [dB] \tag{7.1}$$

At high latitudes, defined here as geographic latitudes above 60°, the ionosphere is often disturbed, and at certain times of day, energetic charged particles will be the dominating source of ionospheric absorption. L_r can be measured by a riometer (Section 2.7) whereas L_q cannot directly be measured, but has to be found by integration through an electron density profile at times when $L_r = 0$.

The basic idea of the model is to use the fact that ionospheric absorption in each height interval is proportional to the electron density N_e in that slab. This can be used to relate measured D-region electron density profiles to simultaneously measured riometer absorption.

IRI predicts N_e as a function of *season, latitude, local time (solar zenith angle)* and *solar activity* in terms of the sunspot number. Solar zenith angles beyond 100° are not

addressed in the IRI, so N_e is not dependent on local time at night. In the F & T-model, a solar zenith angle between 60° and 98° can be given as input to the model to create day time profiles, whereas night time profiles are not dependent on local time. Day time conditions exist above 75 km for solar zenith angles less than 98°. The N_e-profiles were measured using a wave propagation experiment (Faraday rotation, differential absorption) on board rocket flights. The Sen and Wyller generalized magnetoionic theory was used in the calculation of N_e from the differential absorption measurements. Data from 31 dayflights and 58 night flights measured at different seasons and sunspot numbers between 0 and 260 are used in the present model. The rockets were flown from from Andøya, Norway (69°N) and Esrange, Sweden (67°N). In the latest model an attempt has been made to remove seasonal and latitudinal dependence of the model by fitting the data at constant neutral density levels that was found in CIRA (20), instead of at constant heights as in the previous model. Friedrich and Torkar (69) tested the dependence of the measured N_e-values on the sunspot number. No obvious trend was found.

Most of the riometer measurements were made at 27.6 MHz, data obtained at other frequencies were scaled by the inverse frequency squared ratio. The riometers at the rocket ranges were used most of the time.

Night-time N_e-profiles are different from the daytime profiles because: 1) There is no ion/electron production by direct solar radiation, 2) The negative ion density is larger at night caused by a lack of photo detachment of electrons from negative ions, 3) The lack of O at night-time allows the formation of positive water cluster ions which again increases the electron loss rate. Because of these differences in the nature of the N_e-profiles, the collected data were grouped into day and night-time profiles with a limiting solar zenith angle of 98°, and separate day and night-time models were developed.

The night model.

Since there is no electron production by direct solar radiation at night, the absorption produced by the quiet ionosphere L_q is assumed to be a constant. It is also assumed that N_e at any one height is proportional to the total absorption L_i at the time of the measurement (proportionality factors depending on the height). In order to obtain a first estimate of L_q, an initial N_e-profile was selected recorded at a time when $L_r = 0$. The total ionospheric absorption was calculated using Equation 2.16 with properly chosen collision frequencies from CIRA. The calculated value L_i should in this case be equal to L_q. This was taken as the initial value of L_q. At constant neutral density ρ, the available N_e-values from all the rocket flights were plotted against L_i ($= L_r + L_q$) in a scatter plot. Regression lines were drawn at each specific neutral density level between the highest and the lowest measurements of riometer absorption, and coefficients $A_n(\rho)$ and $B_n(\rho)$ determined:

$$N_e(\rho) = A_n(\rho) + B_n(\rho) \cdot L_i \tag{7.2}$$

In this way, mean statistical N_e-profiles for any given L_r, including $L_r=0$ were established. The statistical profile for $L_r=0$ was used to calculate a new statistical L_q using again Equation 2.16. The final statistical profiles at night are shown in Figure 7.2. The curves are dashed or terminated where the measured riometer values are outside the standard deviation of L_r, but inside the highest and lowest measured value.

The day model.

Solar electromagnetic radiation produces a diurnal variability of the electron densities in the quiet ionosphere. The absorption of the quiet, daytime ionosphere therefore varies with the solar zenith angle. L_q is expressed as $L_q = L_0 \cdot (1/Ch(\chi))^n$ where χ is the solar zenith angle and $Ch(\chi)$ is the Chapman function. The constants L_0 and n can be determined by selecting two measured N_e-profiles with different χ-values, finding the integral absorptions for both profiles using Equation 2.16, taking $L_q = L_i - L_r$, and solving the two equations for L_0 and n. Basically, the same procedure used for the night profiles was applied to find a statistical model of the daytime electron densities as a function of measured riometer absorption:

$$N_e(\rho) = A_d(\rho) + B_d(\rho) \cdot L_i = A_d(\rho) + B_d(\rho) \cdot \left[L_0 \left(\frac{1}{Ch\chi} \right)^n + L_r \right] \qquad (7.3)$$

The constants were determined to be $n=0.4$ and $L_0=0.8$ dB. The statistical daytime profiles are shown in Figure 7.3.

The physical relevance of the models was tested against models of electron production and loss processes and only minor discrepancies were found (Friedrich and Torkar (7)).

This work has established a mean, high-latitude electron density model of the D-region for day and night. The profiles are believed to be representative for auroral disturbances at high latitudes. Riometer absorption between 0 and 2.5 dB occurs more than 90% of the time at auroral latitudes, and consequently, N_e-profiles for these conditions will also cover the situation for 90% of all cases.
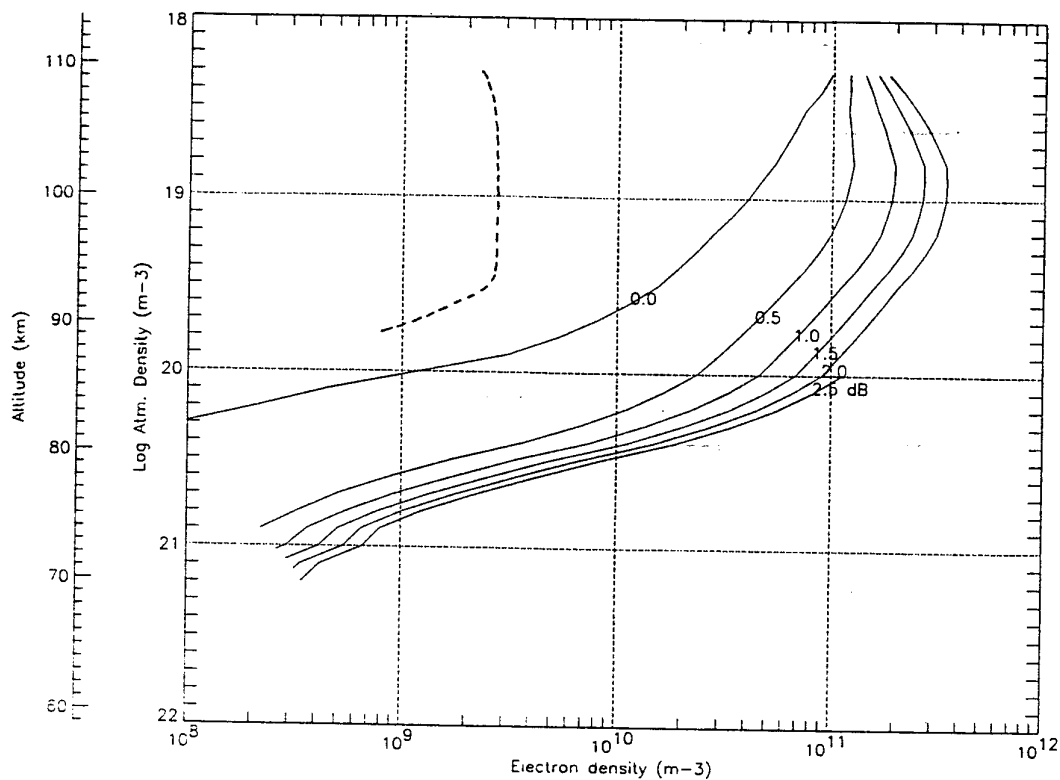
Figure 7.2   F & T-model electron density profiles at night (Friedrich and Torkar (69)). Empirical, non-auroral model indicated as dotted line
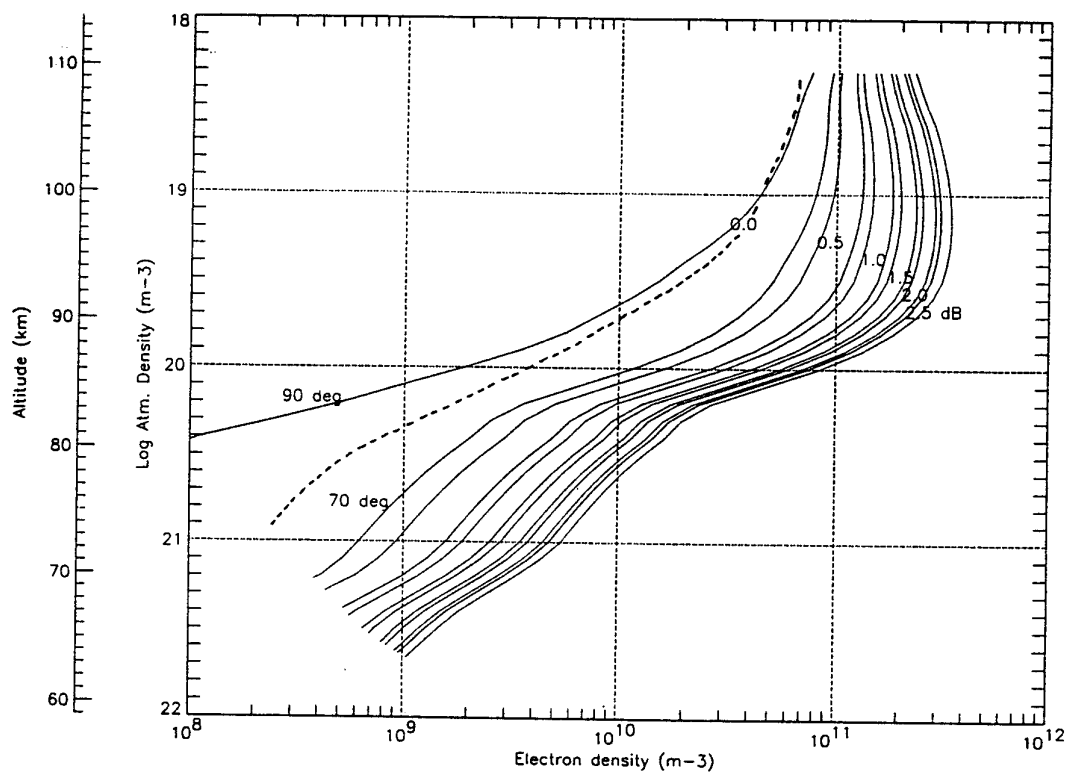
Figure 7.3   F & T-model electron density profiles at day for different solar zenith angles(Friedrich and Torkar(69)). Dotted line: Non-auroral model for χ=70°

7.2 Correlation between geomagnetic activity (K_p) and riometer absorption (L_r)

The ICED-model electron density profile in the height region 110-1000 km must now be combined with a statistical D-region profile in the region 60-110 km. The ICED-model selects an electron density profile determined by time of day, sunspot number and the geomagnetic index, Q. The D-region profiles in Friedrich and Torkar (69) are governed by time of day and measured riometer absorption L_r. Geomagnetic activity and ionospheric absorption are both signs of a disturbed ionosphere, but what is the correlation between them? Data have shown (George (24)) that there exists a geomagnetic control of the absorption. In view of the current, ordinary use of prediction programmes we have chosen to ask the question: Given a predicted sunspot number and an expected geomagnetic activity level (fixed Q), what will the absorption L_r be (variable L_r)? In the following we compare the two indices Q and K_p in order to combine D and E/F-profiles in a proper way.

The availability of K_p is better than for Q, so here we shall use K_p-data. K_p-data is found in IUGG (70) for the month of March 1988. L_r-data is taken from Stauning (71) for the same month. 31 days are compared, and to reduce the effect of the solar zenith angle dependence, the data are plotted separately at intervals of three hours corresponding to the K_p-measurement intervals. Seasonal variations are not considered since data from one month only was used. The riometer measurements are taken at 32 MHz, and data taken every minute are averaged over a three hour period. The correlation between K_p and L_r is displayed in Figure 7.4 for the eight different time intervals (UT).

A linear relationship can be seen on most of the plots, and a least-square first order polynomial fit is made to the scatter plots. The variance of the fit varied between 0.10 and 0.44 for the eight different plots. The steepest linear relationship is found in the morning hours, from 3 UT to 11 UT. For these hours a small increase in the K_p-index corresponds to a relatively large increase in the measured L_r. In the afternoon and evening hours, a small increase in K_p corresponds only to a small increase in L_r. This observation expresses the well known phenomenon of morning absorption at high latitudes. The absorption is high in the morning hours, and it is not necessarily accompanied by a geomagnetic disturbance, whereas in the evening, it takes a large geomagnetic disturbance to produce large absorption. At noon, all the measured absorption values for this month were negative, which means that interference was recorded. From the fitted curves one can read out the probable K_p-index for a given absorption. For example an absorption of 0.1 dB at 0-2 hours corresponds to a K_p-index of 1 and a Q-value of 3, using the relationship between K_p and Q from Section 3.1.
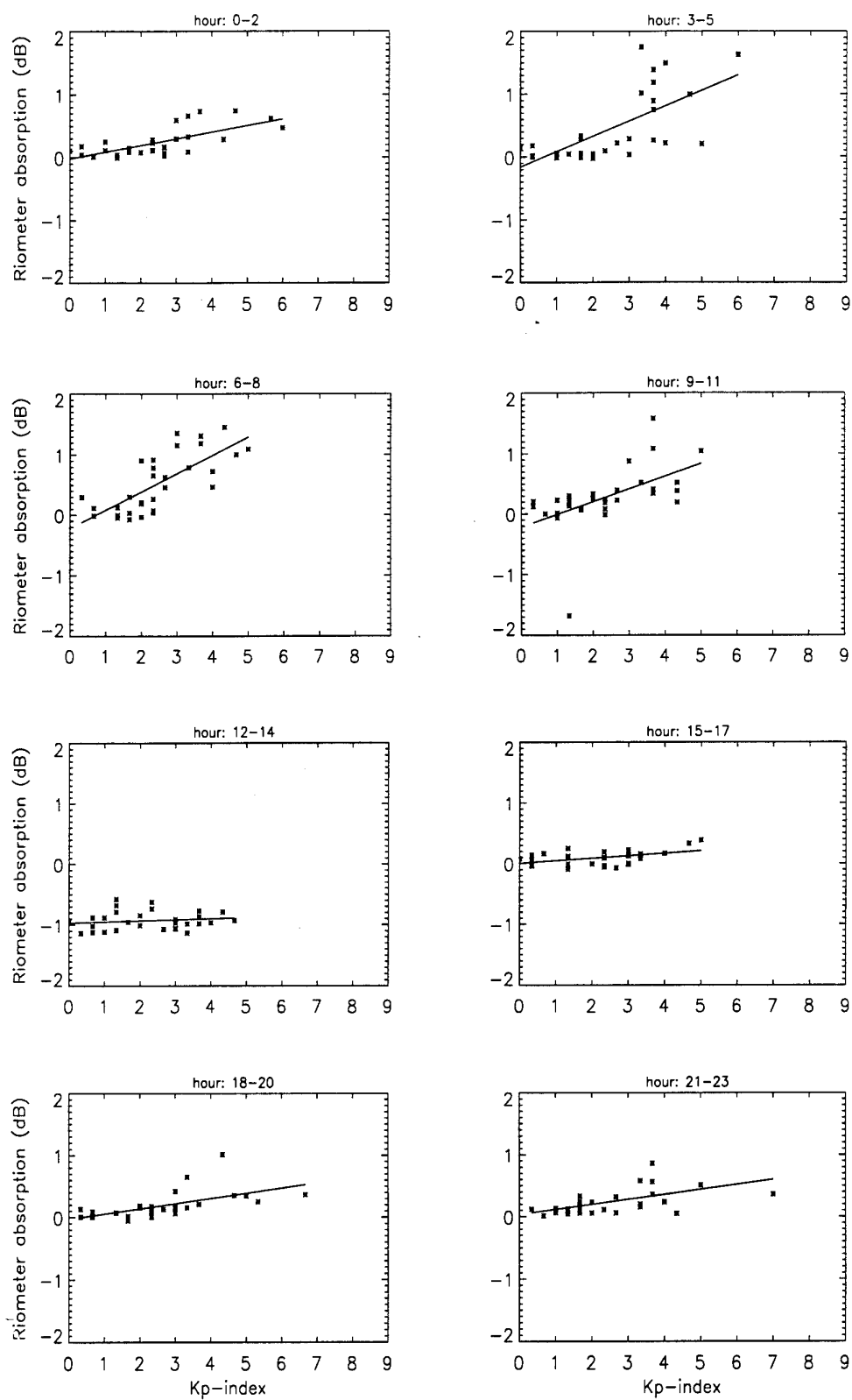
Figure 7.4   Correlation between K_p and L_r for March 1988

Absorption roughly depends on frequency as $1/f^2$, so absorption measurements at different frequencies must be scaled in order to be compared. In the work by Friedrich and Torkar (69) riometer measurements were taken at the frequency 27.6 MHz. Absorption measured on this frequency is the basis for selecting the appropriate electron density profile in the D-region. We must therefore scale the absorption measured at 32 MHz according to the formula:

$$L_{27.6} = L_{32} \cdot \left(\frac{32 + f_H \cdot \sin I}{27.6 + f_H \cdot \sin I}\right)^2 \qquad (7.4)$$

where f_H is the gyro frequency and I is the inclination or magnetic dip which is about 78° in the area where the measurements took place. We have chosen geomagnetic activity levels of Q=0, Q=3, Q=6 and Q=8. The following table shows the diurnal relationship between geomagnetic activiy level Q, and the absorption L_r in dB at 27.6 MHz for the month of March 1988:

Hour (UT)

Q-value	0-2	3-5	6-8	9-11	12-14	15-17	18-20	21-23
0.0	0.0	0.0	0.0	0.0	0.0	0.0	0.0	0.0
3.0	0.13	0.13	0.13	0.0	0.07?	0.13	0.13	0.13
6.0	0.53	1.06	1.33	0.80	0.54?	0.27	0.40	0.53
8.0	0.80	1.72	2.12?	1.33?	0.80?	0.27?	0.66	0.66

*Table 7.1   Riometer absorption (dB) at 27.6 MHz measured at Lavangsdalen
(geographic position 69.40 N, 19.30 E) as a function of hour and
geomagnetic index for March 1988*

For the hours 12-14 UT, when the absorption measurements failed, we have chosen to interpolate linearly between the values measured at 9-11 UT and the values measured at 15-17 UT, in order to make the diurnal plots continuous. We have put question marks on the absorption values for Q=8, hours 6-17 because these values were found by extrapolation of the calculated regression line. For a geomagnetic disturbance larger than Q=3.0, ionospheric absorption is weak during the day, increases in the evening and night to a maximum for the hours 6-8. The values shown in Table 7.1 will be used in the coming absorption calculations.

7.3   Calculations of non-deviative ionospheric loss

The non-deviative ionospheric absorption of the ordinary wave was given in Section 2.5 as:

$$L_i = 4.6 \cdot 10^{-2} \cdot \int_s \frac{N_e \cdot \nu}{(\omega + \omega_L)^2 + \nu^2} ds \quad [dB] \tag{7.5}$$

We will be using this formula for the calculation of ionospheric loss, and these calculations will be referred to as *absorption calculations*. On the computer, and for an oblique ionospheric path, Equation (7.5) takes the form:

$$L_i = 4.6 \cdot 10^{-2} \cdot \frac{1}{\cos\varphi} \cdot 2 \cdot \sum_{h_1}^{h_2} \frac{N_e(h) \cdot \nu(h)}{4\pi^2(f + f_L)^2 + \nu(h)^2} \cdot 1 \quad [dB] \tag{7.6}$$

φ is the angle of incidence of the radio wave on the ionosphere, the factor 2 accounts for the radio wave traversing the ionosphere twice (upleg/downleg), h_1-h_2 is the altitude range for the summation. We have chosen the resolution of the vertical profiles to be 1 km. This formula assumes that the absorption is the same on upleg and downleg, and thereby that the actual path is within a horizontally uniform ionosphere.

Absorption has been calculated for the month of March 1989 for the particular path Andøya-Alta ($\approx$ 70°N and 285 km) described in Chapter 5. A one-hop path is assumed for this short path, which is consistent with predictions. At this high latitude, the inclination of the magnetic field is large, and $f_L \approx f_H = 1.4$ MHz is rounded off to 1.4 MHz. The factor cos φ is found from geometrical calculations, using the virtual height of reflection predicted by ICEPAC (Figure 6.5 in Section 6.2.2). The interval of integration is determined by the height interval at which there exists a D-region statistical electron density model; for March, 67 km - 116 km for the night model and 60 km - 119 km for the day model. If the predicted virtual height of reflection is below the upper altitude of the statistical model, only integration up to the height of reflection will take place.

The vertical profile of the collision frequency is determined in the following way: Pressure values every 5 km for the altitude range 20-120 km for March at 70°N, are found in CIRA (20). Logarithmic interpolation gives the pressure at every km of height. The mean collision frequency is then calculated using Equation (2.19).

The F & T-model electron density profile described in Section 7.1 is specified as a function of neutral density. In order to use Equation (7.6), the relationship of N_e with height has to be established. The pressure (p) and temperature (T) values in the height range 20 -120 km are first found in CIRA. Neutral density is then calculated from the ideal gas equation; n=p/kT, where k is Boltzmans constant. We compare the calculated neutral density values with the logarithmic neutral density values of the F & T-model profiles, and find A and B coefficients by linear interpolation between the coefficients of

the model. In this way, A and B coefficients for every km of height are established. Note that this height profile is unique to the month of March at 70°N. To calculate the "quiet" absorption L_q in day time, we use the solar zenith angle for Tromsø (midpoint of the actual path). The transition from night to day is at 3 UT and from day to night at 19 UT.

The result of the absorption calculations is shown in Figure 7.5 as a function of time of day and frequency for four levels of geomagnetic disturbance. The frequency range has been chosen from 3.0 MHz to 19.0 MHz in steps of 0.5 MHz. It is important to note that frequencies above the MUF are not likely to propagate. The MUF's of this actual path are predicted to be between 3.5 MHz and 7.7 MHz depending on time of day and geomagnetic activity. Note that the scaling of the loss-axis is different for the four figures, but a fixed gray scale has been used. The riometer absorption that determines the model electron density profile, is given for each hour in Table 7.1.

For Q=0 (L_r=0.0), the following can be observed:

- The loss varies smoothly with a maximum ionospheric absorption of 28 dB at 11 UT, and a night absorption of 8 dB. The virtual height of reflection is in most cases above the range of integration, so the only influence of the reflection height is to modify the angle of incidence of the raypath on the ionosphere. A large angle of incidence (E-layer) may cause an additional loss of up to 15 dB compared to F-layer modes on this particular path. One cause of the maximum absorption around noon is the E-layer reflections at the lowest frequencies. The minimum solar zenith angle of 71.6° at 11 UT (12 local time) is another reason for the maximum ionospheric absorption.

- The losses show distinct minima at the transitions between day and night. These minima are consequences of discontinuities (deficiencies) in the F&T-model.

- At the MUF the ionospheric loss attains a value between 5 and 10 dB.

For Q=3 (L_r 0.0-0.13 dB), the following can be observed:

- The ionospheric loss has increased about 10 dB for both night and day.

- There is a sudden reduction of loss for hours 9-11. Table 7.1 gives a minimum riometer absorption of 0.0 dB for these hours which is reflected in the F & T-model loss calculation on this particular path.

- At night, an E-layer reflection for hour 0, frequency 3.0 MHz (Figure 6.5, Section 6.2.2) causes an increased angle of incidence on the ionosphere and therefore increased loss compared to the following hours.

- This figure of F & T-absorption loss shows an intermediate state between Q=0 and Q=6, where an absorption maximum in the morning hours (auroral absorption) is

taking over from an absorption maximum around noon (solar zenith angle dependent absorption).

For Q=6 (L_r 0.27-1.33 dB), the following can be observed:

- Maximum absorption occurs for the hours 6-11 and a minimum for the hours 15-17 UT. A second, smaller maximum occurs around midnight.

- The maximum of absorption is not centered around local noon (11 UT), but shifted towards the morning. No clear solar zenith angle dependence is seen.

- The change between night and daytime electron density profiles as observed for Q<6 is no longer evident.

- The ionospheric absorption for Q=6 attain values over a large range, from 20-150 dB. The L_r-value selected from Table 7.1 is the most important factor that determines the absorption for each hour and frequency, but also virtual height of reflection influences the absorption. For hour 5, frequency 3.0 MHz, a predicted F_2-layer reflection (Figure 6.5 Section 6.2.2) causes an absorption minimum, and for hour 8, frequency 3.0 MHz, a predicted E-layer reflection causes an absorption maximum.

For Q=8 (L_r 0.27-2.12 dB), the following can be observed (it must be noted that for the hours 6 to 17 the L_r data are found by extrapolation and are therefore uncertain):

- Maximum absorption is more than 200 dB and occurs for the same hours as for Q=6.

- The increase of absorption at night compared to Q=6 is smaller, consistent with riometer absorption in Table 7.1.

- For the hours 0-3 UT, ICEPAC predicts a dense E-layer causing reflections below 100 km for f=3 MHz. The F & T-model calculations integrates only up to this low altitude causing a small total loss.

Model loss Q=0

Model loss Q=3

Model loss Q=6

Model loss Q=8
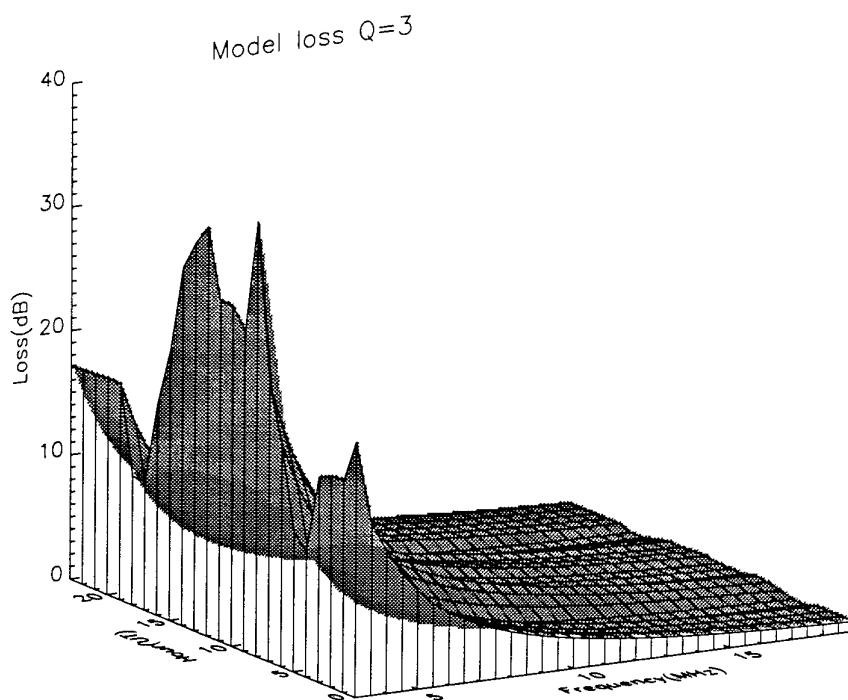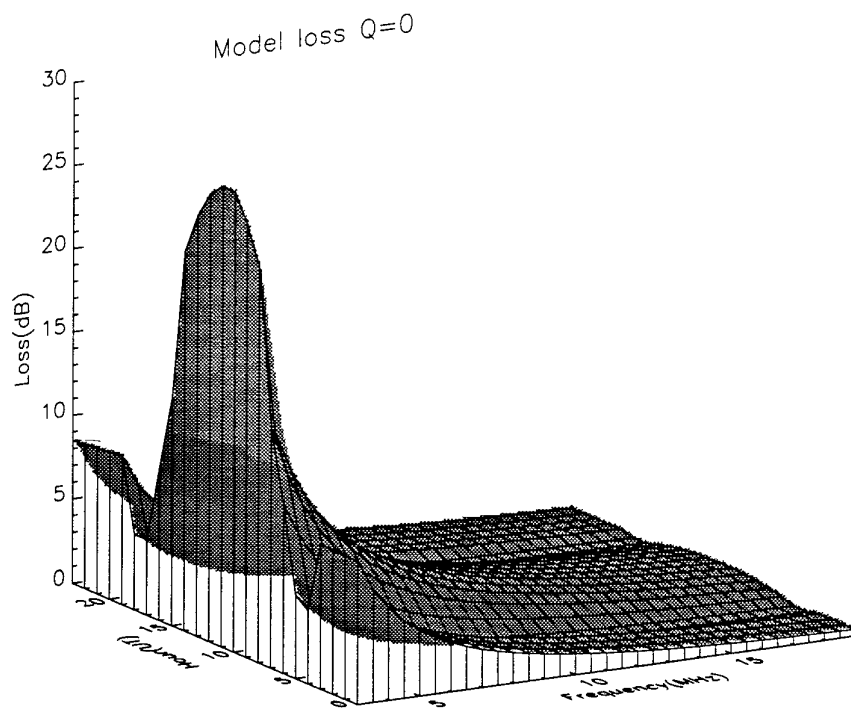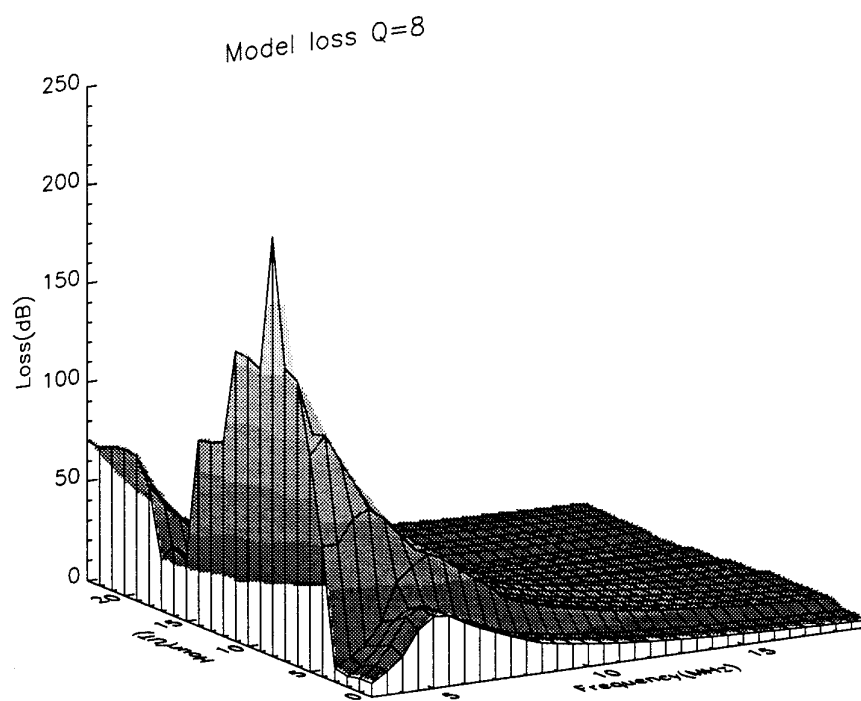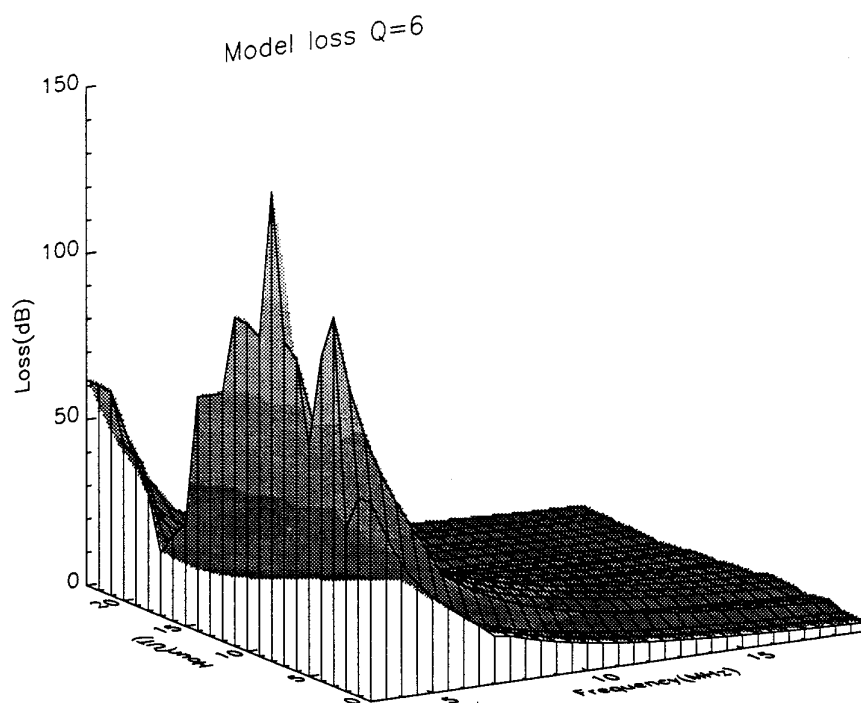
Figure 7.5   Absorption calculations using the F&T-model for the one-hop path
Andøya-Alta (285km)

7.4 Predicted ionospheric loss

The different types of losses predicted by ICEPAC was described in Section 4.3. The absorption calculations in the preceding section include non-deviative ionospheric loss only. The predicted losses that best correspond to the absorption calculations would be the sum L_i of ionospheric absorption L_{n-d}, the residual auroral loss adjustment L_{aur}, and the loss term called E-layer corrections and deviative losses for high-angle modes, L_{cor}.

$$L_i = L_{n-d} + L_{aur} + L_{cor} \qquad (7.7)$$

The sum of these components will include the effect of deviative absorption for both high and low angle modes, and thus is not directly comparable with the F & T absorption calculations. Deviative absorption is included in the ionospheric absorption for low angle modes, and is therefore impossible to exclude from our comparisons. Nevertheless, theory shows that deviative absorption is very small compared to non-deviative absorption. We therefore compare the absorption calculations with the sum L_i of the three predicted loss terms, keeping in mind that the predicted loss contains deviative losses, and the absorption calculations does not.

Predicted L_{aur} for our test path is shown in Figure 7.6 for March 1988. It is defined as a quantity independent of frequency, but it varies with time of day. The dependence on geomagnetic activity is almost negligible. There is a maximum auroral loss of 15 dB during the hours 6-8, and a minimum during the hours 12-14. Again in the hours before midnight, a second, but smaller maximum occurs. The form of this curve agrees quite well with the described high latitude variation of absorption, Section 2.8.3, but it is remarkable that L_{aur} does not depend on geomagnetic activity. The L_{aur} curves for autumn are almost identical. Predicted L_{aur} for summer and winter are in general lower with the second maximum of absorption occuring earlier in the evening at 18-20 UT. The summer and winter profiles agree less with the high-latitude absorption described in Section 2.8.3.
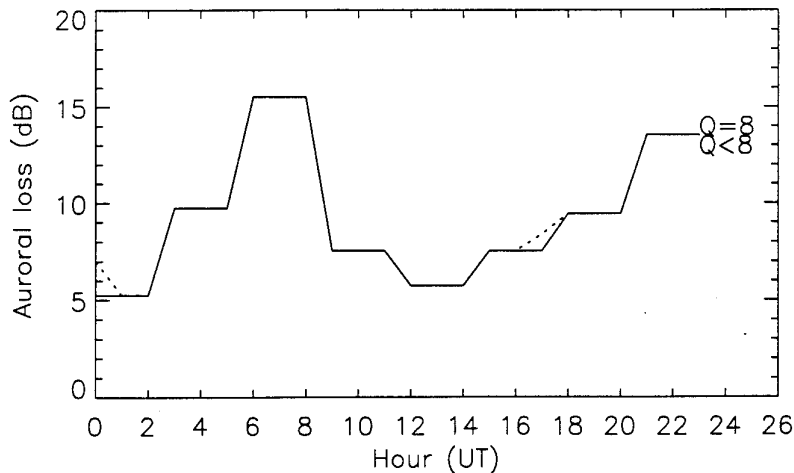
Figure 7.6   Auroral loss adjustment to median signal level, L_{aur}, as a function of
time of day and geomagnetic activity index Q. Q<8 continous line, Q=8
dotted line

The predicted ionospheric loss for Q=0, 3, 6 and 8 is plotted in Figure 7.7 in a similar diagram as for the absorption calculations. The losses are predicted for the most reliable mode. We have plotted predicted losses only up to 8.5 MHz since the MUF is well below 8.5 MHz at all times.

For Q=0 and Q=3 we note the following:

* The predicted losses for Q=0 and Q=3 are equal to within 1 dB. The range of predicted losses is from 10 to 40 dB.

* The contribution to the total predicted ionospheric loss L_i from the non-deviative ionospheric loss L_{n-d} and the auroral loss L_{aur} varies throughout the day. For the hours 9-15 L_{n-d} contributes the most with more than 10 dB. L_{aur} for these hours is less than 8 dB. In particular, L_{n-d} is large for f<4 MHz. At other hours L_{aur} is the largest contributor to the predicted loss, and its diurnal variation shown in Figure 7.6 can be recognized in the figure for Q=0 and Q=3.

* The correction loss term L_{cor} is equal to or close to zero for most of the hours and frequencies. An exception is hour 8 and frequency 6.5 MHz, where the L_{cor} is 12 dB. The reason for this large correction loss is that a high-angle mode is the most reliable mode, and this mode experiences large deviative absorption. The loss peak should therefore be considered as a result of deviative absorption, which is not included in the absorption calculations.

Predicted loss Q=0

Predicted loss Q=3

Predicted loss Q=6

Predicted loss Q=8
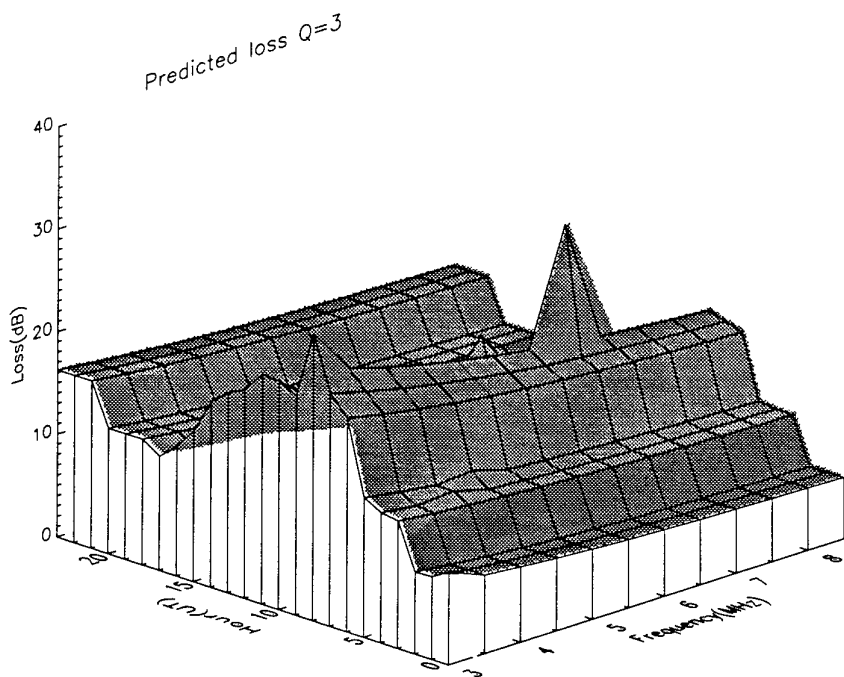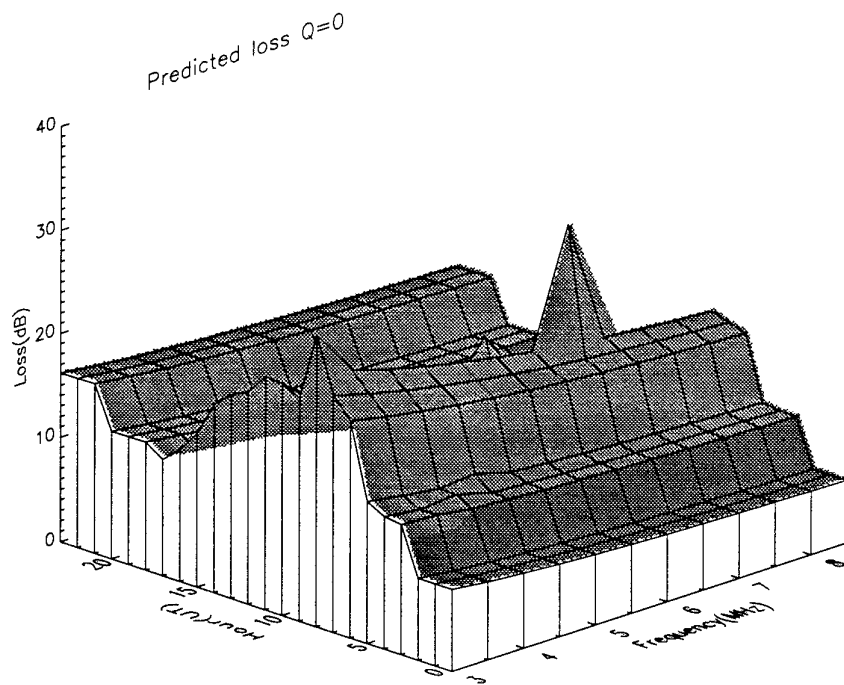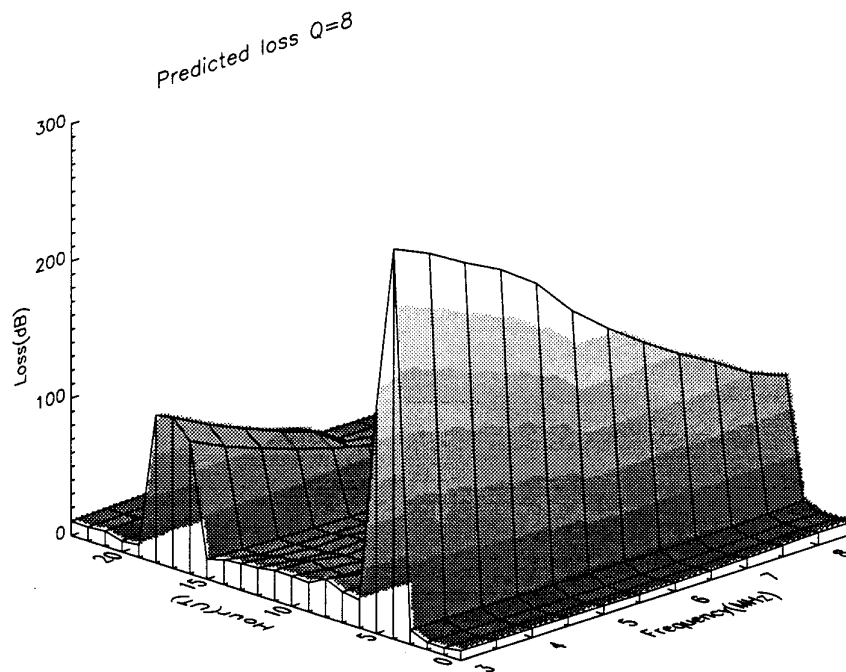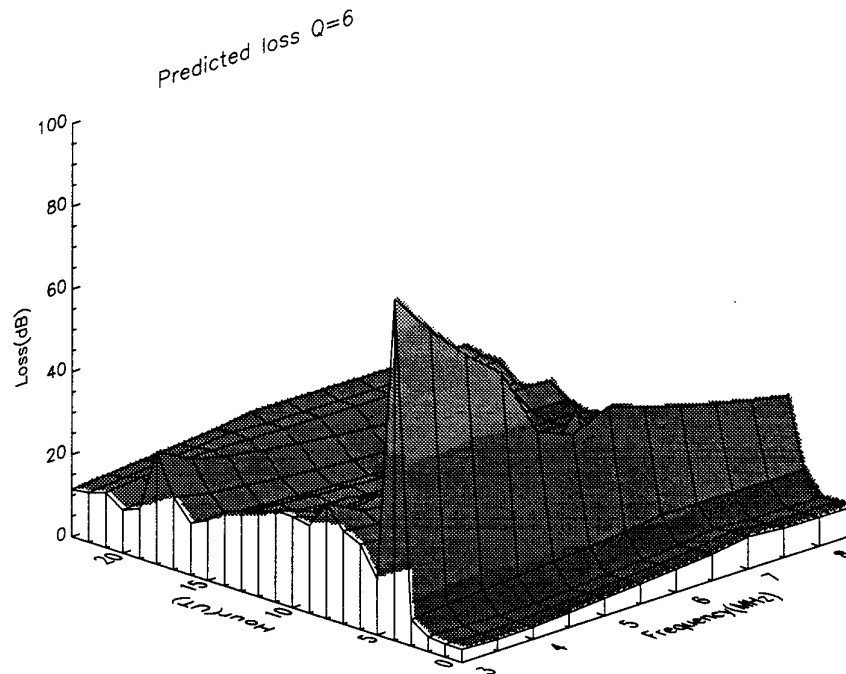
*Figure 7.7   Ionospheric loss predicted by ICEPAC for geomagnetic activity
levels of Q=0, 3, 6 and 8 for the path Andøya-Alta (285 km)*

For Q=6 and Q=8, the following has been observed:

- Two dominating absorption peaks of up to 300 dB occurs at 4 UT and 18 UT for all frequencies. For Q=8 they also appears at hours 5, 16 and 17 UT. For these hours a dense auroral E-layer is predicted (Figure 7.12, Section 7.6). However, the same dense auroral E-layer is also predicted for adjacent hours, and is thus not the cause of the extreme absorption predicted at these particular hours. It was pointed out in Thrane et al (4) that incorporating the high-latitude ICED-model in ICEPAC required a revision of the absorption equation (Equation 4.4) used in ICEPAC. ITS has attempted to revise the absorption equation, but with little success, as observed in Figure 7.7: The absorption index (Equation 4.4) gives excessive absorption when the midpoint of the path is flagged as an auroral location with a large auroral E-layer. To limit this overestimated loss, ICEPAC sets the absorption index to a constant low value for auroral sunrise/sunset and night locations, but leaves the excessive absorption for auroral day locations. The hours showing the absorption peaks are classified as auroral daytime locations.

- Ignoring the absorption peaks, the general level of ionospheric absorption has *not* changed, but is similar to Q=3 to within 1 dB for all frequencies for the hours 5-16 and 19-3. During the hours around noon, the solar zenith angle variation of absorption is visible for Q=6. At 8 UT and 3 MHz L_{aur} is visible as a local, small maximum.

- Considering the above observations, the prediction of ionospheric absorption at high latitudes has some arbitrary elements that should be revised.

7.5   Comparisons of absorption calculations and predictions

The absorption calculations include ionospheric *non-deviative* absorption only, whereas the losses predicted by ICEPAC also contain *deviative* absorption. This should imply that if the predicted absorption was otherwise correct and deviative absorption is *not* negligible, the predictions would generally be larger than the absorption calculations. This is however not so. The difference between the absorption calculations and predicted loss as described in earlier sections, is plotted in Figure 7.8 for the four different values of Q. The rms-values of the differences (including all calculated points), or the "error" if the absorption calculations are assumed to be correct, are:

Q	0	3	6	8
rms of difference	8.3 dB	6.5 dB	24.9 dB	47.7 dB

Table 7.2   RMS of difference between absorption calculations and predictions

- For Q=0, the predicted loss is up to 10 dB larger than the absorption calculation.

- For Q=3, the rms-value of the difference is small and the plotted surface in Figure 7.8 is close to zero. This means that even for Q=3 either the non-deviative part of the predicted absorption is estimated too low, or the deviative absorption is negligible.

- For larger geomagnetic activities the absorption calculations are far above the predictions and indicate that the predictions grossly underestimates the ionospheric absorption at high latitudes.

For low geomagnetic activity, the diurnal variation of the difference is not very pronounced. The F & T-model absorption calculations for Q=0 and Q=3 yield minima around 4 UT and 17 UT. This feature is a concequence of an inadequacy in the F & T-model and is not a physical phenomenon. For high geomagnetic activity the predicted losses are generally much too small at all times of day and for all frequencies. The difference maximizes in the morning with a peak at 8 UT of up to 200 dB for Q=8. We have chosen to put a lower limit on the absorption difference at -30 dB, which excludes the effects of the large predicted absorption peaks around 4 UT and 17 UT (Figure 7.7). They have no physical relevance and is only due to the implementation of certain equations as pointed out in Section 4.3.1 and Thrane et al (4). We have chosen to ignore this obvious error by defining a lower limit of -30 dB, and rather emphasize the general trends.

The "shape" of the absorption calculations and the predictions merits some comments: The F & T-model absorption loss for Q=0 is governed by solar electromagnetic radiation, and a maximum occurs around noon. For large Q, the absorption is controlled by precipitating particles, and the maximum absorption occurs in the morning hours as shown in the absorption calculations. A second maximum occurs around midnight, and a minimum from 15 to 18 UT. This correlates very well with riometer observations described in Section 2.8.3. By using a model of the D-region which is controlled by measured riometer absorption, the diurnal variation of ionospheric absorption caused by particle precipitation is incorporated into loss calculations on a specific path.

Note that in the predictions, the general level of ionospheric absorption does not depend upon geomagnetic activity. This is certainly an error that should be corrected. The auroral loss adjustment factor L_{aur} displayed in Figure 7.6 is also independent of Q. Nevertheless, this factor gives a correct diurnal trend of high latitude absorption for this particular month.
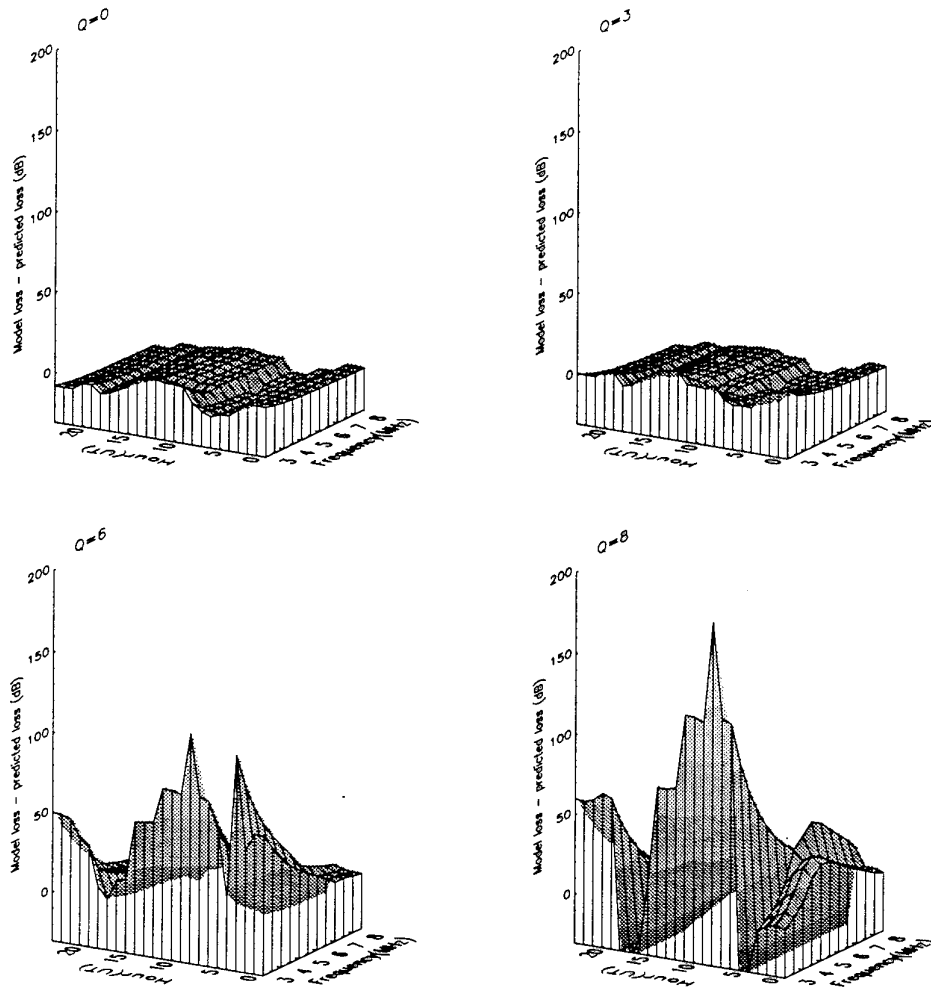
Figure 7.8   Difference between absorption calculations and predicted ionospheric
loss (model loss - predicted loss) for March 1988

An error in the predicted losses of up to 200 dB for high geomagnetic activity is fatal for reliability predictions. High geomagnetic activity often occurs at high latitudes, and it is a fact that predictions of reliability in these regions fail more often than at low and mid-latitudes. The empirical data that are included in the predictions are from low and mid-latitudes only, and these data have been used to derive the standard formula for ionospheric absorption. Therefore, the particle-controlled diurnal variations of absorption experienced at high latitudes are not properly incorporated in the predictions. To include both the diurnal variation *and* the effect of geomagnetic activity on ionospheric absorption, we propose to use the D-region model described here in future prediction programmes. The improvement achieved by doing so, will be explored in later sections.

7.6   Electron density profiles

How do the electron density profiles used in ICEPAC compare with the F & T-model of the D-region as introduced here? The ICED model used in ICEPAC was described in Section 4.5. The electron density profiles specified by the ICED model are defined every 10 km of height from 90 km up to 500 km, and every 50 km from 500 km up to 1000 km. ICEPAC has extended the profiles down to 70 km by fixing N_e at 70 km at $1.24 \cdot 10^9$ m^{-3} and interpolating the electron density linearly between 70 and 90 km. The F & T-model has a resolution of 1 km and covers the altitude range 67-116 km for night- time and 60-119 km for daytime for the month of March. Both the F & T and the ICED-profiles are plotted in Figures 7.9-7.12 for different hours and Q-values. Three successive hourly ICED profiles have been plotted in the same plot, whereas the F & T-model profile has been plotted for the middle of the time interval only. Note that the ICED-profiles might change character from one hour to the next according to the position of the auroral oval. Table 7.1 has been used in the derivation of the F & T-model profiles.

For Q=0, all the ICED profiles are classified by the model as mid-latitude profiles. All layers (E, F_1, F_2) are Chapman layers. For the hours around noon all three layers are present, whereas for sunrise/sunset and night-time conditions, only F_2 and E layers are present.

During the hours 6-17 UT the correspondence between the overlapping part of the F & T-model and the ICED-model is fairly good, with a tendency of the ICED densities being largest. During the remaining hours (night) the ICED electron densities are larger than the F & T-model below 90 km and up to an order of magnitude smaller above 90 km.

Q=0:
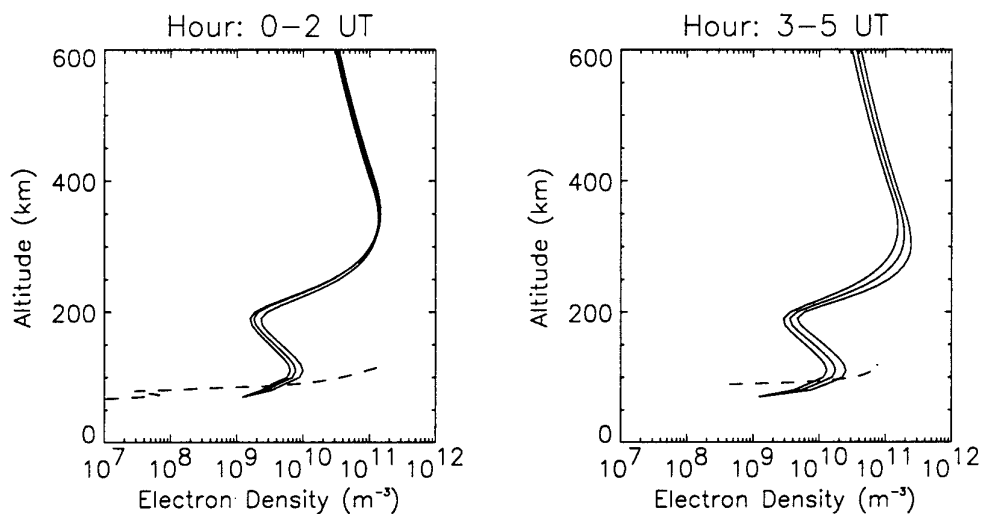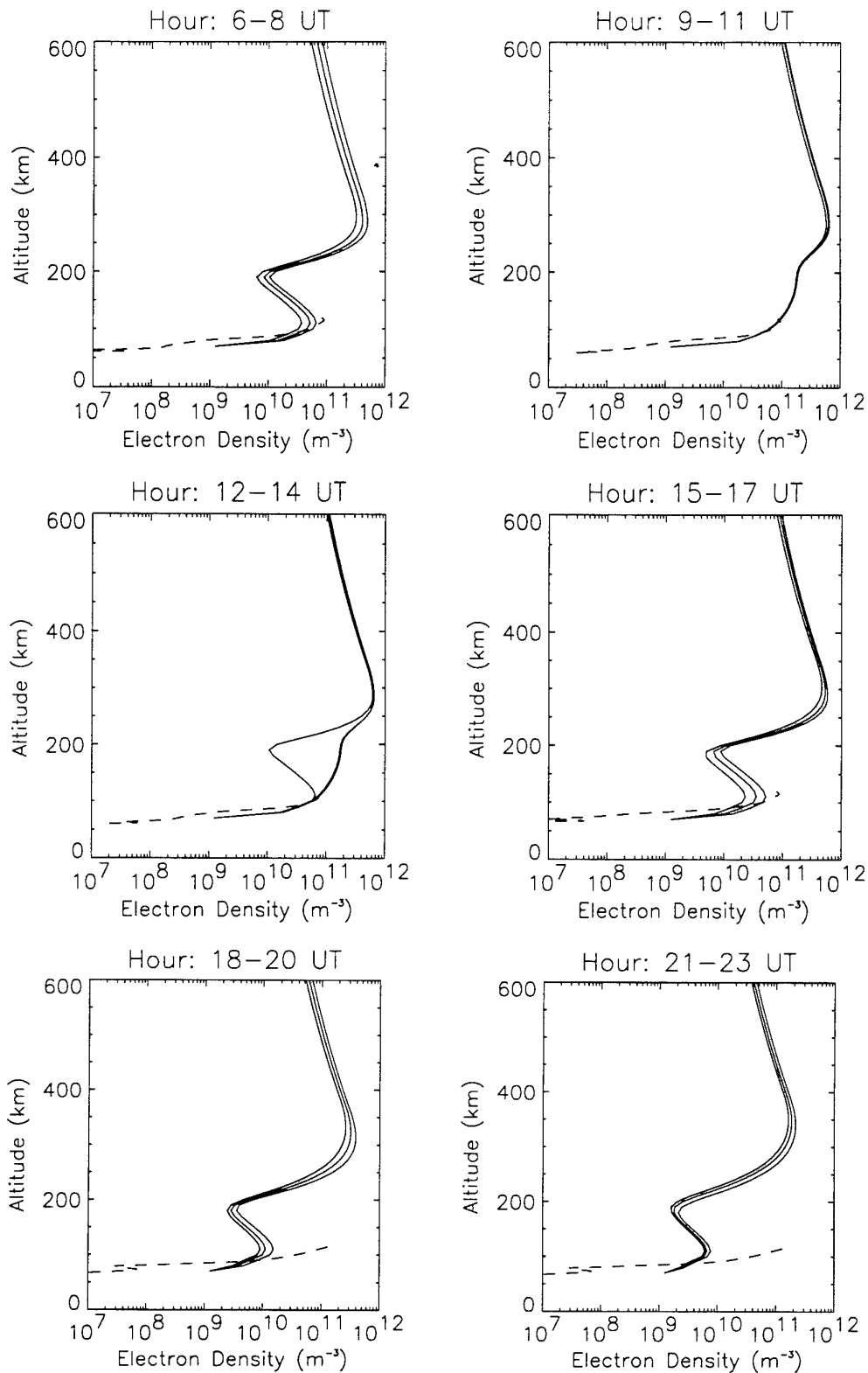
Figur 7.9 ICED-model profiles (continous lines) and F & T-model profiles (dashed
lines) for the midpoint of the path Andøya-Alta for the month of March,
Q=0. Three consecutive hours are shown for the ICED-model, whereas
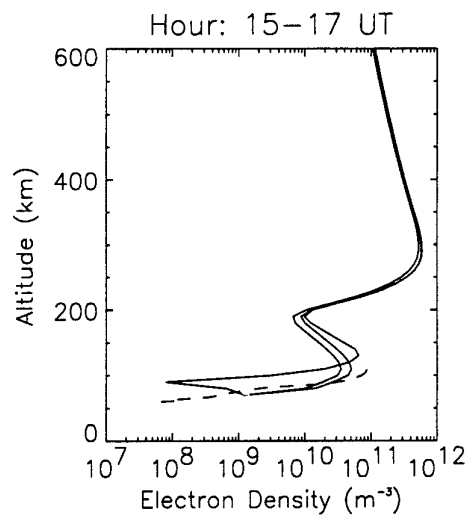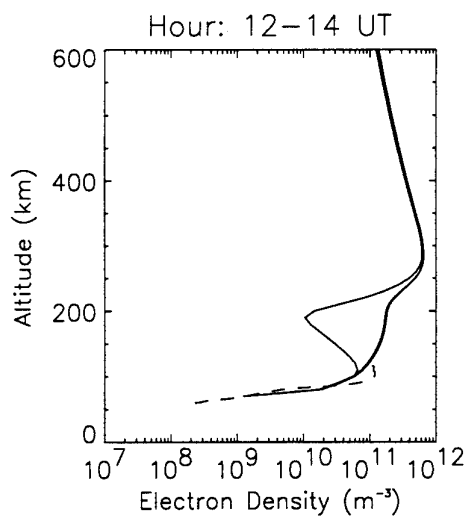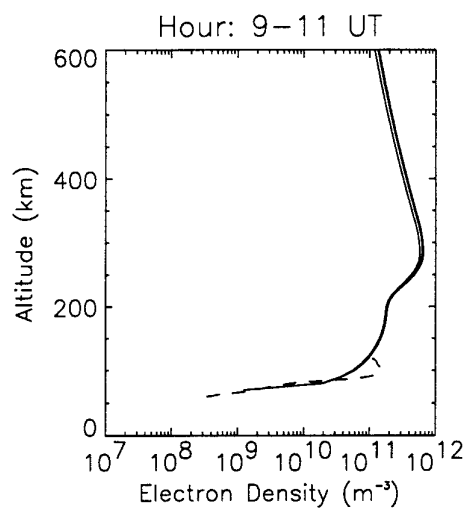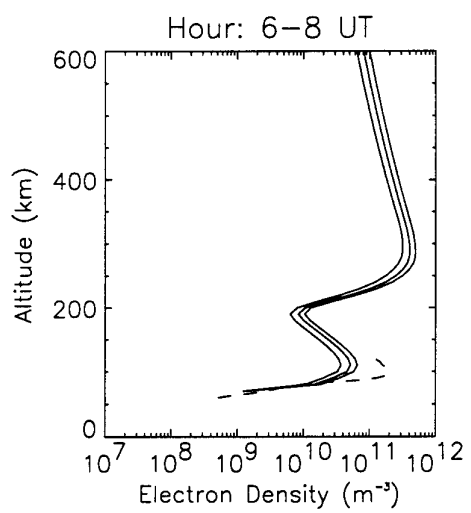the F & T-model is shown for the mid-hour only

Q=3:

Hour: 0-2 UT

Hour: 3-5 UT

Hour: 6-8 UT

Hour: 9-11 UT

Hour: 12-14 UT

Hour: 15-17 UT
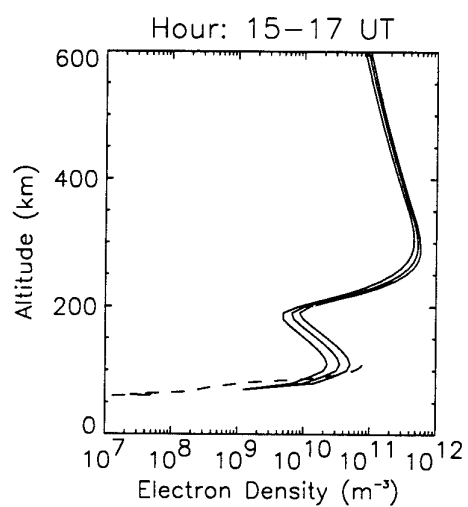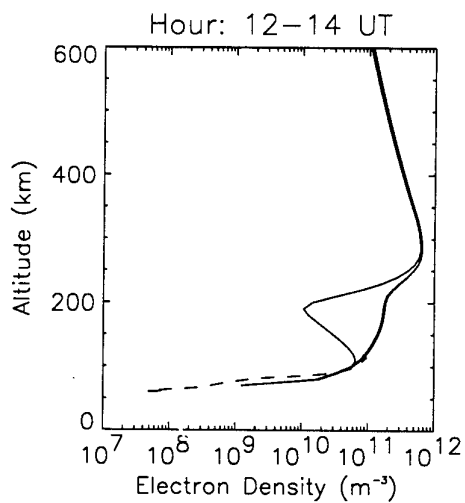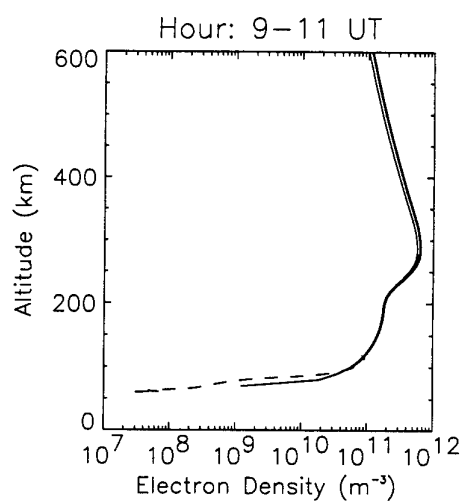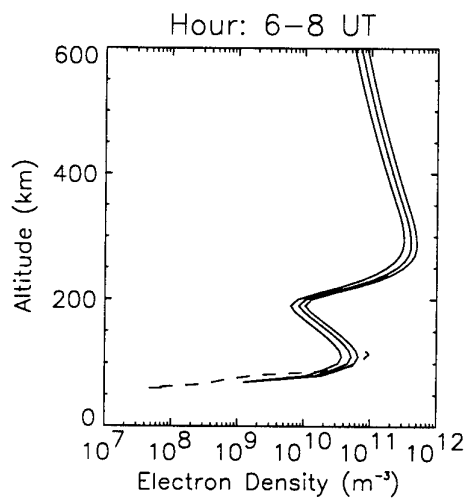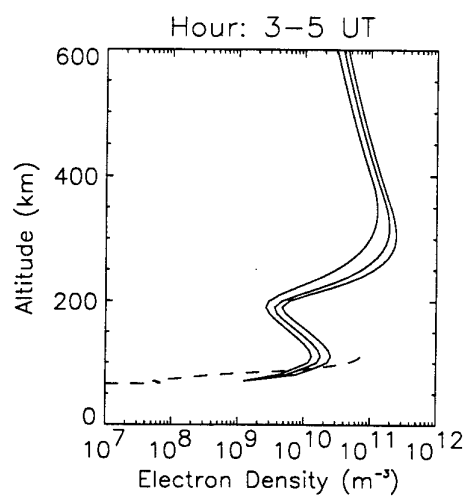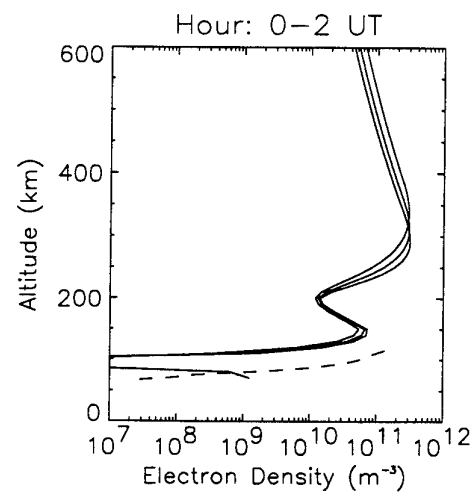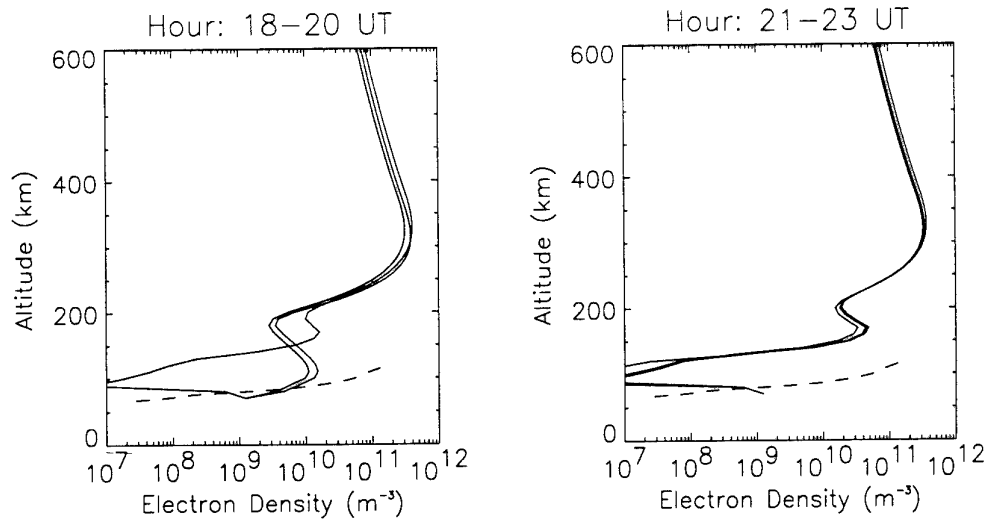
*Figur 7.10   ICED-model profiles (continous lines) and F & T-model profiles (dashed
line) for the midpoint of the path Andøya-Alta for the month of March,
Q=3. Three consecutive hours are shown for the ICED-model, whereas
the F & T-model is shown for the mid-hour only*

For Q=3, the ICED-model selects auroral night profiles for the hours 20-02 UT. The F_2-layer is Chapman, there is no F_1-layer, and the auroral E layer has a Chapman structure at the critical frequency and below, with en exponential extention on the topside of the layer.

A strange feature is observed below 90 km for some of the ICED profiles at night (e.g. hours 21-23 UT). They seem to give increased electron densities in the D-region. This effect is entirely due to the extrapolation routine being used from 90 km down to 70 km, which fixes the electron density at 70 km at a constant value. This obvious model deficiency has little effect on ray path calculations, but if this model electron density profile should be used in absorption predictions, the result will not be correct.

The midpoint of the path is within the subauroral trough region for the hours 1,2, 19 and 20. In this case, the scale height of the F_2-layer has been increased. For the hours 18-20, the ICED profiles changes from a mid-latitude profile at 18 UT via a sunrise/sunset mid-latitude profile at 19 UT to an auroral night profile at 20 UT. The latter is shown with a maximum auroral E-layer density at an altitude of 160 km. For the rest of the hours, low/midle-latitude profiles have been selected.

Comparing the ICED-model with the F & T-model, the agreement is good during day hours as it is for Q=0. When the ICED-model selects the auroral night time profile, the electron densities are greatly underestimated compared with those of the F & T-model. The difference is up to four orders of magnitude if we compare the electron densities at a specific altitude, for instance at 100 km. We can also consider the ICED- profile as

Q=6:

Hour: 0-2 UT

Hour: 3-5 UT

Hour: 6-8 UT

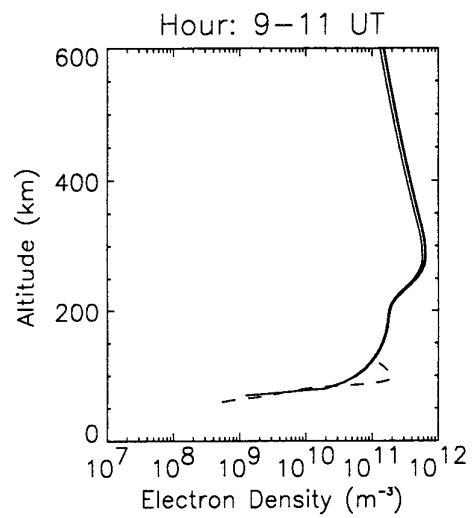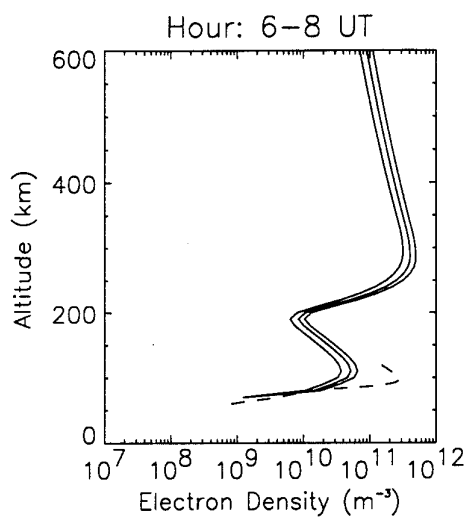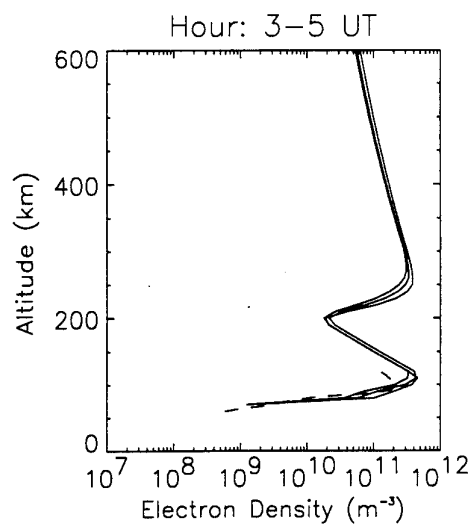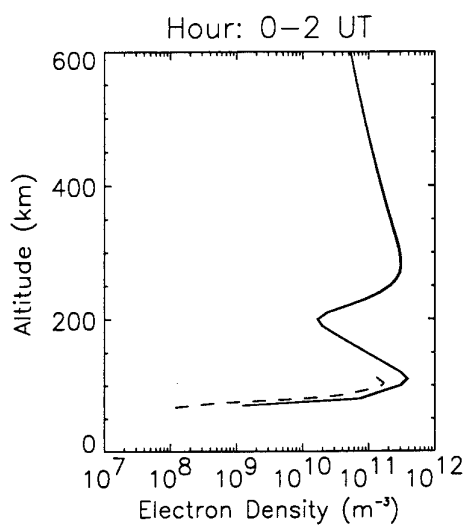Hour: 9-11 UT

Hour: 12-14 UT

Hour: 15-17 UT
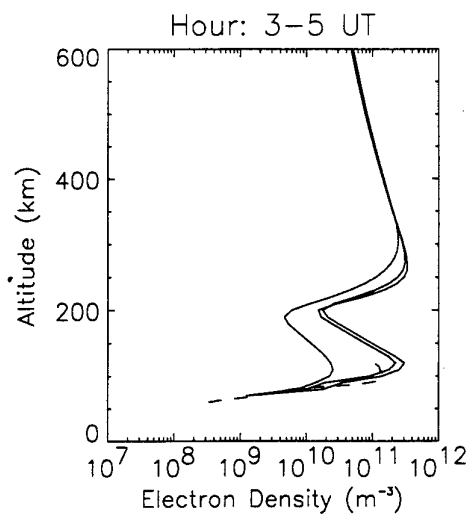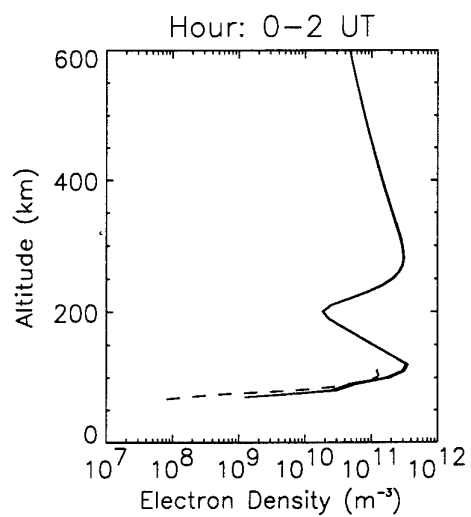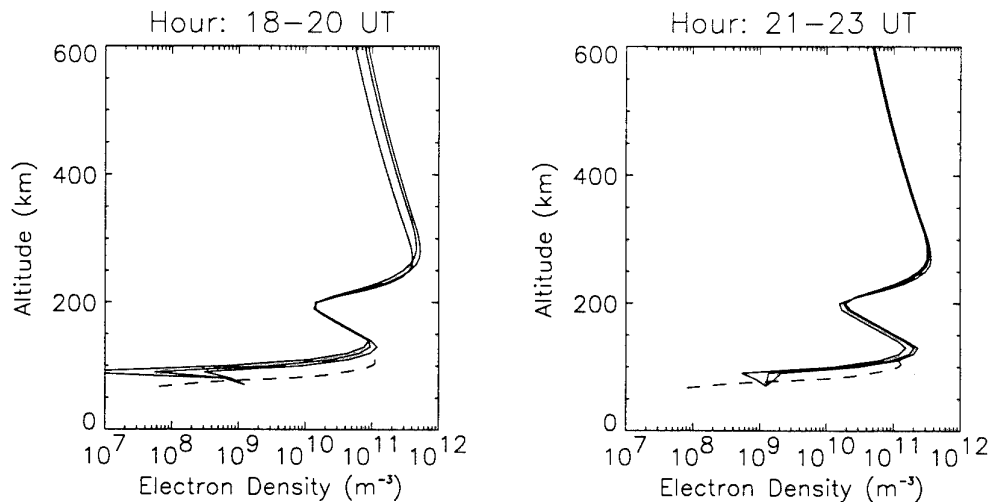
*Figur 7.11   ICED-model profiles (continous lines) and F & T-model profiles (dashed
line) for the midpoint of the path Andøya-Alta for the month of March,
Q=6. Three consecutive hours are shown for the ICED-model, whereas
the F & T-model is shown for the mid-hour only*

displaced vertically by 50-70 km compared to the F & T-model electron densities.

For Q=6 the ICED model gives an auroral night time profile for the same hours as for
Q=3, 20-02 UT. The critical frequency of the auroral E-layer has for these hours
increased to above the critical frequency of the F_2-layer. The hours 3-5 UT show a
"decreasing" ICED profile despite the decreasing solar zenith angle. The reason for this
is that the midpoint of the path is successively classified in the ICED-model as an auroral
sunrise/sunset point, an auroral daytime point and a low/middle latitude daytime point.
The E-layer of the auroral daytime profile consists both of a solar component and an
auroral component. In the evening, from 16 UT to 20 UT, the ICED profiles again
change back again from a low/middle latitude profile via an auroral daytime profile and
an auroral sunrise/sunset profile to an auroral night time profile.

The F & T-model agrees well with the ICED-model in the post-midnight sector. In the
pre-midnight sector, ICED underestimates the D-region densities with orders of
magnitude. For the day hours, they correspond well below 90 km but the ICED-model
gives too small densities above that height.

Q=8:

Hour: 0-2 UT

Hour: 3-5 UT

Hour: 6-8 UT

Hour: 9-11 UT

Hour: 12-14 UT

Hour: 15-17 UT
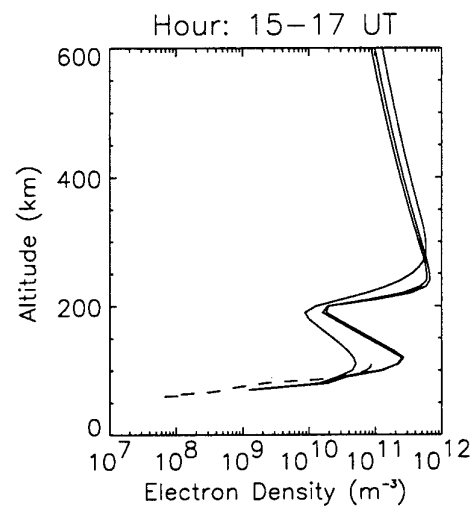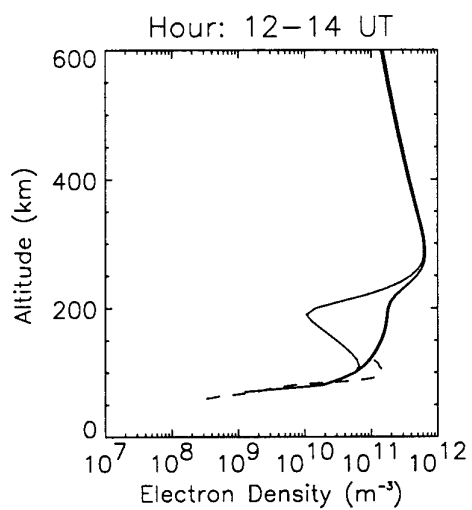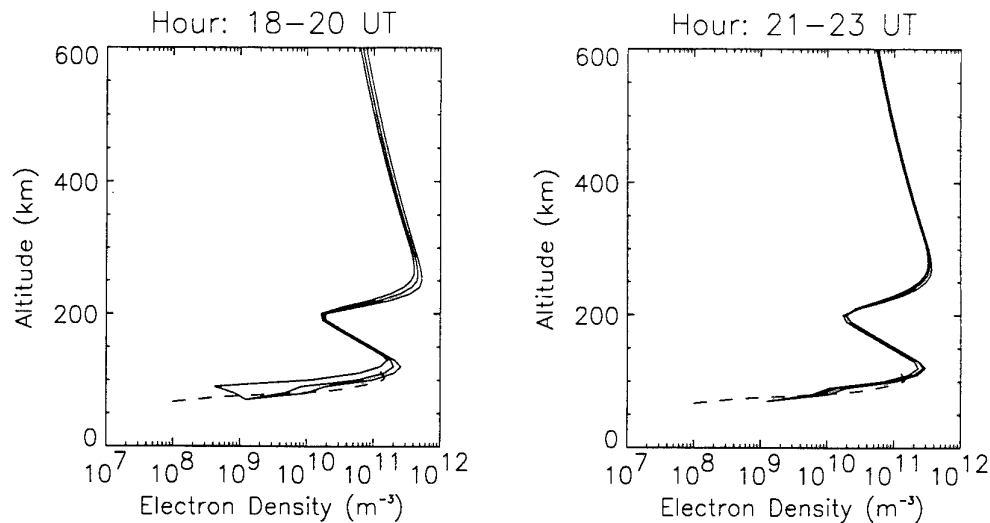
*Figur 7.12   ICED-model profiles (continous lines) and F & T-model profiles (dashed
line) for the midpoint of the path Andøya-Alta for the month of March,
Q=8. Three consecutive hours are shown for the ICED-model, whereas
the F & T-model is shown for the mid-hour only*

The characteristics of the profiles for Q=8 are very similar to those for Q=6 except for a
slightly longer persistence in time of the auroral ICED-profiles. For this high
geomagnetic activity the similarity between the F & T-model and the ICED-model is
amazingly good for night-time. Again, the ICED densities during daytime above 90 km
are up to an order of magnitude too low compared with the F & T-model.

The comparisons in this section between the F & T-model and the ICED-model in the
overlapping heights, have yielded some interesting and unexpected results.

The extrapolation in ICEPAC of the ICED-model down to 70 km gives some peculiar
results, and should not be considered as part of the ICED-model.

For low geomagnetic activity, the ICED-model underestimates the electron densities in
the lower E-region with orders of magnitude at night-time, but gives good agreement
with the F & T-model electron densities during daytime. For high geomagnetic activity,
the situation is reverse: At night, the ICED-model agrees amazingly well with the F & T-
model whereas for daytime the ICED-densites are too small. Thus the difference between
the two models does not in general increase with increasing Q, but it changes character.

The difference between the F & T-model loss calculations and the predictions in the
foregoing section (Figure 7.8) increased with Q. The main problem of the prediction of
ionospheric absorption is therefore not so much the existing electron density model, but
rather the semi-empirical formula used in the calculations. We think it is important that
the ICED-model be extended downwards to include the D-region, and corrected at those
altitudes where discrepancies are pronounced between the F & T-model and the ICED-

model. It is even more important that the absorption is calculated in a physically correct way from realistic electron density profiles.

7.7   Inclusion of the F & T-model electron densities in ICEPAC

The next step in our evaluation of the alternative way of predicting ionospheric absorption, is to use the electron densities specified by the F & T-model and the appropriate integration formula for ionospheric loss, in the ICEPAC programme. Our purpose is to change the internal electron density profiles used by ICEPAC according to the F & T-model at altitudes below 120 km and keep the ICED-values unchanged above that height. Then ionospheric absorption can be found by integration through the complete electron density profile up to the virtual height of reflection, using Equation (7.6).

Ideally, the F & T-model electron densities at 116 km altitude for night-time and 119 km altitude for day time should be combined smoothly with the ICED electron densities over some small height interval Δh. This would represent a physically consistent model. ICEPAC uses exponential extensions of the electron densities above maxima of the layers. We have chosen *not* to combine the two electron density profiles properly since the collision frequency v is decreasing exponentially with altitude, and the contribution to the total loss is small above 120 km.

For the ionospheric loss calculation both in Section 7.3 and in this section, we have integrated Equation 7.6 only up to the altitude at which the F & T-model stops (119 km-day, 116 km-night). For an actual ionospheric path this is not correct since the upper limit of integration should be the real height of reflection. However, the error thus obtained is small for the same reason as above. We estimate the maximum error as follows: We assume a collision frequency $v(h)=v_{120}\cdot\exp(-(h-h_{120})/16)$ (Hz) above 120 km where the pressure scale height is 16 km (used in ICEPAC). The electron density in the height interval between maximum of the F & T model, $N_{F\&T,max}$, and minimum of the ICED-model is set equal to $N_{F-T,max}$, according to Figure 7.13. From the minimum electron density of the ICED-model up to the virtual height of reflection, the ICED-model is used, and the product $N(h)\cdot v(h)$ is integrated over the whole interval. The error thus obtained for any hour, frequency and Q-value was maximum 12 % of the total ionospheric loss. In most cases it was much less than 10%. Because of the uncertainty of other parameters used in prediction programmes, we feel that integrating the electron density profile only up to 119 (116) km to find an estimate of ionospheric loss, is justified.

When ICEPAC electron densities are exchanged with the F & T-model in the D and lower E-region, new propagation modes may appear. The virtual height of reflection may be different for these new modes as compared to the modes propagating in an

unmodified electron density profile. The losses for the new modes are calculated, and the most reliable mode will be chosen accordingly. The total circuit reliability is calculated taking all the propagating modes into account.
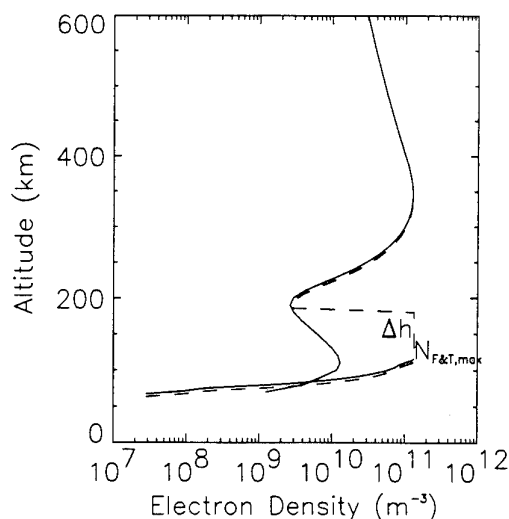

Figure 7.13   *Estimating maximum error when the F & T-model and the ICED-model are not smoothly combined*

7.7.1   Software implementation

ICEPAC has a software option of using external electron density profiles specified in a datafile. We used this option to create external electron density profiles for each hour, consisting of the F & T-model up to about 120 km and the ICED-model above 120 km.

To incorporate the F & T-model correctly in ICEPAC, several steps had to be made:

* ICEPAC was run with the external electron density profiles, storing on files *all* possible propagating modes and their virtual height of reflection.

* The mode information was then used in a separate programme to calculate the ionospheric loss for each possible mode using Equation (7.6).

* The calculated losses were read from files into ICEPAC and exchanged with the three loss-terms (described in Section 7.4) already existing in ICEPAC.

* ICEPAC was then run again for each hour using the external electron density profiles *and* the externally calculated losses.

This method of incorporating the F & T-model in ICEPAC is ad-hoc and manual, but for a particular electron density profile it should yield both correct reflection heights and absorption.

7.8   Modified predictions - loss and virtual height of reflection

Using the method described in Section 7.7 with the F & T-model included, new predicted virtual heights of reflection and ionospheric loss for the most reliable mode can be obtained. We have only considered the four lowest frequencies (3.0 - 8.5 MHz) used in our HF test measurements since data exist basically at these frequencies. Predictions and data will be compared in the next chapter. New virtual heights of reflection for the most reliable mode is shown in a three dimensional plot, Figure 7.14.
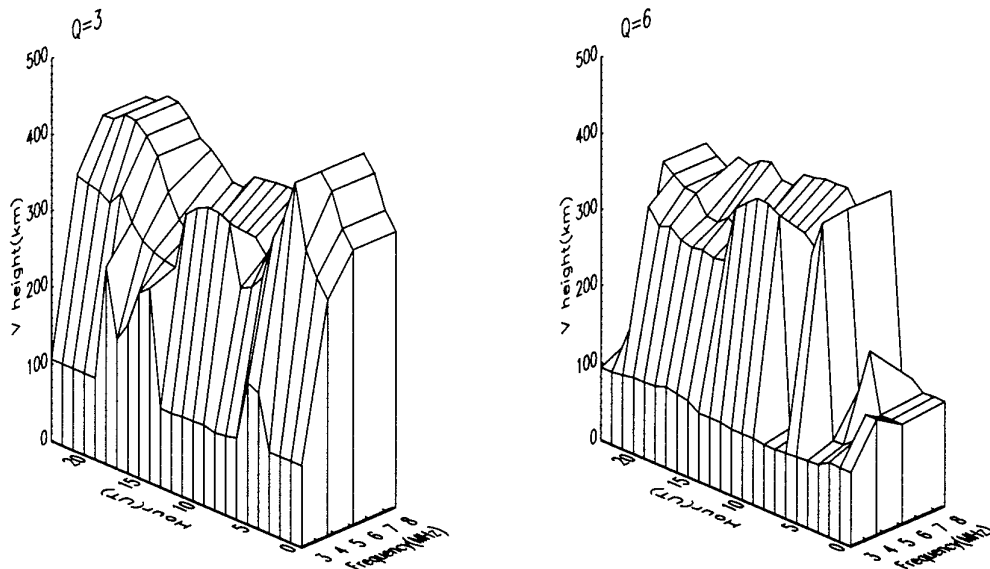
Figure 7.14   New virtual heights of reflection with the F & T-model inserted for the path Andøya-Alta (285 km)

When comparing the new predicted virtual heights of reflection with the virtual heights produced by ICEPAC unmodified (Figure 6.5), the modified ICEPAC yield E-layer reflections at 3 MHz at most times, both for Q=3 and Q=6.

Because the modes have changed, so have the calculated ionospheric losses from Section 7.3. New calculated losses based on new virtual reflection heights are shown in Figure 7.15. If the virtual height has changed from above 119 (116) km to below, there are two effects on the calculated ionospheric loss: The loss increases due to an increased angle of incidence φ, *and* the loss decreases due to a reduced upper integration limit. These two effects might partially cancel, and the net effect is not predictable. An example where a

reduction of virtual height has resulted in *increased* absorption compared to Figure 7.5, is the hours before midnight for f=3.0 MHz and Q=3. An example where the reduction of virtual height has resulted in *reduced* absorption is the hours centered around 8 UT for f=3.0 MHz and Q=6.

The F & T-model absorption calculation based on new predicted virtual heights intuitively seems better than the old absorption calculations (Figure 7.5). It is more correct to use predicted virtual heights based on realistic electron density profiles (represented by the F & T-model). Although the plot looks smoother, there are still hourly fluctuations of the loss, which are not realistic for a model. This is caused by the varying riometer absorption given as input to the F & T-model. A more accurate relationship between geomagnetic activity Q and riometer absorption L_r can probably be found if more data are compared (Section 7.2), and this would smoothen the plots even more.

The main features of Figure 7.15 are: As Q increases, the maximum absorption moves in time from noon to the morning hours. The general level of absorption at all frequencies increases, and the increase of absorption is relatively larger at higher frequencies (e.g. 4.5 MHz compared to 3 MHz). These features show that including the F & T-model as part of ICEPAC yields a realistic model of ionospheric loss.
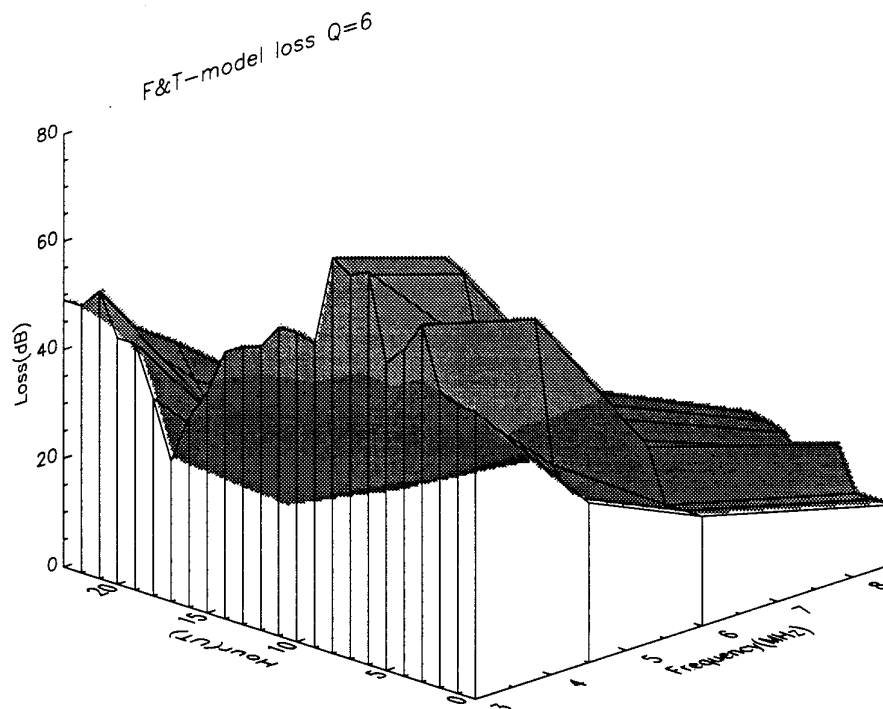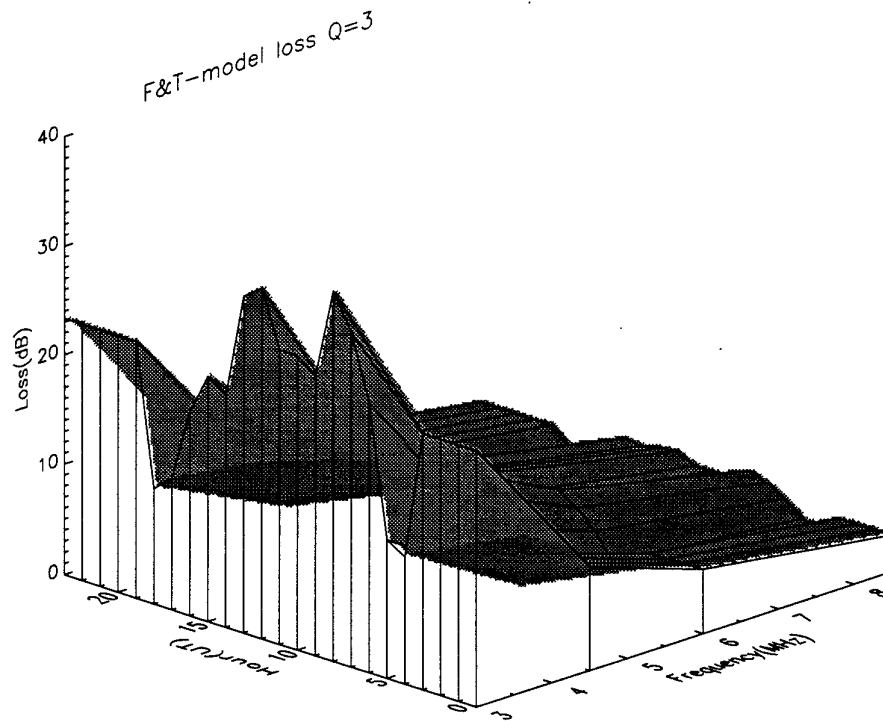
Figure 7.15   F & T-model loss using predicted virtual heights (Figure 7.14) for the path Andøya-Alta (285 km)

8   DISCUSSION: COMPARISONS OF DATA AND IMPROVED PREDICTIONS

The purpose of our modifications to ICEPAC is to improve the predictions of signal strength by incorporating a new loss model. The existing loss model is particular poor at high latitudes, since the semi-empirical loss equations inherent in ICEPAC are based on low latitude data only. To evaluate the modified ICEPAC, the new predictions should be compared with our HF test data collected at the high latitude path Andøya-Alta.

The method of comparison and the quantities compared, reliability and virtual height of reflection, were presented in Section 6.1. The shortcomings of the existing ICEPAC programme were pointed out in Section 6.3. In this chapter we do the same comparisons with the *modified* ICEPAC. The results have been published in Jodalen and Thrane (6). We continue the special study of the period March/April 1988. We here concentrate on the four lowest frequencies in the set of measurements, since data at higher frequencies are very rare. The two data sets for Q≤4 and Q>4 are shown again here for convenience (virtual height, Figure 8.1, and reliability, Figures 8.2 and 8.3). The reliability-data are shown here from two different viewing angles.

8.1   Achievements by including the F & T-model

8.1.1   Virtual height of reflection

Figure 8.4 shows a graphical comparison between:

- the median of the virtual heights measured on the test path,

- predicted virtual height of the unmodified ICEPAC

- and predicted virtual height after the F & T-model has been included.

When comparing first the unmodified ICEPAC prediction of virtual height with the prediction including the F & T-model for Q=3, significant changes can only be seen at 3.0 MHz. The discrepancies occur in the afternoon and at night. For Q=6, there are some changes of virtual height at night and in the morning also for 4.5 MHz and 6.0 MHz. The inclusion of the F & T-model has generally lead to a decrease from F_2-reflection heights to E-reflection heights for the lowest frequencies. This is due to the increased electron densities of the F & T-model at night.

The database for this month is small (16-17 days) and neither the mean nor the median (used here) are perfect statistical measures.

When comparing the median of data with modified predictions for Q=3 and f=3.0 MHz, the F & T-model seem to have made the prediction worse at night time. However, the distribution of data (Figure 8.1) shows that there are many messages reflected also in the E-region which is consistent with the modified prediction. Besides, the ambiguity of the virtual heights above 300 km could hide two-hop modes reflected in the E-region at night.

For Q=6, the modified prediction predicts more E-region reflection heights at the lowest frequencies. This can also be seen in the data (4.5 MHz, Figure 8.1), so the trend is correct. The F & T-model has nevertheless *not* given considerably more E-layer reflections for pre-midnight hours, which was expected from the comparison of electron density profiles in Section 7.6. We cannot conclude that the F & T-model really *has* improved the prediction of virtual height. The real test of the F & T-model will be the comparison of reliability in the next section.
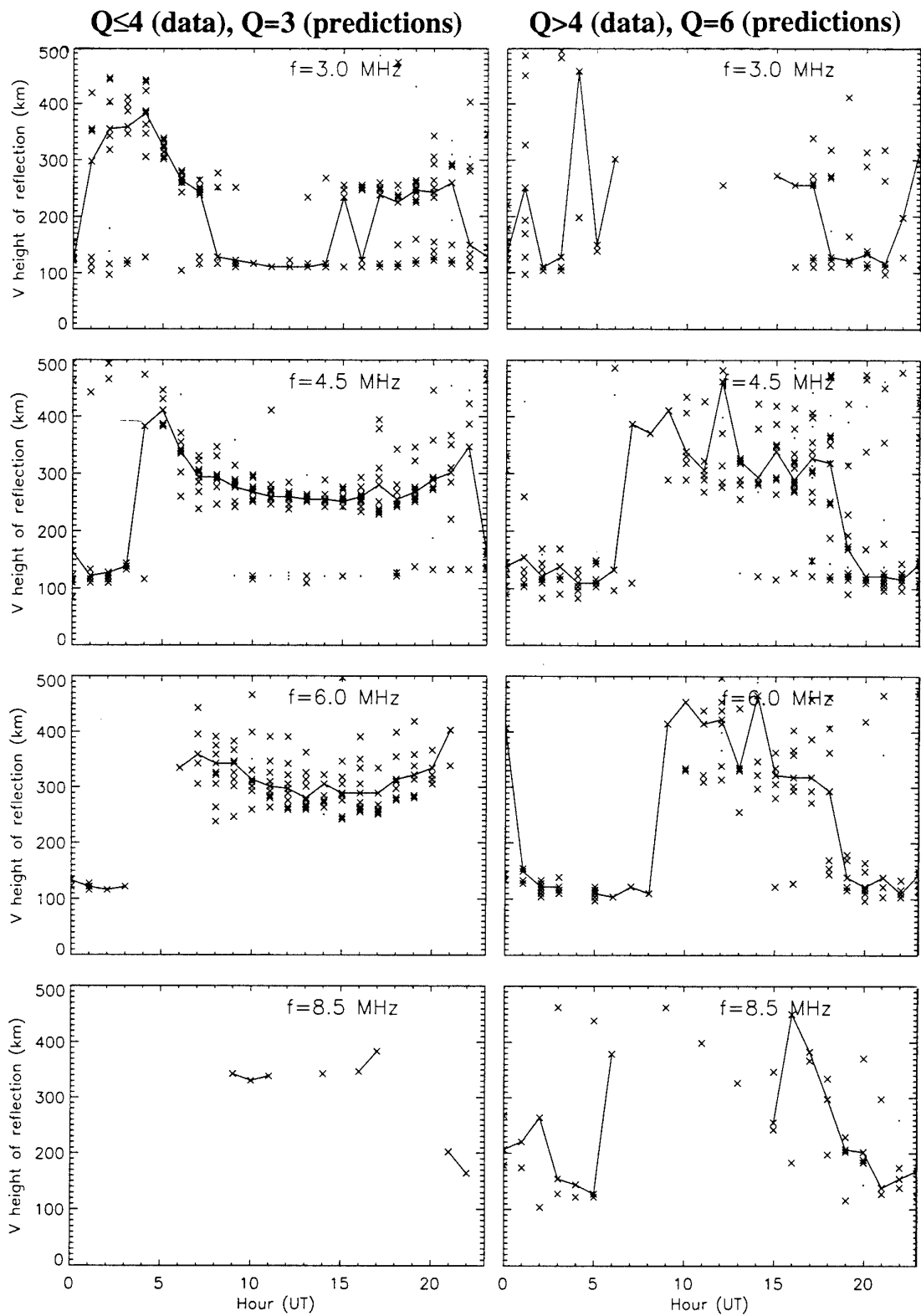
Q≤4 (data), Q=3 (predictions) **Q>4 (data), Q=6 (predictions)**

Figure 8.1   Measured virtual height of reflection, Andøya-Alta (285 km), March/April
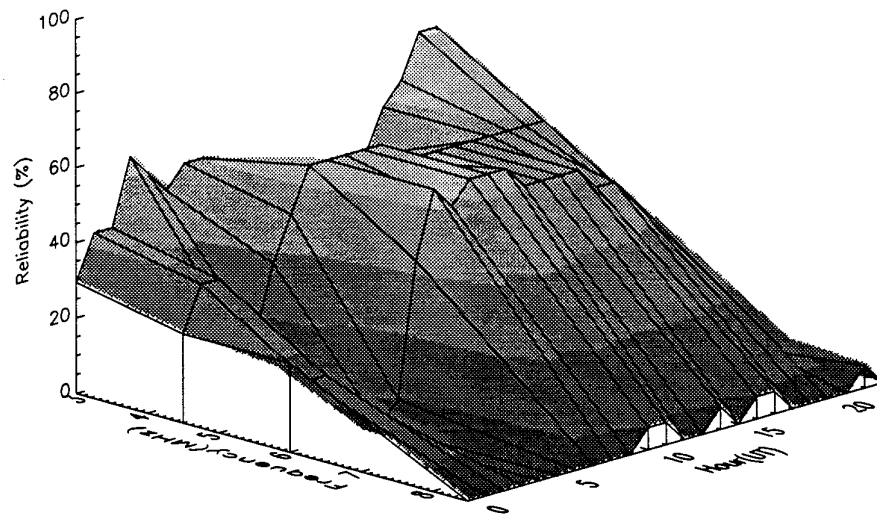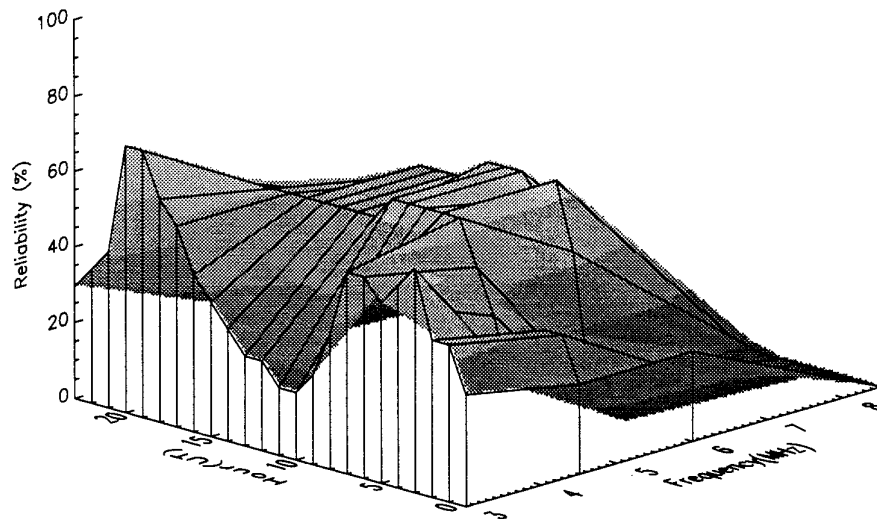*1988. Median of data drawn as a continous line. Small dots indicate*
multipath

Q≤4:

Figure 8.2   Measured reliability, Andøya-Alta (285 km), March/April 1988, days where
Q≤4. Two different viewing angles

Q>4:

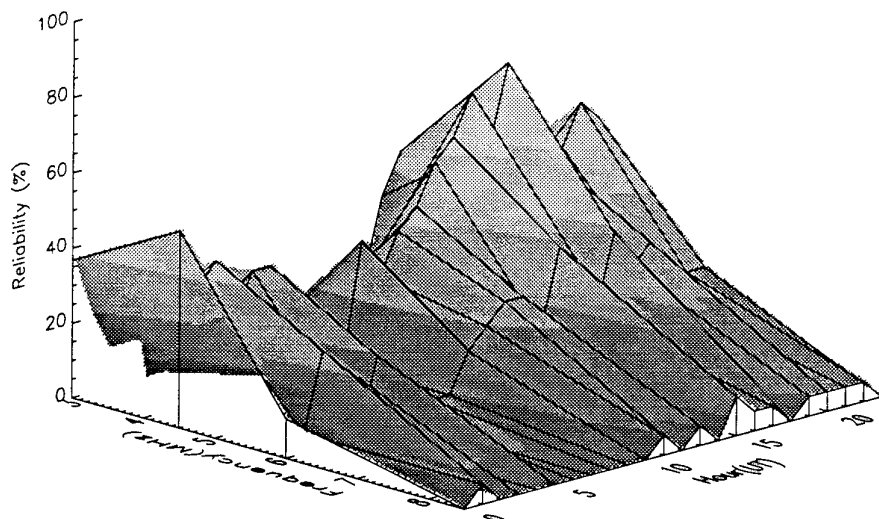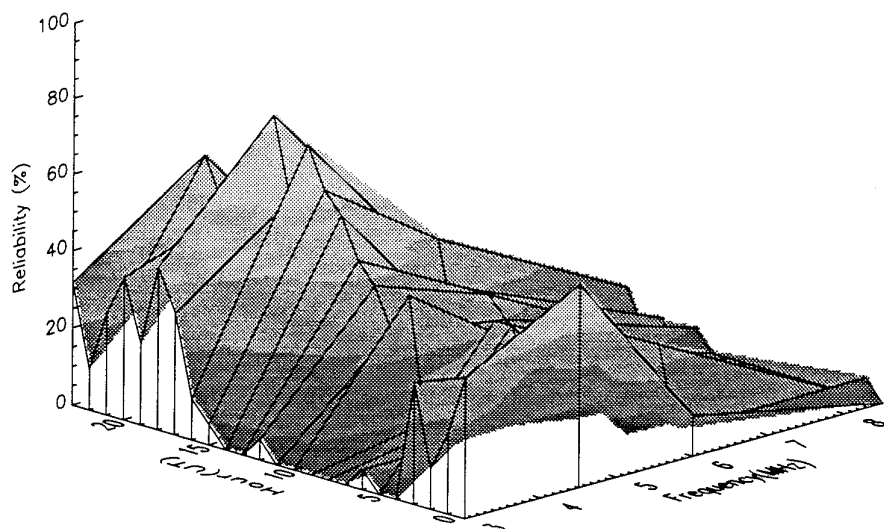*Figure 8.3   Measured reliability, Andøya-Alta (285 km), March/April 1988, days where*
         Q>4. Two different viewing angles

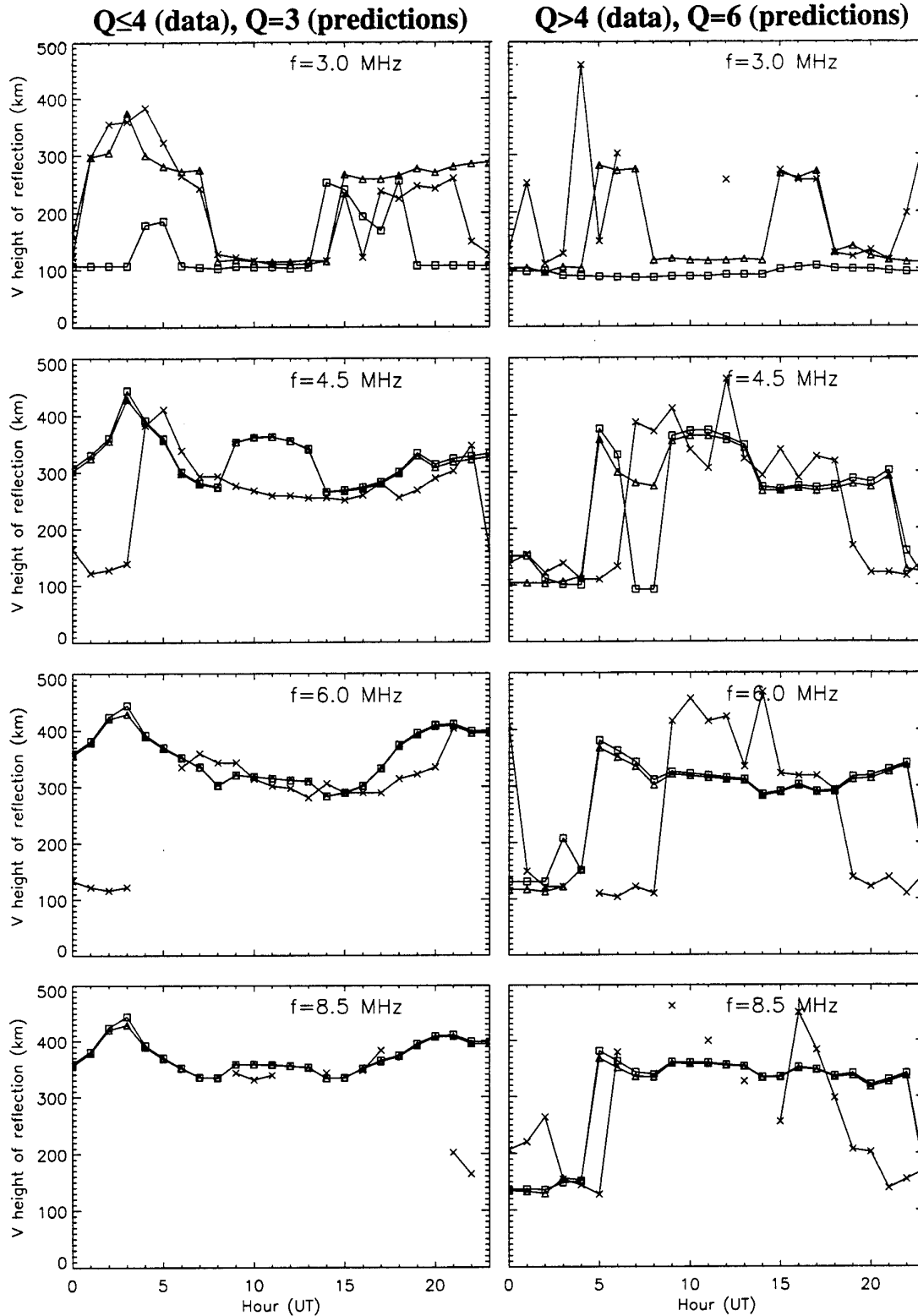*Figure 8.4 Virtual height of reflection for median of measured data (X), unmodified
predictions(Δ) and predictions with the F&T-model included ([]). Path
Andøya-Alta (285 km), March/April 1988*

8.1.2   Reliability

The reliability predictions without and with the F & T-model included is shown in the upper and lower parts of Figure 8.5 and 8.6, respectively. Figure 8.5 displays a prediction with Q=3 (low geomagnetic activity) and Figure 8.6 shows higher geomagnetic activity with Q=6.

For both levels of geomagnetic activity, the influence of the F & T-model on the reliability predictions decreases as the frequency increases. For Q=3, it is negligible above 4.5 MHz, and for Q=6, above 6 MHz. Because f^2 appears in the denominators in the equations for ionospheric loss, Equations 2.16 and 4.2, this is to be expected.

For Q=3, the predicted reliability has been reduced from 90 % to about 80 % for f=3.0 MHz, which is still far above the measured reliability (20 % - 70 % in Figure 8.2). Since the absolute level of measured reliability and predicted reliability should be compared with caution as pointed out in Section 6.3, we again compare the similarity coefficients k(N) between data and modified prediction in Figure 8.7.

The k(N) of the modified prediction should be compared with the k(N) of the unmodified prediction (Figure 6.8 Section 6.2.2). The total similarity coefficient k(96) over all hours and frequencies has for Q=3 actually decreased by 4 % from 0.71 to 0.67 after the inclusion of the F & T-model. The similarity for each hour over all frequencies k(4) are also in general smaller. However, a small, but correct diurnal variation now seen in the predictions causes the similarity at the two lowest frequencies over all hours, k(24), to increase.

We conclude that the inclusion of the F & T-model has not lead to any significant improvement of the similarity between data and predictions for Q=3. Nevertheless, the overall decreased reliability of data at the lowest frequency is now reflected in the prediction. Also, a correct trend of diurnal variations of reliability at the lowest frequency can be seen.

For Q=6, the predicted reliability at 3.0 MHz has been reduced from around 90 % at all times of day to about 10 % in the morning hours, and a maximum of 80 % in the late afternoon. The same tendency is also visible at 4.5 MHz and 6.0 MHz. Compared to data (Figure 8.3), this is still an optimistic prediction, but the marked diurnal variation now seen gives a good picture of the real data.

This improved prediction of reliability under disturbed geomagnetic conditions is quantified in Figure 8.7 for each hour and frequency. The total improvement of similarity over all frequencies and hours is rather small, the increase is only 1 % to 0.55. However, the diurnal variation now incorporated by the F & T-model results in considerably better agreement at frequencies from 3 MHz to 6 MHz compared to Figure 6.8 Section 6.2.2.

As for Q=3 but even more pronounced, the main improvement is the overall decrease of reliability at the lowest frequencies and the incorporation of diurnal variation of absorption.
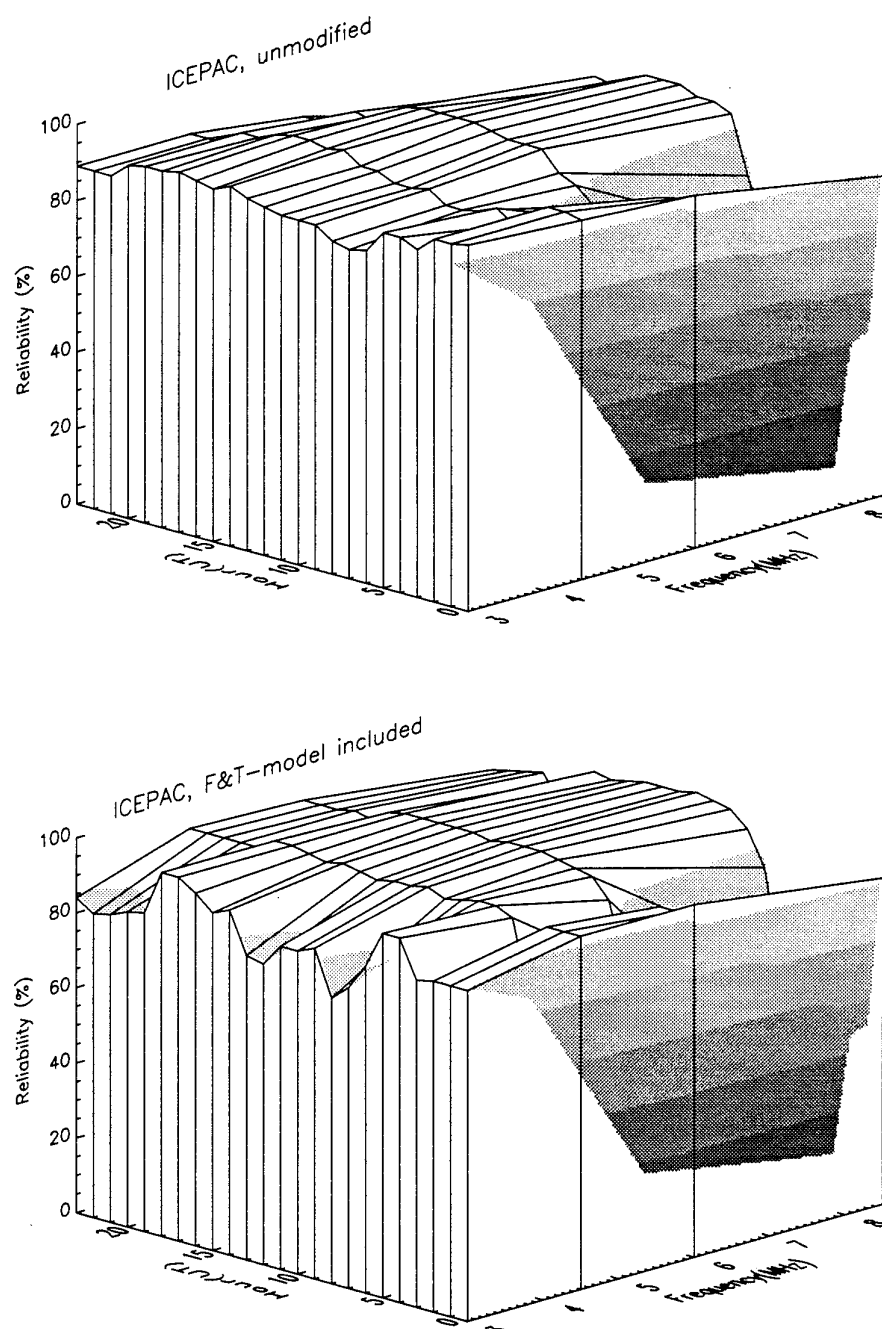
Q=3:

Figure 8.5 Unmodified prediction above, ICEPAC prediction with the F & T-model included below. Andøya-Alta (285 km), March 1988, SSN=71
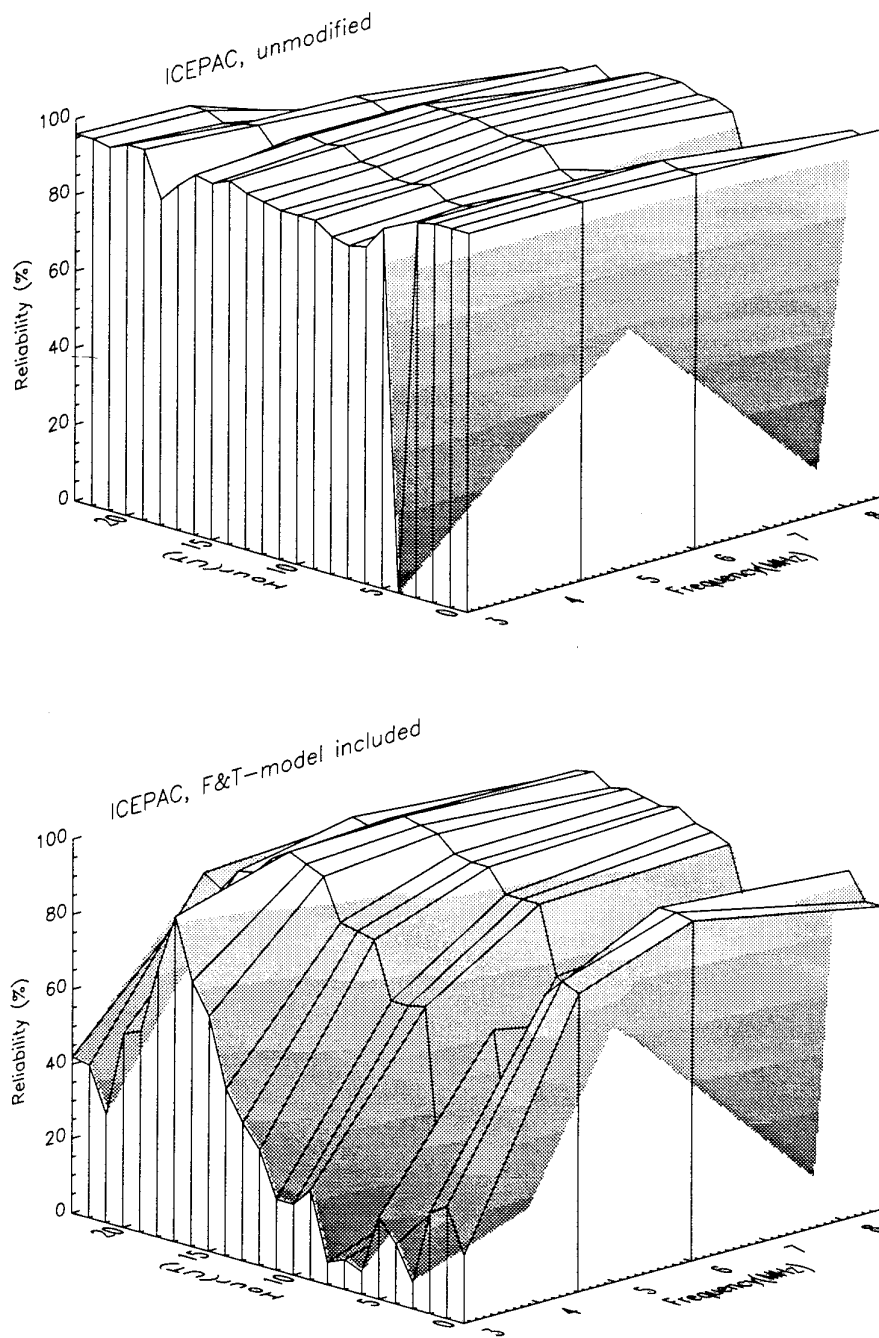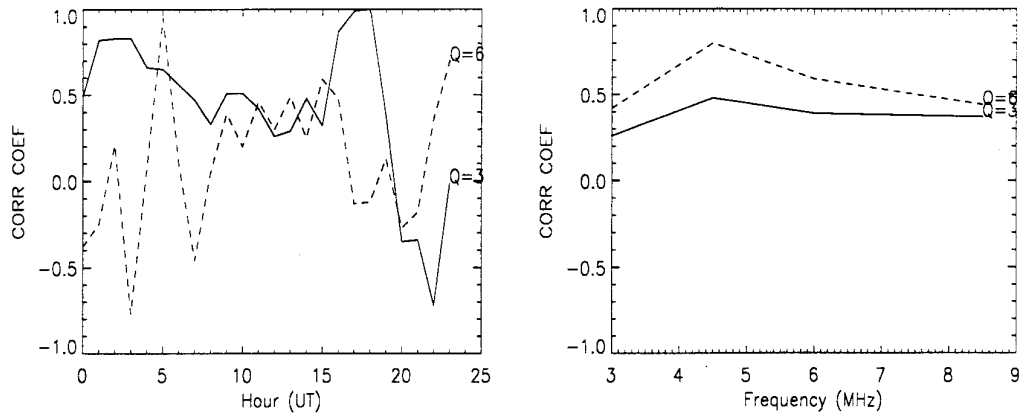
Q=6:

Figure 8.6   Unmodified prediction above, ICEPAC prediction with the F & T-model
included below. Andøya-Alta (285 km), March 1988, SSN=71

Figure 8.7   Similarity coefficients (corr coef) between reliability of measured data and reliability predicted by ICEPAC including the F&T-model. Andøya-Alta (285 km), March 1988

8.2   Reliability at frequencies around the MUF

The inclusion of the F & T-model made the prediction of reliability more similar to the data at lower frequencies. There are still large discrepancies between data and predictions at the higher frequencies with the predictions being much too optimistic. ICEPAC does not calculate MUF as a monthly median corresponding to a reliability of 50 % at the MUF. It includes instead the possibility of other propagation mechanisms at frequencies around the MUF, and calculates a reliability at the MUF which is much larger. The MUFs for the period studied are in the range 3.5-7.7 MHz, and we see from the figures that the reliability at these frequencies is more than 90 %. Comparisons with the data (Figures 8.2 and 8.3) show that this approach leads to a significant overestimate of the reliabilities at and above the MUF. Based on our data, we believe that the need for a propagation mechanism above the MUF is overestimated.

The two ways of calculating reliability described in Section 4.3.2 are both attempts to describe the real world. Neither of them needs to be wrong, but one might be more successful than the other. Argo (53) claims that the current IONCAP/ICEPAC model is wrong, and he describes what he believes to be mixing of terms. The alternative way of calculating circuit reliability R_c as described in Section 4.3.2, is based on the equation (Goodman (9)):

$$R_c = q_1 \cdot P_1 + q_2 \cdot P_2 + q_{12} \cdot P_{12} \tag{8.1}$$

where q_n is the probability that mode n exists, P_n is the probability that the S/N-ratio for mode n exceeds a required level, q_{nm} is the probability that modes n and m exist simultaneously and P_{nm} is the probability that the combination of mode n and m exceeds

the required level. The formula is here written including two modes only, but should include all possible modes and their simultaneous probabilities. The number of modes will nevertheless be limited because of the ionospheric properties. This method was implemented in earlier versions of ICEPAC, e.g. ITS-78, but was discarded because some measurements showed that the resulting prediction was too pessimistic and that there was a need to incorporate above-the-MUF propagation.

We decided to try a similar method of calculating reliability, with a hope to achieve more realistic predictions at the upper frequencies. The following arguments support this method:

q_n is purely a function of the MUF and the actual frequency, whereas P_n is a function of path, power, absorption and noise. The physical relations between the two parameters are very complex, and for this reason we assume as a working hypothesis that q_n and P_n are statistically independent as long as above-the-MUF losses are excluded from the signal strength calculations. They can therefore be multiplied.

To include the term above-the-MUF-loss instead of computing mode probability seem an artificial way of modelling propagation mechanisms at frequencies above the MUF. Multiplying q_n by P_n to get the probability of achieving a certain SNR-ratio by ionospheric reflection alone seems to be physically more correct. It does possibly not include other propagation mechanisms such as forward scatter, reflection at inhomogenities and at ionospheric electron density tilts, but if needed, these mechanisms should be modelled separately and independently. Argo (53) however, indicates that above-the-MUF propagation might be included in the MUF distribution, since this distribution normally is a chi-squared distribution or a two-slope log-normal distribution. If this is true, then other propagation mechanisms *are* included in the calculations, and reliability is not underestimated.

8.2.1   Implementation of mode availability in ICEPAC

Only minor changes to the program were necessary in order to implement the term mode availability, q_n. This term was already calculated, but not used anywhere in the program (FDAYS/PROB, probably a left-over from earlier versions of ICEPAC).

As a first step, we have excluded the term above-the-MUF loss from all loss calculations in order to make the signal strength calculations independent of the probability of ionospheric reflection. This results in large signal strength (relatively small loss) at frequencies that are expected to be well above the path MUF.

The second step is to multiply the reliability of all possible modes with their respective mode availabilities, q_n. This is done first for each hop combination (described in Section

4.4), and a most reliable mode (MRM) is chosen for each, based on the new reliability ($q_n \cdot P_n$). For each hop combination, the modes are then power summed, and a preliminary circuit reliability is calculated by multiplying the probability of the power sum exceeding the required level, $P_{n,...,p}$, by the mode availability of the MRM, $q_{n,MRM}$. The result can be expressed as $R_{c,pre} = P_{n,...,p} \cdot q_{n,MRM}$. This is not quite in accordance with Equation 8.1, but is a similar approach. For each of the three hop combinations there are now a MRM with parameters such as virtual height, loss, mode, etc., and a preliminary circuit reliability based on the power sum of possible modes and the mode availability for the MRM. These preliminary circuit reliabilities are now compared with the reliabilities calculated for a 1-hop E_s-mode and a 2-hops E_s-mode. The reliabilites of the E_s-modes consist also of a mode availability factor and a probability factor of the SNR exceeding the required level. A final MRM, with probability q_{MRM}, is now chosen among the five hop combinations (1-hop, 2-hops, 3-hops, 1-hop E_s, 2-hops E_s) based on the preliminary circuit reliability for each, and parameters mentioned above are stored as output. The five possible hop combinations (three of them consist of a power sum already) are finally power summed and the output circuit reliability is calculated by multiplying $P_{a,...,z}$ by q_{MRM}.

Since two single E_s-hop combinations are considered against three power summed other hop combinations, the probability that an E_s-hop combination is selected as the MRM is smaller, except possibly for those frequencies that penetrate the normal layers, but are reflected from an E_s-layer. The final circuit reliability used in our implementation of mode availability can be expressed as:

$$R_c = q_{MRM} \cdot P_{a,...,z} \tag{8.2}$$

where q_{MRM} is the mode availability of the selected mode (selected among maximum 20 possible modes based on their individual mode reliabilities), and $P_{a,...,z}$ is the probability of the power sum of all possible modes being larger than the required SNR. Comparing this equation with Equation 8.1, $P_{a,...,z}$ corresponds exactly to P_{12}. It is not trivial to calculate q_{12}, since the probability of the existence of mode 1 is not independent of the existence of mode 2. We have simplified the problem, and instead multiplied $P_{a,...,z}$ with the probability of the MRM. The q_{MRM} is expected to be larger than q_{12}, and this might compensate for the two missing terms $q_1 \cdot P_1$ and $q_2 \cdot P_2$.

The random phase approximation in ICEPAC is a valid approach for calculating average received power in a certain area a certain distance from the receiver. The multipath components arriving with different phases at the receiver causes amplitude fluctuations for narrowband signals if the receiver is moved around in a local area, but the average power will be equal to that of a broadband signal which give no particular amplitude fluctuations within the area.

8.3   Achievements by including mode availability

Although the inclusion of the F & T-model in Section 8.1 only gave a small improvement of the prediction of reliability for disturbed conditions, we believe that the F & T-model is a fundamentally correct way of calculating absorption. We will therefore keep it in the predictions when also mode availability is included.

Including mode availability as described in the preceding section, gives new reliability-values for each mode and thus a different choice of the most reliable mode. Virtual height and absorption calculations of ionospheric loss will therefore also change, but the differences are not so large that new figures similar to Figure 7.14 and 7.15 in Section 7.8 are necessary in this context. We will in the following subsections compare prediction of virtual height and reliability including both the F & T-model and mode availability, with data and unmodified predictions.

8.3.1   Virtual height of reflection

The new predicted virtual height is shown in Figure 8.8 in addition to the unmodified prediction and the median of the data. The changes of predicted virtual height from Figure 8.4 can be seen at the upper frequencies, where E-region modes at night have been selected more frequently as the most reliable mode.

Since the amount of data is very small on the two largest frequencies, it is difficult to state whether the new prediction represents an improvement, but it has selected a few more of the E-region data reflections at 4.5 and 6.0 MHz.
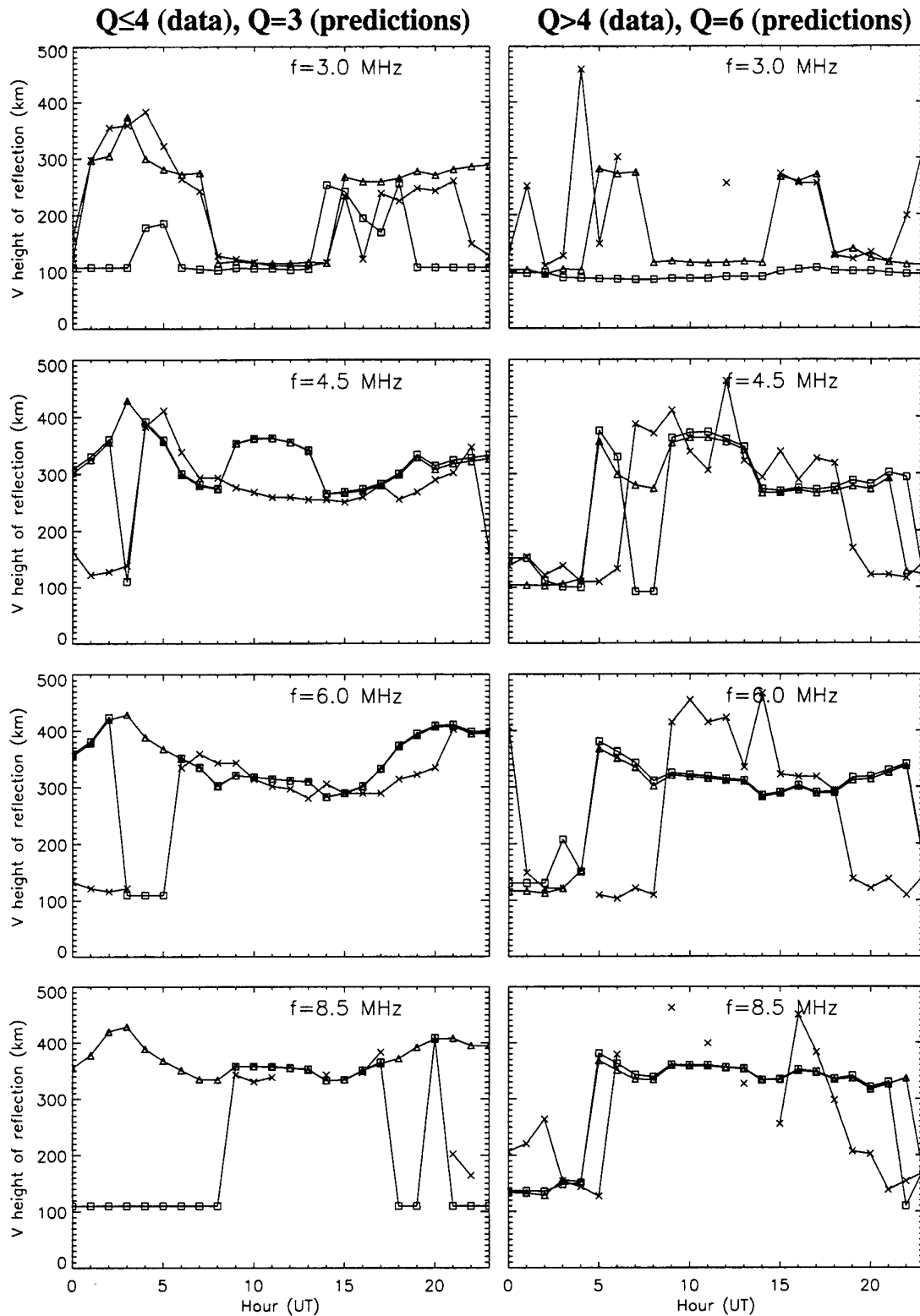
Q≤4 (data), Q=3 (predictions)   **Q>4 (data), Q=6 (predictions)**

Figure 8.8   Virtual height of reflection for median of measured data (X), unmodified
predictions(Δ) and predictions with both the F&T-model and mode
availability included ([]). Path Andøya-Alta (285 km), March/April 1988

8.3.2 Reliability

The new predicted reliability for Q=3 and Q=6 is shown in the lower part of Figure 8.9 and 8.10, respectively. The unmodified predictions are shown in the upper part. For the lowest frequencies, the shape of the reliability surface is similar, but not exactly equal to the shape of Figures 8.5 and 8.6. This shows that the multiplication by mode availability has caused slightly different choices of most reliable mode also for frequencies below the MUF (mode availability expected to be close to 1.0). Nevertheless, the reliabilities at these frequencies are in general very similar to the ones predicted with only the F & T-model included.

For the upper frequencies (6.0 and 8.5 MHz) there has been a big change by the inclusion of mode availability. For both levels of geomagnetic activity, the reliability has been reduced drastically. For instance, for Q=3, the reliability at 8.5 MHz has been reduced from 80 % to 0 % at night and from 90 % to less than 30 % around noon.

Including mode availability shows almost equal effects for Q=3 and Q=6 and brings the reliability at 6.0 and 8.5 MHz roughly to the same level for Q=3 and Q=6. This was not the case when the F & T-model only was included. The F & T-model brought a more intense depletion of reliability for Q=6 than for Q=3 at the lowest frequencies. The F & T-model is a model of absorption which correctly increases with increasing geomagnetic activity. Mode availability is a model of the propagation of radio waves. The propagation (mode structure) might change during increased geomagnetic activity, but it does not necessarily reduce the signal strength of certain modes, provided that the frequency is high enough to avoid the increased absorption. The effect of the F & T-model can be seen at the lowest frequencies and the effect of mode availability can be seen at the highest frequencies in Figures 8.9 and 8.10.

Comparing the new prediction for Q=3 with the data, Figure 8.2, and neglecting the absolute level of reliability, the shape of the predicted surface is now remarkably similar to the data.

The similarity coefficients between data and the new prediction are displayed in Figure 8.11. The similarity coefficient k(96) between all points on the surface is now 0.91, an increase of 20 % from the unmodified prediction. The k values have increased for all frequencies and all hours, compared both with Figure 6.8 (unmodified prediction) and Figure 8.7 (prediction with F & T-model).
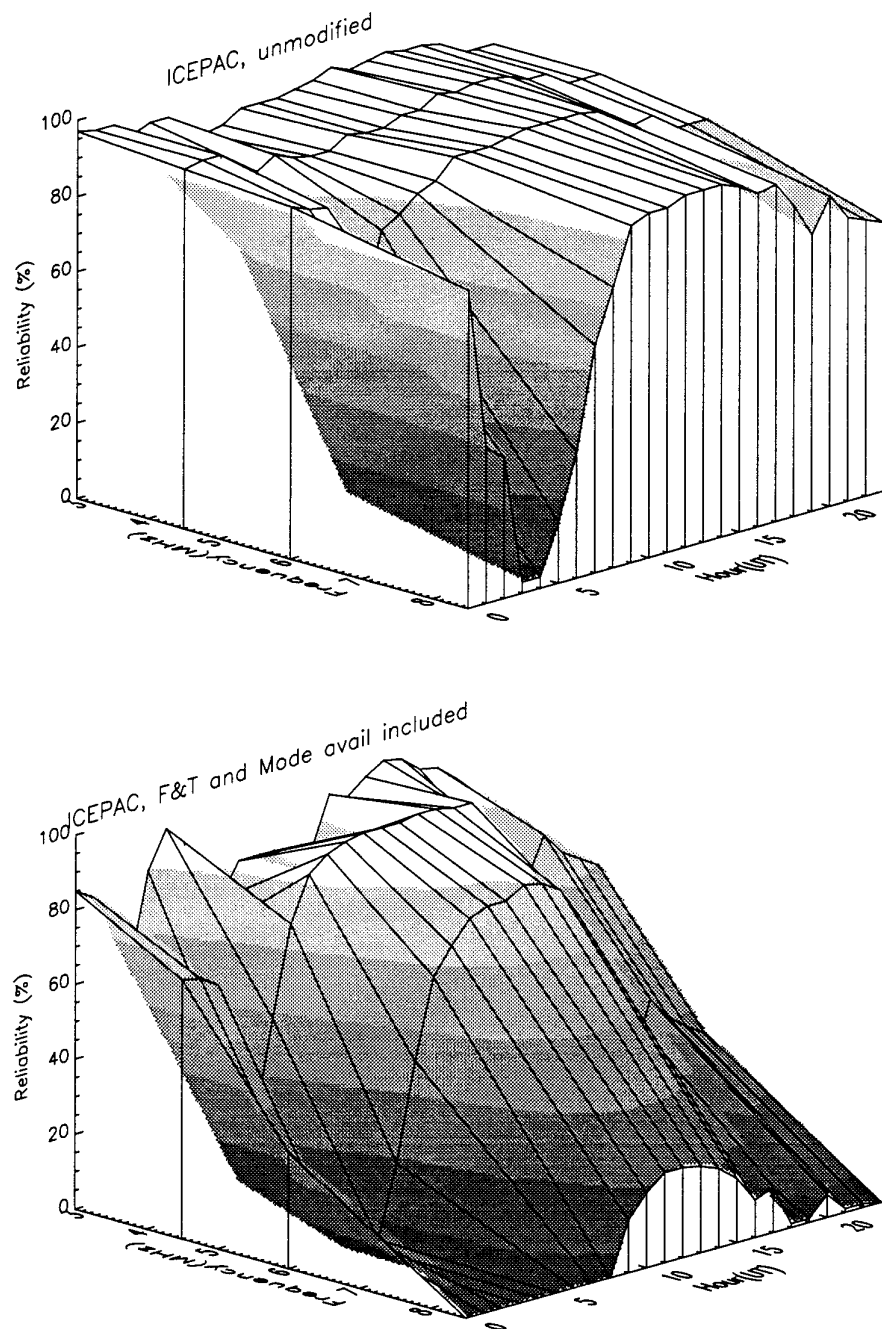
Q=3:

Figure 8.9 Unmodified prediction above, ICEPAC prediction with both the F & T-model and mode availability included below. Andøya-Alta (285 km), March 1988, SSN=71
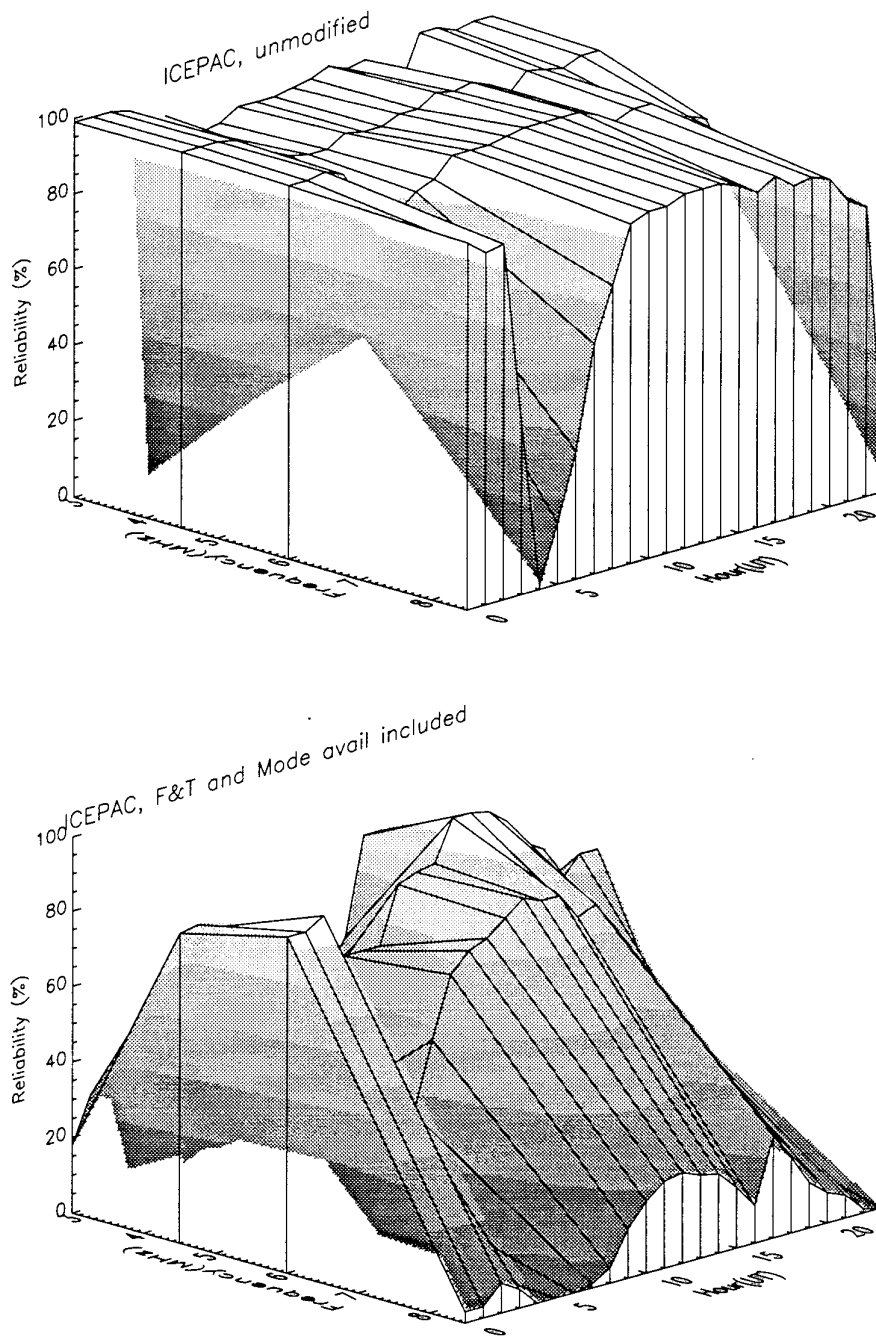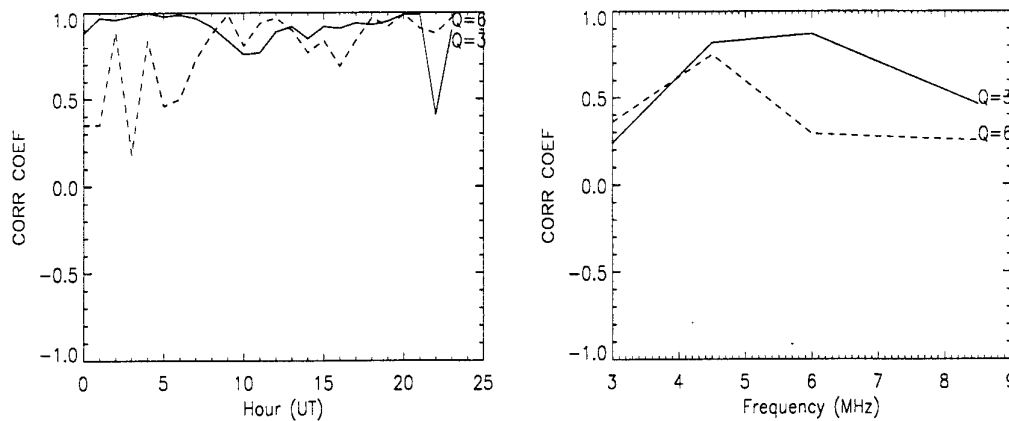
Q=6:

Figure 8.10 *Unmodified prediction above, ICEPAC prediction with both the F & T-model and mode availability included below. Andøya-Alta (285 km), March 1988, SSN=71*

*Figure 8.11   Similarity coefficients (corr coef) between reliability of measured data
and reliability predicted by ICEPAC including both the F&T-model and
mode availability. Andøya-Alta (285 km), March 88*

Q=6 does not show the same remarkably good resemblance to the data (Figure 8.3), but
is nevertheless a large improvement compared to the unmodified prediction. The
similarity coefficient k(96) of all frequencies and hours have increased from 0.54 to 0.78,
an increase of 24 %. The similarity coefficient has also increased for the two lowest
frequencies, but decreased for the two highest frequencies compared with the unmodified
prediction (Figure 6.8). Compared with Figure 8.7 (only F & T-model included), k(24)
for each frequency have decreased. The main improvement for Q=6 has occured for k(4)
for each hour, over all frequencies. This is due to the low reliability now predicted at the
upper frequencies, in much better correspondance with the data.

Since the ionospheric medium is much more variable and difficult to predict under
disturbed conditions, one must expect less similarity between data and predictions than
for quiet conditions.

Including *both* the F & T-model and mode availability has given a large improvement of
predicted reliability. The F & T-model alone (Section 8.1) did not give significant
improvements of the similarity coefficients, only at individual frequencies for Q=6. The
usefulness of the F & T-model should therefore be tested by including mode availability
alone in ICEPAC, without the F & T-model. The similarity coefficients between data and
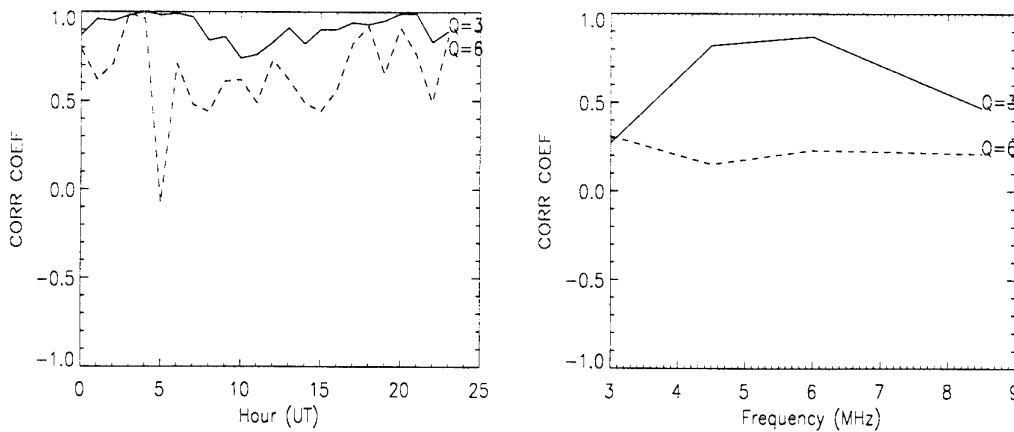predictions including mode availability only, are given in Figure 8.12.

Figure 8.12 *Similarity coefficients between reliability of measured data and reliability predicted by ICEPAC including mode availability only. Andøya-Alta (285 km), March 1988*

For Q=3, mode availability *alone* is the reason for large similarity coefficients. The similarity coefficient over all hours and frequencies is now 0.91, the same as when both F & T and mode availability were included. This is an expected result since the absorption equation used in ICEPAC is an empirical fit to low-latitude data where particle precipitation and auroral absorption is rare. The F & T-model would have little to contribute in these situations, but rather be an alternative way of calculating the absorption.

For Q=6, *both* the F & T-model and mode availability are contributing to the high similarity in Figure 8.11. The total k(96) is now 0.67, an increase from unmodified predictions of 13 %, but a decrease from F & T *and* mode availability included, of 11 %. The coefficients in Figure 8.11 are generally larger than corresponding coefficients in Figure 8.12, except for a few hours. This shows that both the F & T-model and mode availability are necessary in order to improve the prediction of reliability significantly during disturbed conditions. Table 8.1 lists the overall similarity coefficients when the different models are included.

k(96) between:	Q=3	Q=6
data and ICEPAC unmodified	0,71	0,54
data and ICEPAC with F&T included	0,67	0,55
data and ICEPAC with mode avail included	0,91	0,67
data and ICEPAC with F&T and mode avail included	0,91	0,78

Table 8.1 *Similarity coefficients between data and predictions over all frequencies and hours when different models are included in the predictions*

The data (Figure 8.2 and 8.3 and previous plots, Section 6.2) shows clearly that propagation above the MUF is very limited. Based on our data and the comparisons made here between unmodified predictions and predictions including mode availability,

we support those authors that claim that above-the-MUF propagation is overestimated. A much better agreement between data and predictions has been obtained by including mode availability as an independent factor in the reliability calculations.

8.4 The applicability of the model and error sources

ICEPAC and other prediction programmes contain *models* of the ionosphere and of radio propagation, which have limited complexity. For example, ICEPAC does not include multipath fading, Doppler effects and the effect of the Earth's magnetic field on propagation. Nevertheless, ICEPAC is a fairly complex program, but with reasonable computation time. Here we will mention some of the error sources contained in our proposed absorption model calculations, which can either be eliminated through more complex software algorithms, or are inherent in the statistical F & T-model.

In our comparisons between measured data and predictions, we did not thoroughly verify that the input parameters to ICEPAC were correct. Parameters such as noise level at the receiver, antenna gain pattern and radiated power were chosen according to our best guess, but without measurements. These uncertainties may cause discrepancies between data and predictions.

ICEPAC uses the local index Q at the magnetic midnight meridian as a measure of geomagnetic activity, and deduces the global index K_p from it. The formula used in this conversion is criticized by Dandekar (36), and he suggests another conversion formula that gives a smaller Q relative to K_p than the formula used in ICEPAC. Q is still greater than K_p for $K_p \geq 3$. If the suggested formula is more correct than the current formula, then Table 7.1 in Section 7.2 would give a relatively large increase of riometer absorptions for Q=3 and a smaller increase for Q=6. For Q=8 the riometer absorption would decrease. The relative riometer absorption of different hours would not change, and thus not the shape of the surfaces in Figure 7.5. The general level for different values of Q would change slightly.

Table 7.1 in Section 7.2 relates the global parameter K_p to local measurements of riometer absorption in Lavangsdalen. We used one month of data only, so this correlation analysis might be prone to errors. A local geophysical index describes the actual state of the ionosphere at a particular location better than a global index. Correlating the global K_p to local riometer measurements in e.g. Alaska would give a different relationship. It was found in Vondrak et al (72) that conversion of K_p to a local K was necessary in order to model absorption correctly. Thus an important feature of the F & T-model is that knowledge about the local riometer absorption in a particular latitude/longitude sector can be incorporated in propagation predictions for that sector.

Most of the data used in the developement of the mean statistical F & T-model profiles is from Scandinavia. Ranta (22) reports that there is a different observed diurnal variation of riometer absorption in Alaska than at other high latitude longitudinal sectors including Canada. Rapoport (32) also reports differences between longitudinal sectors, but not as fundamental as those mentioned by Ranta. We have not found an explanation in the literature for the different diurnal variation of absorption in Alaska and Europe. If the reason is a different particle spectrum that causes the ionization and the N_e-profiles, the F & T-model electron density profiles would not be applicable in Alaska.

Using the Appleton-Hartree equation for ionospheric loss (Equation 7.6) introduces some errors that have been mentioned in earlier chapters. The error sources are the following:

- Using the Appleton-Hartree equation instead of the generalized magneto-ionic theory described in Section 2.6 introduces errors in the lower part of the D-region for the lowest frequencies. For 2 MHz at an altitude of 60 km the Appleton-Hartree equation overestimates the absorption with an error less than 30 % for the ordinary wave (Barrington and Thrane (21)).

- We have used the longitudinal approximation which means that the direction of propagation is assumed to be along the magnetic field. The longitudinal approximation is considered to be accurate enough for many HF propagation paths (Budden (73)). Geometrical considerations show that the error is minor for our short, high-latitude path, and of no importance in these overall simplified calculations of propagation.

Some errors are due to the implementation of the Appleton-Hartree equation on the computer, and can be improved by more sophisticated software algorithms:

- We are using the N_e-profile at the midpoint of the path, or in general at the locations along the path where reflections are expected. However, the absorption occurs where the ray traverses the D-region, so ideally two N_e-profiles should be used, one close to the transmitter and the other one closer to the receiver. The short path used in our example lies approximately in the east-west direction, and we assume that the auroral events extend along the raypath and do not introduce significant errors.

- Ionospheric absorption was calculated by integrating Equation 7.6 over the height interval in which the F & T-model is defined. The non-deviative absorption does however, not cease abruptly at e.g. 120 km, but decreases smoothly over a large height interval. In Section 7.7 we estimated the maximum error in our calculations due to the discontinuity between the F & T-profile and the ICED-profile.

One error is inherent in the F & T-model:

- For the transition between day and night time there is a non-realistic abrupt increase/decrease in absorption for small Q-values. This discontinuity should be investigated. The error seen in Figure 7.5 for Q=0 is about 4 dB.

Eliminating the above-the-MUF propagation may introduce a too pessimistic prediction of reliability. This argument was mentioned by, but not supported by Argo (53). Our comparisons support Argo; the predictions including the above-the-MUF propagation are too optimistic. Defining the circuit reliability as $R_c=q_{MRM} \cdot P_{a,...,z}$ is consistent with what is measured on a real channel: For a narrowband signal as in our experiment, each databit has a fairly long time-duration, and power propagated along different paths is received within the data bit period (assuming no frequency-selective fading). A *power sum* of modes is detected, and BER determined. Most of the time, *one* mode is dominating and transferring most of the power.

The approach of using the electron density profile (as suggested in this work) to calculate both the ionospheric absorption and the mode availability can be used instead of the semi-empirical formula for absorption and a-t-M propagation in ICEPAC. Then the uncertainty of the ICEPAC empirical data and the definition of the signal strength mentioned in Section 4.3.2 can be avoided.

9 CONCLUSIONS

Experience has shown that HF communication at high latitudes is less reliable and predictable than at lower latitudes (Thrane (74)). The high-latitude ionosphere is a very dynamic medium due to precipitation of charged particles from the solar wind and the interaction of the interplanetary magnetic field with the Earth's magnetic field. Lower latitudes are screened from these effects by the dipole magnetic field. HF radio waves travelling through the high latitude ionosphere are subject to multipath problems, Doppler shift/spread and severe absorption that all vary with time of day, frequency, geomagnetic activity and solar activity. It is important to know and understand the fundamental limitations of the ionospheric medium in order to choose appropriate signal processing techniques for HF. Some of the devastating effects can be counteracted by appropriate signal processing techniques, such as modulation, coding and diversity. For the HF operator it is important to choose a suitable frequency at all times, and to know the probability of achieving a connection.

Prediction programmes at HF are based on theoretical knowledge of radio wave propagation in the ionosphere and on empirical data. They serve as tools for systems design, frequency management and daily operations of communication systems. At high-latitudes, systematic observations of HF communication have been scarce and the performance of prediction programmes poor (Thrane (75)).

The objective of this work has been to investigate HF propagation characteristics at high latitudes, and to compare measurements with the predictions from the programme ICEPAC.

A database was established in the period 1987 to 1992 containing data from one auroral, 285 km path and one sub-auroral/mid-latitude, 1280 km path. We measured the BER of the channel by transmitting a standard message, and derived the statistical reliability of the channel. The time delays of the signals were also measured and virtual heights of reflection derived, assuming a one-hop path. The database describes the effects of seasonal variations and different degrees of geophysical disturbances.

The observations were compared with predicted circuit reliability and with predicted virtual height of reflection for the most reliable propagating mode. The most important conclusions are as follows:

For the short auroral path:

• The observed reliabilities are in general much smaller than the predicted reliabilities. The reason is that auroral absorption and ionospheric dynamics have not been properly taken into account in ICEPAC.

- During periods of high geomagnetic activity, the observations show a marked decrease of reliability in the morning due to absorption caused by particle precipitation. This observed diurnal variation is not predicted by ICEPAC.

- ICEPAC predicts that reliable propagation channels exist at frequencies well above the predicted MUF. The propagation at these frequencies is supposed to be caused by scatter from inhomogeneities etc., in contrast to reflection from ordinary layers of electron density. Propagation above the MUF is not observed in our data sets.

For the longer mid-latitude/sub-auroral path:

- The data show both high-latitude and mid-latitude characteristics. The observed high-latitude characteristics are low reliability for disturbed conditions and the presence of some auroral-E reflections at night. However, the characteristic time variation of auroral absorption with high absorption in the morning is *not* observed.

- In spite of the observed auroral characteristics, ICEPAC classifies this path as a mid-latitude path. Unexpectedly, the discrepancy between data and predictions is larger for this path than for the auroral path.

At high-latitudes, the prediction of signal strength and thus reliability of the channel was shown to be particularly unsatisfactory. At the low frequencies, the level of, and daily variation of absorption is not accurately predicted, and at the high frequencies above the MUF, the predicted probability of propagation is too optimistic. We suggest two improvements to the predictions:

- To solve the problem of incorrect prediction of absorption, we have incorporated the high-latitude D-region model (F & T-model) developed by M. Friedrich and K. Torkar, and integrated the non-deviative absorption through the D-region model using the Appleton-Hartree equation.

- To solve the problem of large relibility at frequencies above the MUF, we have implemented a method of calculating reliability that uses explicitly the probability of a mode being present. This method has been used in the earliest versions of ICEPAC.

Our comparisons with the data show a significant improvement in the prediction of reliability. The F & T-model gives small reliabilities for the lowest frequencies in good agreement with the measured characteristics. The decrease of reliability is particularly large for the morning hours during disturbed conditions, as also observed in the data. The explicit use of mode availability reduces the predicted reliability for frequencies close to the MUF considerably, in agreement with observations. This reduction is independent of geomagnetic activity. The two suggested modifications have not lead to any improvement of predicted virtual height of reflection.

The overall improvement of predicted reliability achieved by these modifications for the selected month is 20 % for quiet conditions and 24 % for disturbed conditions. We believe that incorporating a D-region model and integrating the ionospheric absorption through a realistic N_e-profile is fundamentally a more correct way of predicting ionospheric absorption. This is particularly important at high latitudes where the D-region N_e-densities vary with the geomagnetic activity by orders of magnitude, and the absorption can be large. In addition, the large existing database of riometer absorption from high latitudes can be used to predict the correct diurnal variation of absorption.

We also argue, based on our data, that above-the-MUF propagation is over-estimated in ICEPAC. The specular reflections from ionospheric layers, not other propagation mechanisms above the MUF, dominate the propagation at the observed maximum frequency on this path.

Our measurements were conducted during years around sunspot maximum and are thus expected to show a worst case situation with high LUF. However, the MUF is also larger for high sunspot numbers, so the range of usable frequencies are shifted towards higher frequencies.

Future work in this field should include:

- The F & T-model should be further developed and tested against more data sets including different seasons and sunspot numbers.

- The F & T-model should be implemented properly in the software, making the complete electron density profile continous, etc.

- Observed longitudinal differences of absorption should be investigated. If the cause of the differences is a different ionizing spectrum, then the F & T-model may not be applicable to all longitudinal sectors.

- Much work remains to incorporate existing high-latitude absorption databases in the prediction programme. A large global network of riometers exist that has measured absorption for many years. Using the F & T-model and an appropriate absorption equation will allow these riometer data to be incorporated in the prediction of absorption. The riometer data from different databases must be calibrated and sufficient spatial resolution of the absorption characteristics must be determined.

Modelling of the D-region is not an easy task (see for example Thrane et al (28)). High-latitude models other than the F & T-model also exist, such as CCIR Supplement to Report 252-2 (55) which is based on the work by Foppiano (76), Vondrak et al (72) and Kirkwood and Collins (77). A comparison between the different high-latitude models should also be done in the future.

Including the F & T-absorption model for high-latitudes makes the prediction programme more complex. This work has revealed that absorption calculations for high-latitudes in ICEPAC are inconsistent and incorrect, resulting in variations of absorption of a hundred dB from hour to hour. We strongly recommend that an improved high-latitude model of absorption is incorporated in prediction programmes.

References

(1) Stewart F., G. Hand, Institute of Telecommunications Sciences, Boulder, Colorado, USA -private communication 1991-1994.

(2) Teters L.R., J.L. Lloyd, G.W. Haydon, D.L. Lucas (1983): Estimating the performance of telecommunication systems using the ionospheric transmission channel, *NTIA Rep.,* 83-127, National Telecommunications and Information Administration, Boulder, Colorado.

(3) Jodalen V., E.V. Thrane (1991): A study of the high latitude ionosphere using a digital spread spectrum ionospheric sounder, *IEE Conference Publication,* 339, Fifth Int. Conf. on HF Radio Systems and Techniques, Edinburgh.

(4) Thrane E. V., V. Jodalen, F Stewart, D Saleem, J Katan (1994): Study of measured and predicted reliability of the ionospheric HF communication channel at high latitudes, *Radio Science,* 29, 5, pp 1293-1309.

(5) Jodalen V., E.V. Thrane (1994): A study of the relation between ionospheric absorption and predicted HF propagation parameters at high latitudes, *IEE Conference Publication,* 392, Sixth Int. Conf. on HF Radio Systems and Techniques, York.

(6) Jodalen V., E. V. Thrane (1995): An improved model of ionospheric absorption at HF high latitude paths, *AGARD Conference Proceedings,* AGARD Conference on Digital Communications and Propagation, Athens, Greece.

(7) Friedrich M., K. M. Torkar (1983): High-latitude plasma densities and their relation to riometer absorption, *JATP,* 45, 2/3, pp 127-135.

(8) Davies K. (1989): Ionospheric Radio, *Peter Peregrinus Ltd.,* Stevenage, UK.

(9) Goodman J. M. (1992): HF Communications, Science and Technology, *Van Nostrand Reinhold,* New York, USA.

(10) Halcrow B. W., J. S. Nisbet (1977): A model of F_2 peak electron densities in the main trough region of the ionosphere, *Radio Science,* 12, 5, pp 815-820.

(11) Rycroft M. J., J. O. Thomas (1979): The magnetospheric Plasmapause and the electron density trough at the Alouette I orbit, *Planet. Space Sci.,* 18, (1), pp 65-80.

(12) Ratcliffe J. A., (1959): The magneto-ionic theory and its applications to the ionosphere, *Cambridge University Press,* London, UK.

(13) Appleton E. V., J. A. Ratcliffe (1927): On the Nature of Wireless Signal Variations, *Proc of the Royal Society (A),* 115, p 291.

(14) Piggott W. R., W. J. G. Beynon, G. M. Brown, C. G. Little (1957): The measurement of ionospheric absorption, *Annals of the IGY*, Vol III, Part II, p 173.

(15) Phelps A.V., J. L. Pack (1961): *Phys Rev Letters*, 6, p 111.

(16) Sen H. K., A. A. Wyller (1960): On the generalizations of the Appleton- Hartree magnetoionic formulas, *J Geophys Res*, 65, p 3931.

(17) Thrane E. V., W. R. Piggott (1966): The collision frequency in the E- and D-region of the ionosphere, *JATP*, 28, pp 721-737.

(18) Thrane E.V. (1966): Experimental studies of the structure of the ionospheric D-region, *NDRE Report No 54*, Forsvarets forskningsinstitutt.

(19) Molmud P. (1959): *Phys Rev*, 114, p 29.

(20) Rees D., J. J. Barnett, K. Labitzke (1990): COSPAR International Reference Atmosphere II, Middle Atmospheric Models, *Adv Space Res*, 10, (12).

(21) Barrington R. E., E. V. Thrane (1962): The determination of D-region electron densities from observations of cross modulations, *JATP*, 24, pp 31-42.

(22) Ranta H. (1978): Riometer measurements of ionospheric absorption at high latitudes, *Report No. 34*, Sodankyla Geophysical Observatory, Sodankyla, Finland.

(23) Thrane, E. V. (1981): The physics of radio wave absorption, *AGARD Conf Proc*, No 295, Ed E. Schmerling, pp 10-1 to 10-15, AGARD, Paris, France.

(24) George P. L. (1971): The calculation of ionospheric absorption in HF radio propagation predictions, *WRE-Technical Note-A207(AP)*, Department of Supply, Australian Defence Scientific Service Weapons Research Establishment, Salisbury, South Australia.

(25) Piggott W. R. (1953): The reflection and absorption of radio waves in the ionosphere, *Proc IEE*, 100, Part III, pp 61-72.

(26) Thrane E. V. (1972): On the diurnal and seasonal variation of the D-and E-regions above Kjeller, *Proceedings of NATO ADV Study Inst*, Ed K Folkestad, Magnetosphere-Ionosphere Interactions, Oslo University Press, pp 29-38.

(27) *Journal of Atmospheric and Terrestrial Physics* (1979), 41, special issue.

(28) Thrane E.V. et al (1979): D-region predictions, a working group report, *Solar-Terrestrial Prediction Proceedings*, Ed R. F. Donnelly, Vol II, pp 573-598. US Gvt Printing Office Stock no 003-017-00471-6.

(29) Thomas L. (1979): A study of the enhanced electron concentrations in the mid-latitude D-region on winter days in terms of the positive ion chemistry, *J Geomag Geoelectr,* 31, pp 567-583.

(30) Hartz T. R. (1971): The Radiating Atmosphere, Ed. B. M. McCormac, Reidel Dordrecht, p 225.

(31) Holt O., B. Landmark, F. Lied (1961): Analysis of riometer observations obtained during polar radio blackouts, *JATP,* 23, p 229.

(32) Rapoport Z. Ts. (1979): Comparison of the variability of auroral radio wave absorption in the ionosphere at Loparskaya and College, *Geomagn. Aeron.,* 10, p 58.

(33) Egeland A., Ø. Holter, A. Omholt (1973): Cosmical Geophysics, Universitetsforlaget.

(34) Jursa A. S. (1985): Handbook of geophysics and the space environment, Air Force Geophysics Laboratory, Air Force Systems Command, US Air Force, US.

(35) Hardy D. A., -private communications.

(36) Dandekar B. S. (1993): Determination of the auroral oval Q index from the air weather service K index, *PL-TR-93-2267 Environmental Research papers, No. 1136,* Phillips Laboratory, Air Force Material Command, Hanscom Air Force Base, MA, USA.

(37) Feldstein Y. I., G. V. Starkov (1967): Dynamics of Auroral Belt and Polar Geomagnetic Disturbances, *Planet Space Sci,* 15, p 209.

(38) Starkov G. V. (1969): Analytical representation of the equatorial boundary of the oval auroral zone, *Geomagn Aeron,* 9, p 614.

(39) Reilly A. E. (1978): The Geomagnetic Index Q - Its Persistence, Predictability, and Other Pertinent Properties, *AFGL-TR-78-0223, Environmental Research Papers no 640,* Air Force Geophysics Laboratory, Hanscom AFB, Massachusetts, USA.

(40) Dandekar B. S. (1979): Magnetic disturbance statistics from a single station q index applied to an actual OTH-B radar situation, *AFGL-TR-79-0296, Environmental Research Papers,* No 687, Air Force Geophysics Laboratory, Hanscom AFB, Massachusetts, USA.

(41) CCIR (1979): CCIR Interim Method for Estimating Skywave Field Strength and Transmission Loss at Frequencies Between the Approximate limits of 2 and 30

MHz, *Report 252-2* in *Recommendations and Reports of the CCIR: Propagation in Ionized Media,* Vol VI, New Delhi plenary, ITU, Geneva, Switzerland.

(42) Davies R. M., N. L. Groome, Variations of the 3000 km MUF in time and space, - private communications.

(43) CCIR (1986): Man-Made Noise, *Report 258-4, Reports and Recommendations of the CCIR: Propagation in Ionized Media,* Vol VI, Dubrovnik Plenary, ITU, Geneva, Switzerland.

(44) CCIR, Characterisitics and applications of atmospheric radio noise data, *Report 322-3,* ITU, Geneva, Switzerland.

(45) Laitinen P. O., G. W. Haydon (1959): Analysis and prediction of sky-wave field intensities in the high frequency band, *Tech Rept,* 9, *Revised RPN 203,* U.S Army Signal Radio Propagation Agency, USA.

(46) Lucas D. L., G. W. Haydon (1966): Predicting statistical performance indexes for high frequency ionospheric telecommunications systems, *ESSA Tech Rept IER 1-ITSA 1,* NTIA, ITS, Boulder, USA.

(47) Philips M. L. (1962): Evaluation of effective E_s reflectivity of obscuration because of E_s ionization, *External Tech Memo,* 14, Electro-Physics Labs.

(48) Phillips M. L., W. Abel, F-layer transmission on frequencies above the conventionally calculated MUF, *Project Earmuff, Final Report,* U.S. Army Signal Corps, Contract DA-36-029-SC-72802, USA Signal R&D Labs, Ft. Monmouth, New Jersey, USA.

(49) Wheeler J. L. (1966): Transmission loss for ionospheric propagation above the standard MUF, *Radio Science,* 1, 11, pp 1303-1308.

(50) Bradley P. A., C. Bedford (1976): Prediction of HF circuit availability, *Electronics Letters,* 12, pp 32-33.

(51) Bradley P. A. (1989): Above-the-MUF loss, *IEE Conf Pub* No 301, Part 2, 6th Int Conf on Antennas and Propagation, pp 257-262.

(52) Bradley P. A., R. Y. Liu, M. Lockwood, M. I. Dick (1982): Above-the-MUF Loss, *CCIR XVIth Plenary Assembly,* Study group 6, IWP 6/1 Doc 209, IWP 6/12 Doc.

(53) Argo P. (1993): Reliability Calculations and Above-the-MUF propagation, *Proceedings of the Ionospheric Effects Symposium, IES-93,* Washington, USA.

(54) Hagn G., A.J. Gibson, P.A. Bradley (1993): Propagation on frequencies above the basic maximum usable frequency, *Proceedings of the Ionospheric Effects Symposium, IES-93,* Washington, USA.

(55) CCIR (1982): Supplement to Report 252-2: Second CCIR Computer-Based Interim Method for Estimating Skywave Field Strength and Transmission Loss at Frequencies Between 2 and 30 MHz, ITU, Geneva, Switzerland.

(56) CCIR (1986): Propagation Prediction Methods for High Frequency Broadcasting, *Report 894-1, Recommendations and Reports of the CCIR: Propagation in Ionized Media,* Vol VI, XVIth Plenary held in Dubrovnik, ITU, Geneva, Switzerland.

(57) Tascione T.F., H.W. Kroehl, R. Creiger, J.W. Freeman Jr., R.A. Wolf, R.W. Spiro, R.V. Hilmer, J.W. Shade, B.A. Hausman (1988): New ionospheric and magnetospheric specification models, *Radio Science,* 23, pp 211-222.

(58) Skaug R. (1982): An experiment with spread spectrum modulation on an HF channel, *IEE Conf Pub,* No 206, Second Conference on HF Communication Systems and Techniques, IEE, London, UK.

(59) Thrane E. V. (1979): Results of transmission tests in Norway using high frequency radio waves reflected from the ionosphere, *Intern Rapport E-303,* Norwegian Defence Research Establishment, Kjeller, Norway.

(60) Thrane E. V., P. A. Bradley (1981): High frequency sky-wave prediction methods and observational circuits, *IEE Conf Proc,* Second Int Conf on Antennas and Propagation, pp 258-262, York, UK.

(61) Jodalen V., E.V. Thrane, I. Koltveit, T. Hellum (1991): Ionospheric HF radio propagation at high latitudes using conventional and spread spectrum modulation, *FFI/Rap.* 91/7003, Forsvarets forskningsinstitutt, Kjeller, Norway.

(62) Sklar B. (1988): Digital Communications, *Prentice-Hall International Editions,* New Jersey, USA.

(63) Clutterbuck C. (1995): Defence Resarch Agency, Malvern, UK, -private communication.

(64) Friedrich M., K. Torkar (1992): An empirical model of the nonauroral D region, *Radio Science,* 27, 6, pp 945-953.

(65) Wagner L.S., J. A. Goldstein (1995): Channel spread parameters for the high-latitude near-vertical-incidence skywave HF channel: Correlation with geomagnetic activity, *NRL/FR/5550-95-9772,* Naval Research Laboratory, Washington DC, USA.

(66) Basler R. P., P. B. Bentley, R. T. Price, R. T. Tsunoda, T. L. Wong (1988): Ionospheric distortion of HF signals, *Radio Sci,* 23, (4), pp 569-579.

(67) Davies N. C., P. S. Cannon (1995): DAMSON- A system to measure multipath dispersion, Doppler spread and Doppler shift on multi-mechanism communications channels, *Proc of AGARD Symp* on Multiple mechanism propagation paths (MMPPs): Their characterisation and influence on system design, CP-543, Rotterdam, Holland.

(68) Baron M. (1986): EISCAT progress 1983-1985, *JATP,* 48, p 767.

(69) Friedrich M., K.M. Torkar (1995): Typical behaviour of the high latitude lower ionosphere, *Adv. Space Res.* 16, 1, pp 73-81.

(70) IUGG, Association of Geomagnetism and Aeronomy, International Service of Geomagnetic Indices, Editor: Institut fur Geophysik, Gottingen, Germany.

(71) Stauning P., S. Henriksen (1988): Lavangsdalen Riometer Absorption Data, *Technical Report,* 89-28, Danish Meteorological Institute, Copenhagen, Denmark.

(72) Vondrak R. R., G. Smith, V. E. Hatfield, R. T. Tsunoda, V. R. Frank, P. D. Perreault (1977): Chatanika model of the high latitude ionosphere for application to HF propagation prediction, *SRI Report* on Contract F19628-77-c-0102.

(73) Budden K. G. (1961): Radio waves in the ionosphere, Cambridge University Press.

(74) Thrane E. V. (1986): Problems in HF propagation, *AGARD Lecture Series* No. 145, AGARD, Paris.

(75) Thrane E. V. (1986): State of the art of modelling and prediction in HF propagation, *AGARD Lecture Series* No. 145, AGARD, Paris.

(76) Foppiano A. J. (1975): A new method for predicting the auroral absorption of HF sky waves, *CCIR Interim Working Party, Document 3.*

(77) Kirkwood S., P. N. Collins (1991): The high latitude lower ionosphere observed by EISCAT, *Adv. Space Res.,* 11, 10, pp 109-112.

APPENDIX

A   THE DATABASE OF THE HF TESTS

FINAL DATABASE, HF TEST CIRCUIT

	JAN	FEB	MAR	APR	MAY	JUNE	JULY	AUG	SEPT	OCT	NOV	DEC
1987	30-31							1-25	1-22, 27-28	3,7, 10-18,21 23-26	1-16	1-6,8, 10-11,13,
1988			2-24, 28-31	1-17, 21-30,	1-5, 15-16,	9-28, 30	1,4-5, 8-10,13-22 25-27,29-31	1-2, 8-9 11-31		1,3-30	1-3, 7-14,23, 27-30	1-4, 13-14
1989	9						7-28, 31	1-4,9 15,24-31	1-7 11-28			
1990		1-19	5-13, 15-31	1-18, 20-30	1-21			15-24, 27-31	1-29	19-27	2-5, 8, 12,15-30	3-24
1991					4-9 15-31	13-30	1-31	1-20 27-31	1-4			
1992		1-29	1-31	1-21 24-30	1-7 21-31	1-30						

(Arrows in JUNE/JULY area: Short path ↓ / Long path ↑)

APPENDIX

B   DATA FROM THE LONG PATH

January/February 1990

This winter period consisted of 17 quiet days and 22 disturbed days.

<u>Virtual height.</u>
The virtual height of reflection is shown in Figure A1. Four frequencies within the HF band are selected for display from the set of nine measurement frequencies.

The reflection pattern is very similar for quiet and disturbed conditions. We nevertheless see slightly larger spread of reflection heights around noon for the disturbed period. There are E-layer reflections from an altitude of about 150 km at night. It is impossible to say whether the observations are sporadic-E or auroral E-layer reflections. The interpretation of a virtual height of 285 km or more is ambiguous. The propagating mode may also be a two-hop mode with a different virtual height.

The predictions are almost identical for Q=3 and Q=6. The agreement between data and predictions is very good for the hours around noon, except for the frequency 19 MHz where the virtual height is predicted 50 km too high. ICEPAC predicts sporadic-E at night at a fixed altitude of 110 km, 40 km lower than the observed E-layer reflections.

<u>Reliability.</u>
Figure A2 and A3 show the reliability of data and predicted reliability for the two periods. The reliability of data is largest around noon, and larger for the quiet period than for the disturbed period. The observed MUF is about 19 MHz around noon.

The predictions of reliability for the quiet and disturbed periods are almost identical and too optimistic, as for the short path. For hours around noon at frequencies 14-17 MHz, the reliability drops to very small values, and then rises again to 30 % for 19 MHz. This is caused by negative antenna gains for these frequencies and is not a propagation phenomenon. The predicted and observed MUFs agree well. The prediction of reliability at night is strongly over-estimated; at the lowest frequencies up to 100 % reliability is predicted.

<u>Similarity coefficients.</u>
The overall similarity coefficients between the predictions of reliability and data are extremely low for this data set; 0.18 for Q=3 and 0.08 for Q=6. k(9) for each hour over all frequencies are smaller than those measured on the short path, whereas k(24) for each frequency over all hours are in general larger. Similarity coefficients for Q=3 and Q=6 are similar (Figure A4).

150
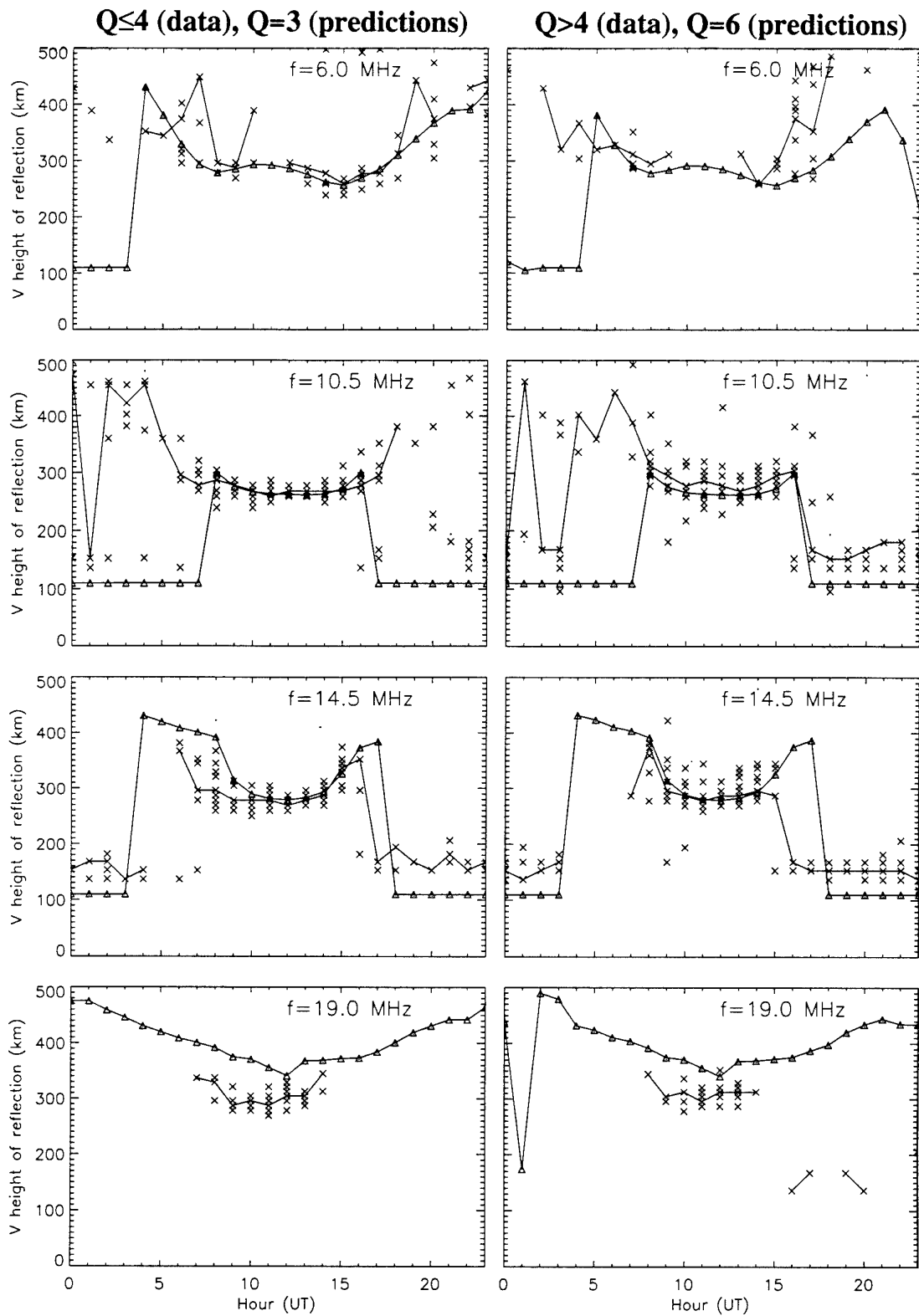
Figure A1   Virtual height of reflection, Kløfta-Alta (1230 km), January/February 1990.
Median of data drawn as a continous line. Small dots indicate
multipath. Predicted virtual height shown as triangles. SSN=151

Q≤4:
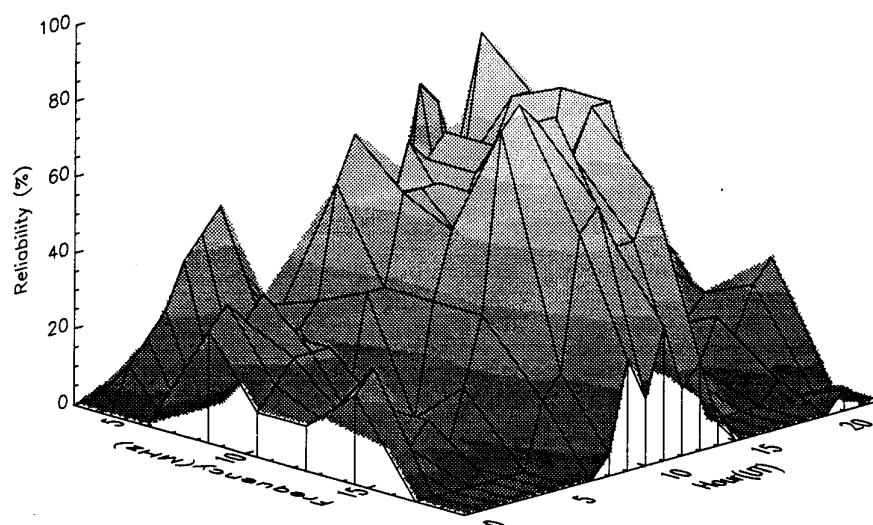
Q=3:
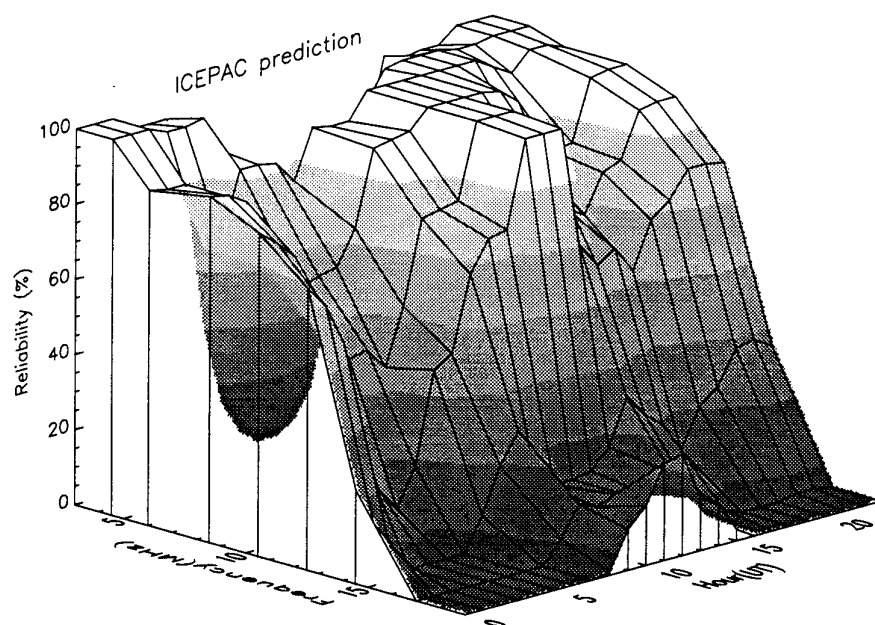
Figure A2   Reliability of data for January/February 1990 above, prediction for
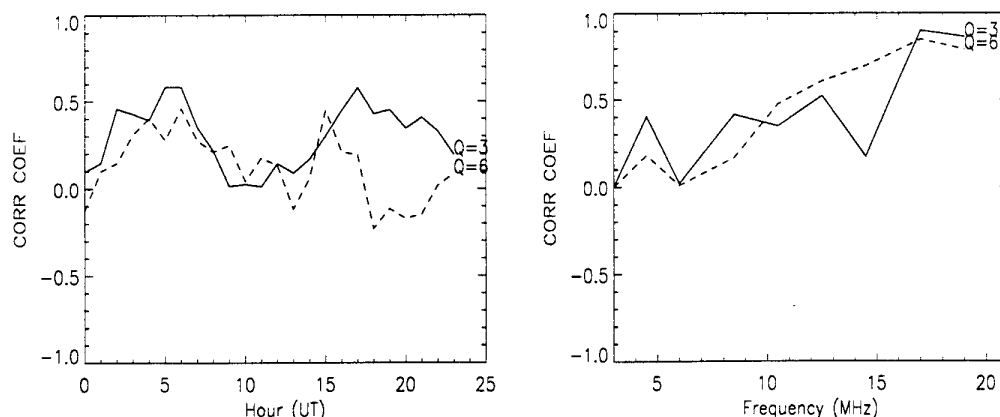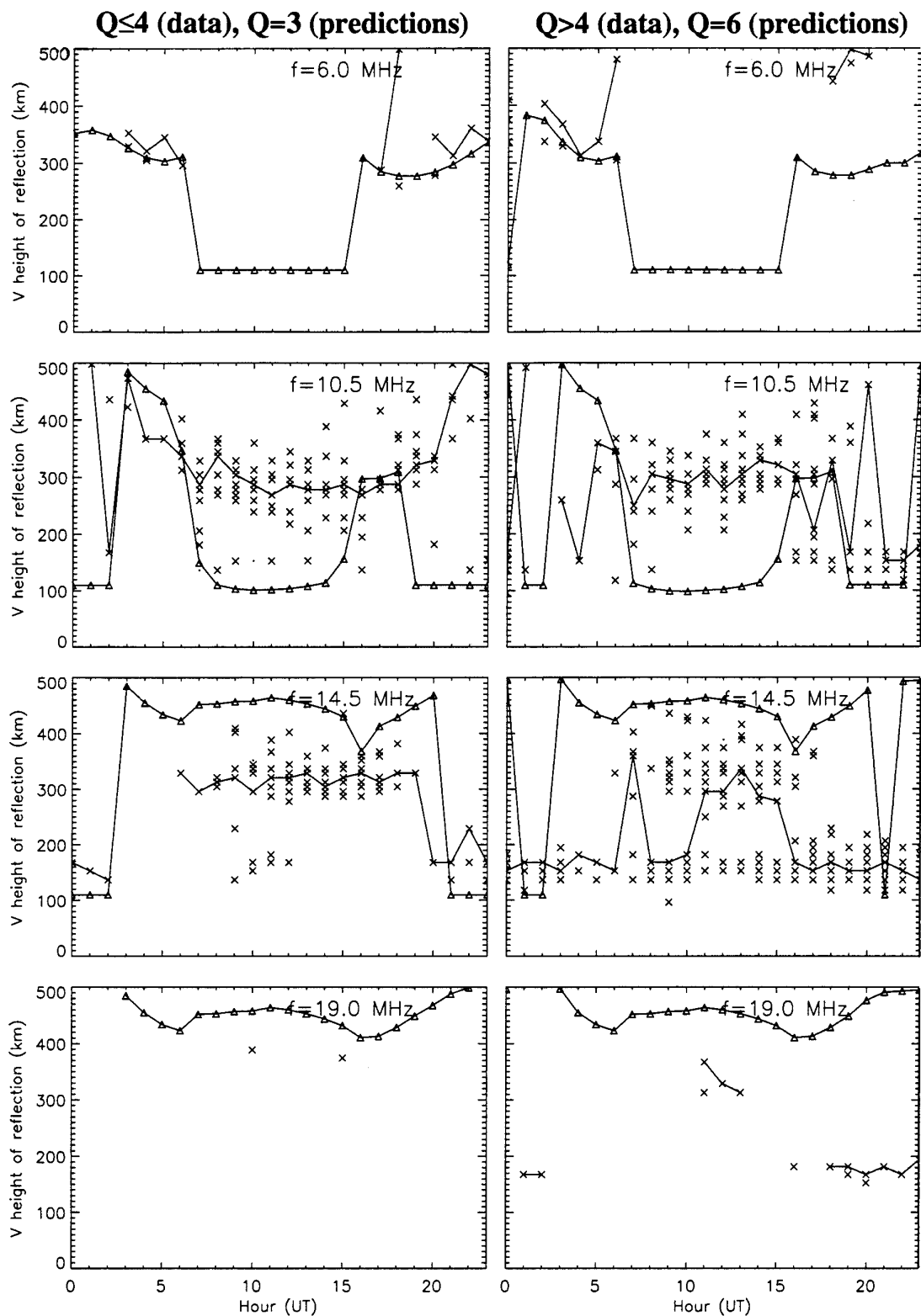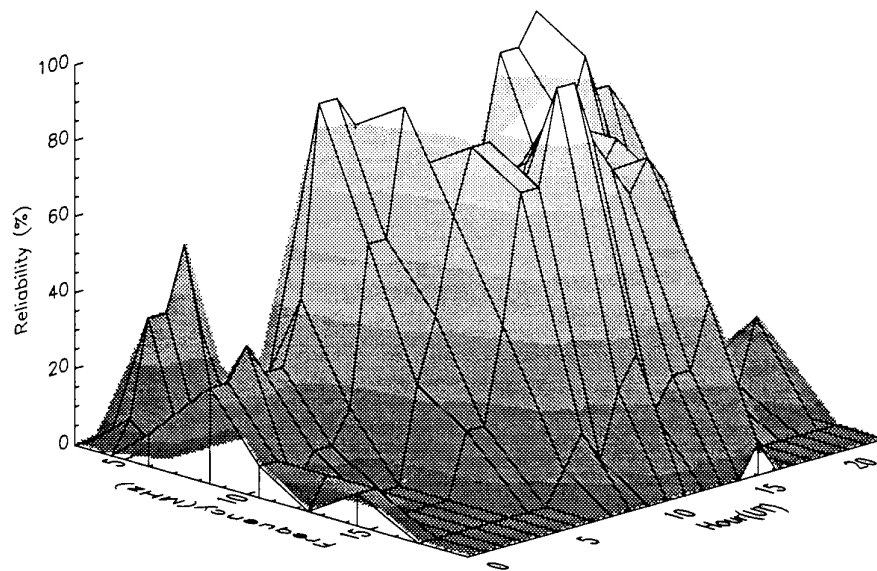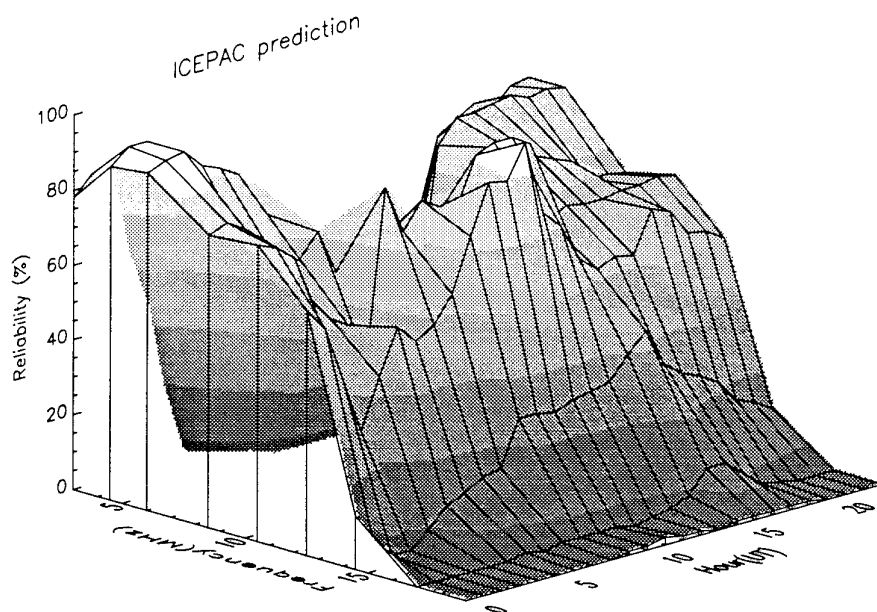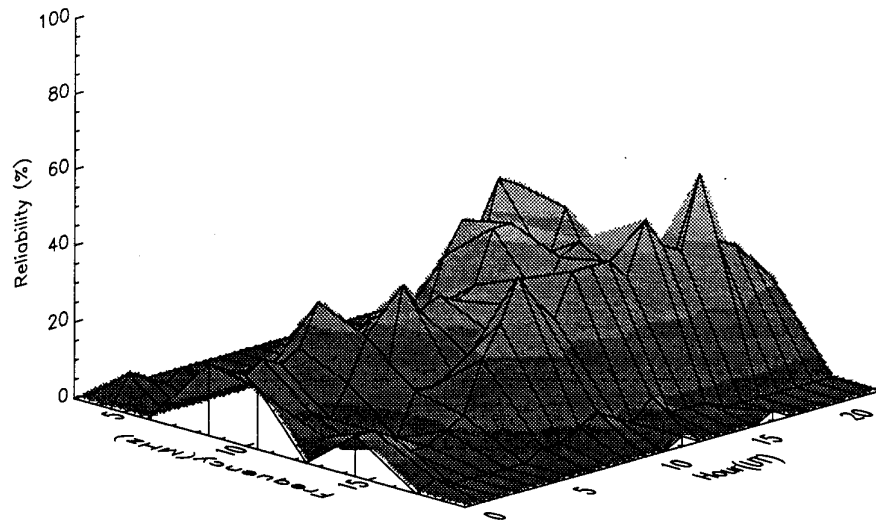*January below (SSN=151). Kløfta-Alta (1230 km)*
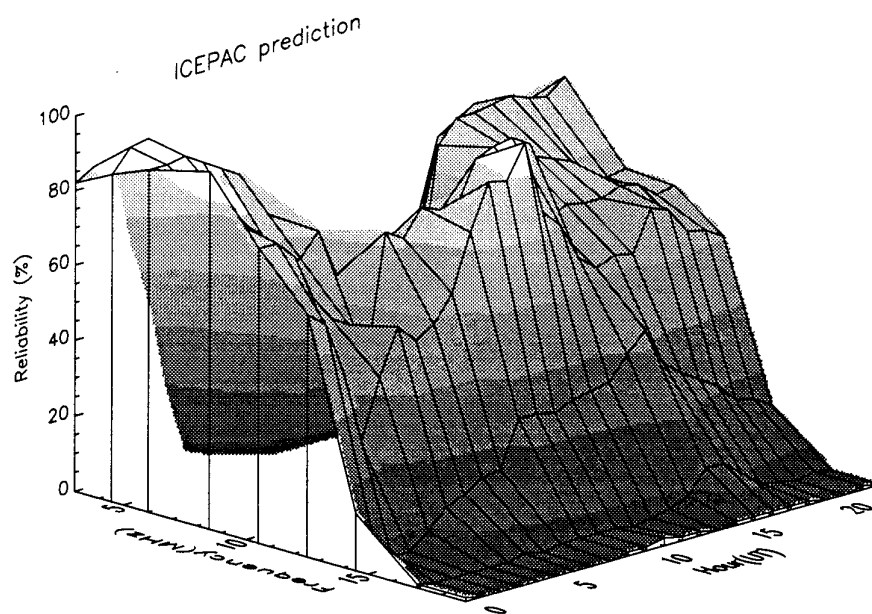
Q>4:
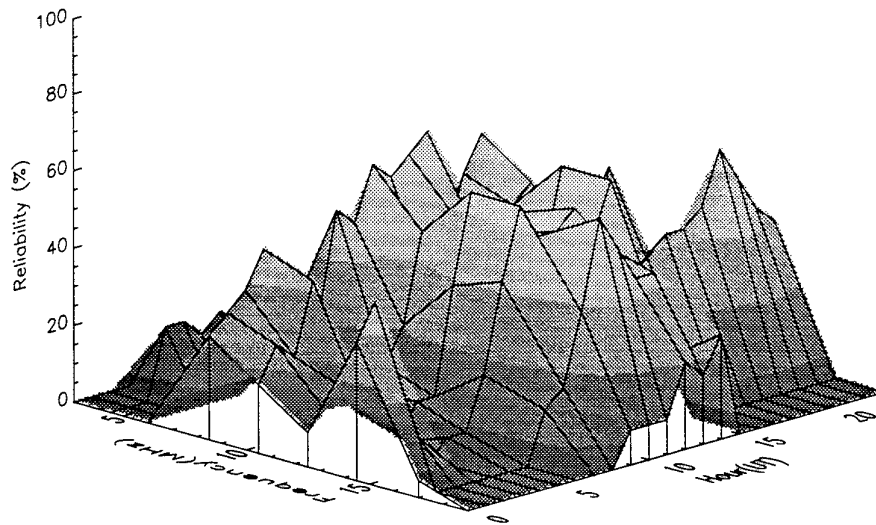
Q=6:
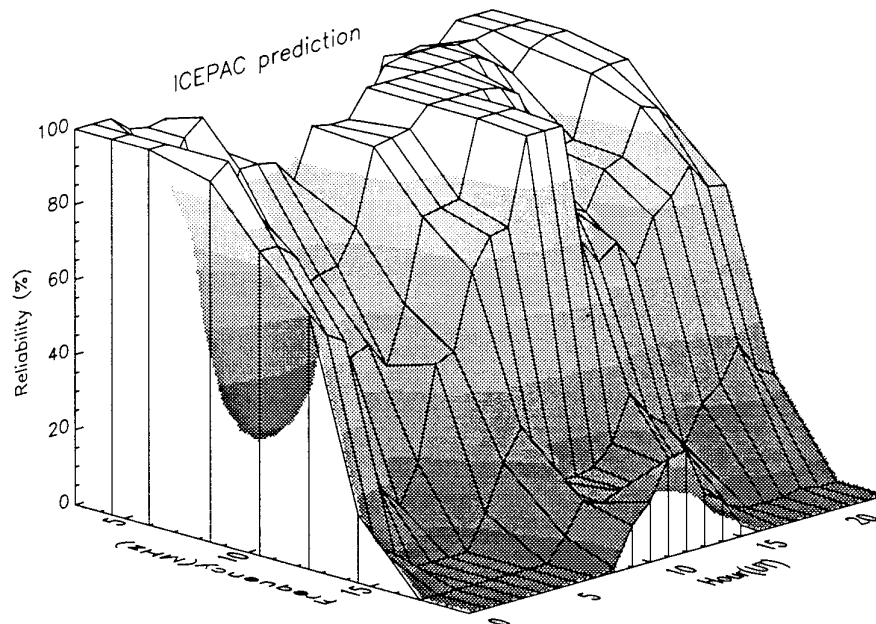
Figure A3   Reliability of data for January/February 1990 above, prediction for January below (SSN=151). Kløfta-Alta (1230 km)

*Figure A4 Similarity coefficients (corr coef) between reliability of measured data and
reliability predicted by ICEPAC. Kløfta-Alta (1230 km), January/February
1990, SSN=151*

March/April 1990

The quiet period consisted of 12 days and the disturbed period of 37 days.

Virtual height.
Virtual heights are shown in Figure A5. The reflection patterns for the two periods are
very similar, but more E-layer reflections are observed at f=14.5 MHz for the disturbed
period.

Predictions of virtual height are again almost equal for Q=3 and Q=6. ICEPAC predicts
E and E_s reflections around noon for frequencies up to and including 10.5 MHz. The
observations show only F-layer reflections for these hours and frequencies. At f=14.5
MHz the F_2-reflections are predicted 100 km too high.

Reliability.
Reliabilities derived from data and predictions are shown in Figure A6 and A7. The
reliabilities from the data for the disturbed period are smaller than for the quiet period.
Reliability is particularly low at night. The maximum usable frequency for quiet
conditions is 17 MHz around noon.

Predicted reliability is overestimated at night for both Q=3 and Q=6, in particular at the
lowest frequencies.

Similarity coefficients.
The overall similarity coefficients for this data set are 0.47 for Q=3 and 0.34 for Q=6.
Figure A8 shows the similarity coefficients k(9) and k(24). k(9) is small for the hours

around midnight, reflecting the large difference between data and predictions. The similarity coefficients for each frequency are equal to or larger than corresponding similarity coefficients for the short path.

Q≤4 (data), Q=3 (predictions)   Q>4 (data), Q=6 (predictions)

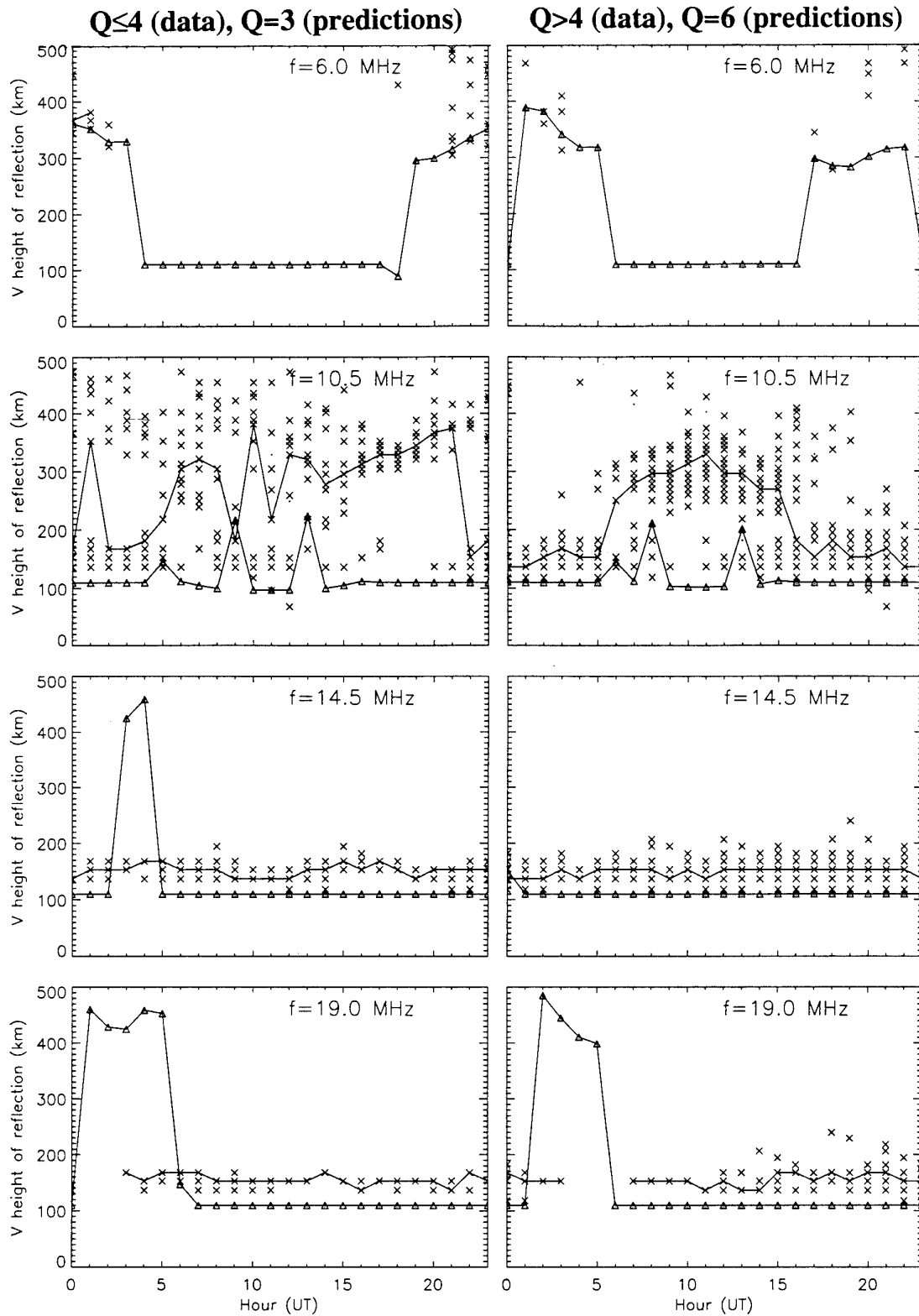*Figure A5   Virtual height of reflection, Kløfta-Alta (1230 km), March/April 1990.*
Median of data drawn as a continous line. Small dots indicate multipath.
Predicted virtual height shown as triangles. SSN=152

Q≤4:

Q=3:

*Figure A6   Reliability of data for March/April 1990 above, prediction for March below
(SSN=152). Kløfta-Alta (1230 km)*

Q>4:

Q=6:

*Figure A7   Reliability of data for March/April 1990 above, prediction for March below
(SSN=152). Kløfta-Alta (1230 km)*
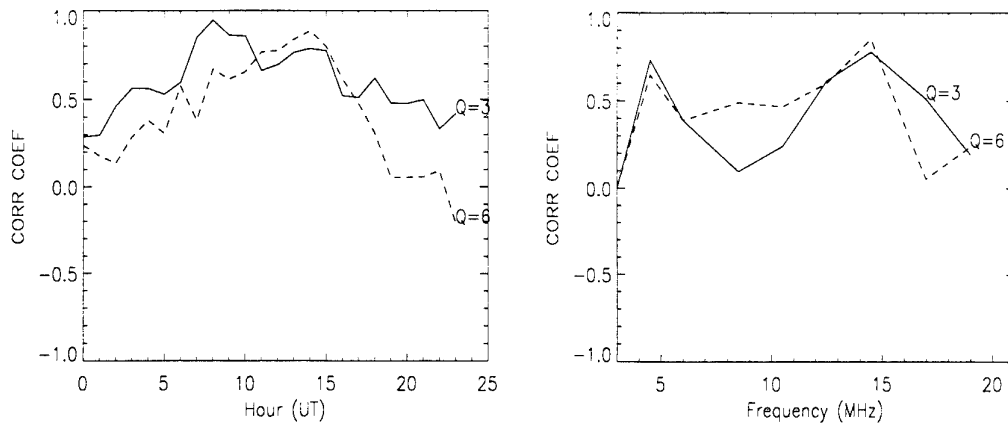
Figure A8 *Similarity coefficients (corr coef) between reliability of measured data and reliability predicted by ICEPAC. Kløfta-Alta (1230 km), March/April 1990, SSN=152*

June/July/August 1991

We have used 14 days of measurements for the quiet period and 44 days for the disturbed period.

Virtual height.
Virtual height of reflection is plotted in Figure A9. E or E_s-reflections dominate the reflection pattern for frequencies above 10.5 MHz. F_2-reflections occur at 10.5 MHz together with E or E_s reflections, but F_2 echoes disappear at higher frequencies, indicating that a dense E-layer exists throughout the day. At 10.5 MHz, F_2-reflections exist at night for quiet conditions but not for disturbed conditions. This can be explained by a denser auroral E for disturbed conditions.

Predictions are again similar for Q=3 and Q=6, predicting sporadic-E reflections at all frequencies. ICEPAC fails to predict the more important F_2-reflections around noon at 10.5 MHz.

Reliability.
The reliability derived from observations is larger for Q≤4 than for Q>4 in Figures A10 and A11. The reliability is also large during night for this summer data set. The MUF is about 19 MHz around noon for quiet conditions.

The predictions of reliability are too optimistic at the lowest frequencies at night time compared to data. The MUF around noon is predicted too low.

Similarity coefficients.
The best similarity coefficients on the long path are obtained for this data set; for Q=3

the total similarity coefficient is 0.58 and for Q=6, 0.44. The similarity coefficient for each hour around noon is very high, decreasing towards midnight (Figure A12). The similarities for each frequency over all hours are again better than for the short path.

Figure A9   Virtual height of reflection, Kløfta-Alta (1230 km), June/July/August 1991.
Median of data drawn as a continous line. Small dots indicate multipath.
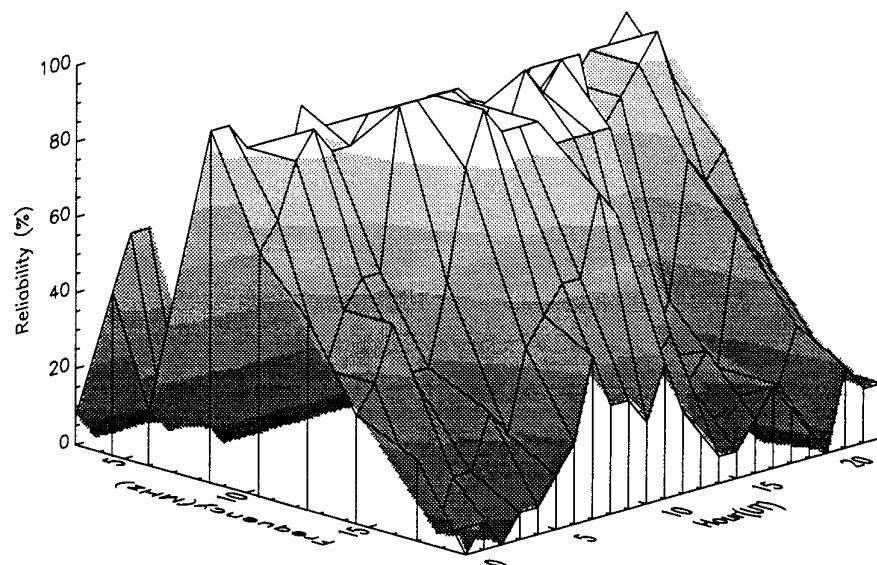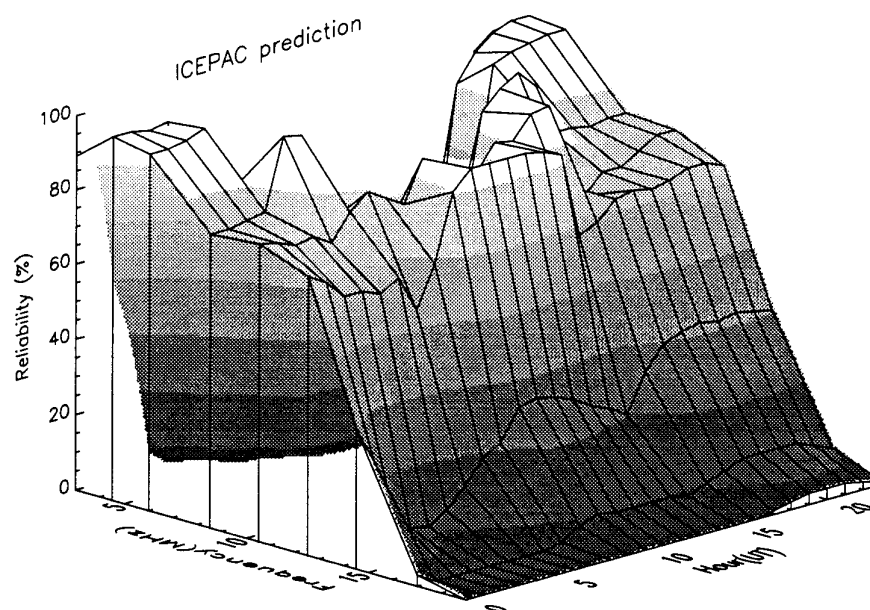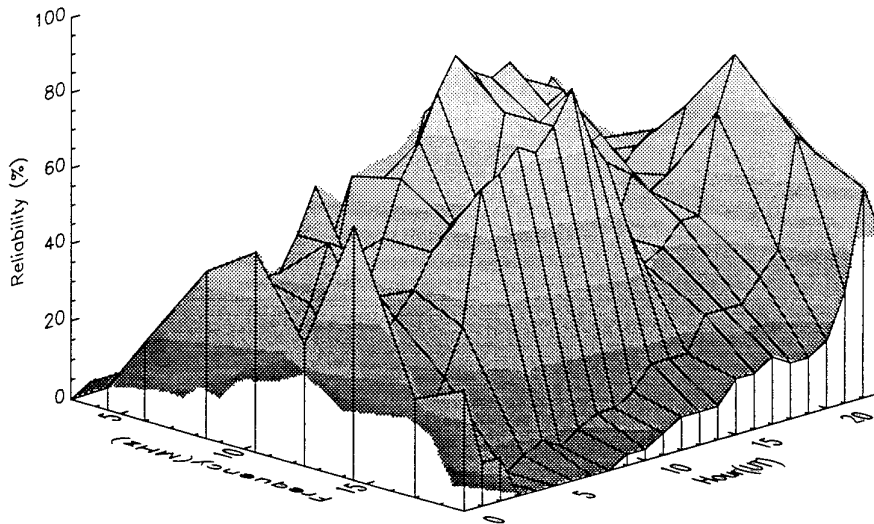Predicted virtual height shown as triangles. SSN=146

Q≤4:

Q=3:

*Figure A10   Reliability of data for June/July/August 1991 above, prediction for July
below (SSN=146). Kløfta-Alta (1230 km)*

Q>4:

Q=6:
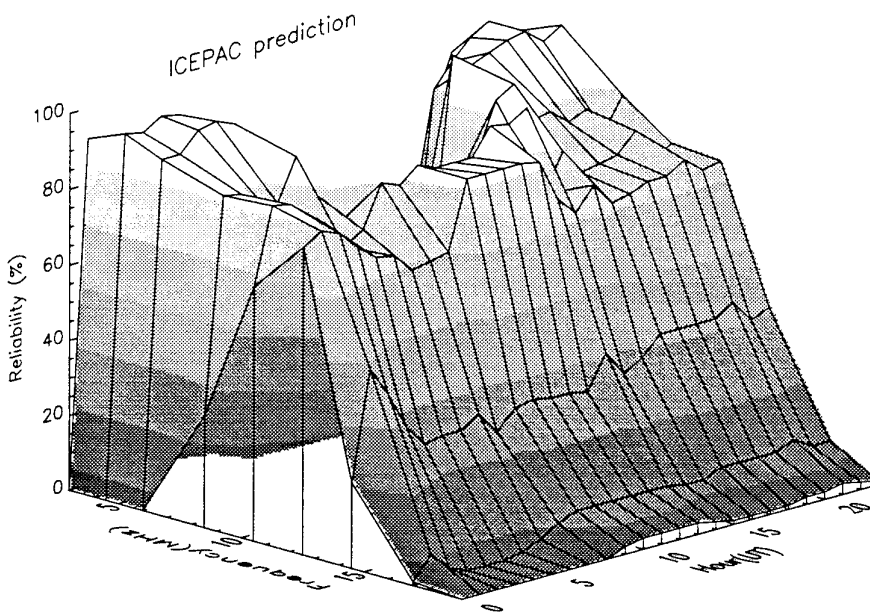
Figure A11   Reliability of data for June/July/August 1991 above, prediction for August below (SSN=147). Kløfta-Alta (1230 km)
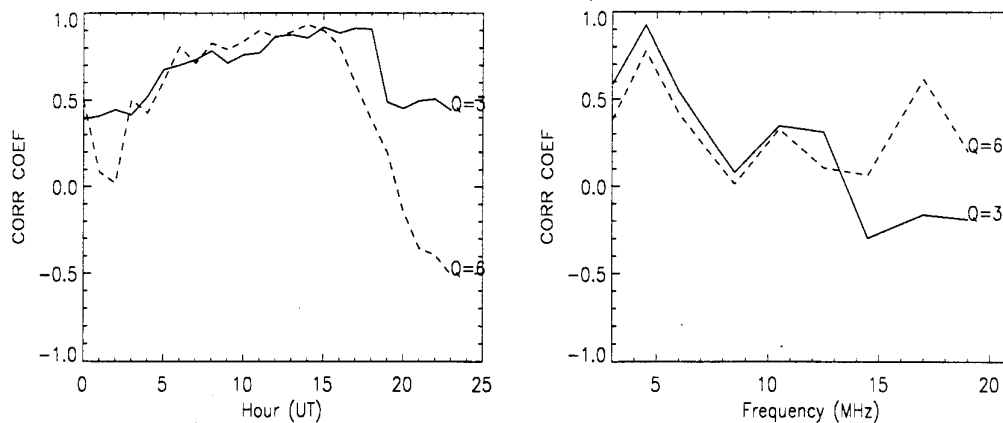
Figure A12   Similarity coefficients (corr coef) between reliability of measured data and reliability predicted by ICEPAC. Kløfta-Alta (1230 km), June/July/August 1991, SSN=146

September/November 1990

We have used 23 quiet days and 14 disturbed days in this data set. Most of the quiet days occured in November, and most of the disturbed days in September, so the predictions for the quiet and disturbed time period are from November and September, respectively. The predictions reflect therefore a small seasonal change.

Virtual height.
Virtual height is displayed in Figure A13. The reflection pattern of the data is similar to the data sets from winter and spring shown previously.

The predictions of virtual height perform better for the "winter" month November (quiet period) than for September. The E-layer reflections at night are nevertheless predicted 40 km too low compared to the data for the quiet period. For September (disturbed period), the same prediction errors are made as for the spring equinox data set.

Reliability.
Reliabilities are shown in Figure A14 and A15. The reliability derived from this data set is larger for the disturbed period than for the quiet period. Otherwise the quiet and disturbed period show the same characteristics. The MUF is more than 19 MHz around noon for quiet conditions.

Similarity coefficients.
The overall similarity coefficients for this data set are 0.43 for Q=3 and 0.49 for Q=6. ICEPAC predicts for November (quiet) similar reliabilities as for the winter data set. For the hours around noon, the very low predicted reliabilities for frequencies 14.5-17 MHz

causes the small similarity coefficients (Figure A16). For September (disturbed), ICEPAC predicts similar reliabilities as for the spring and summer data set. The similarity coefficients between data and predictions are high around noon, but decrease towards midnight. Again, too large reliabilites are predicted for the lowest frequencies around midnight.

Q≤4 (data), Q=3 (predictions)   **Q>4 (data), Q=6 (predictions)**
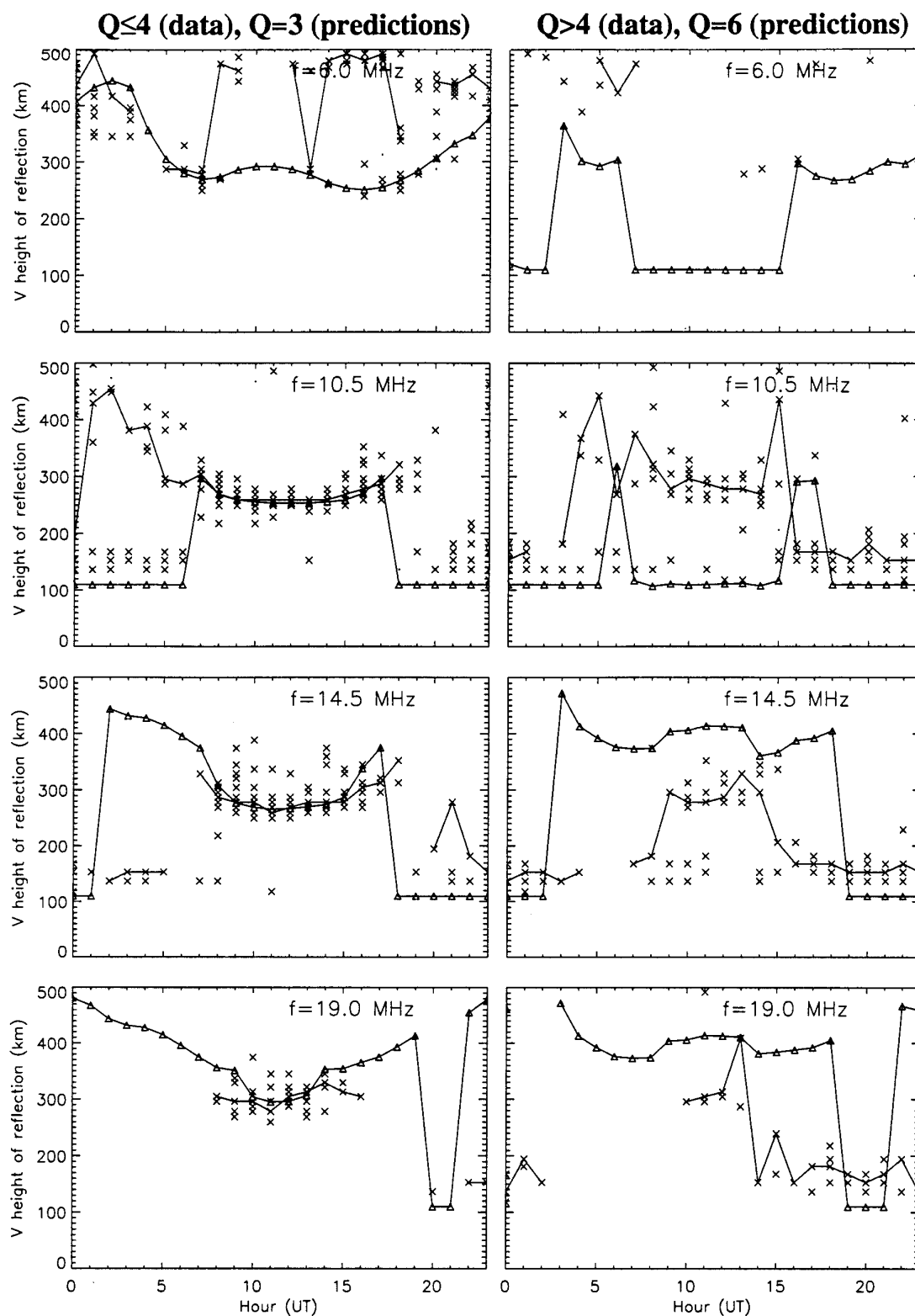
Figure A13   Virtual height of reflection, Kløfta-Alta (1230 km), September/November 1990. Median of data drawn as a continous line. Small dots indicate multipath. Predicted virtual height shown as triangles. SSN=142

Q≤4:
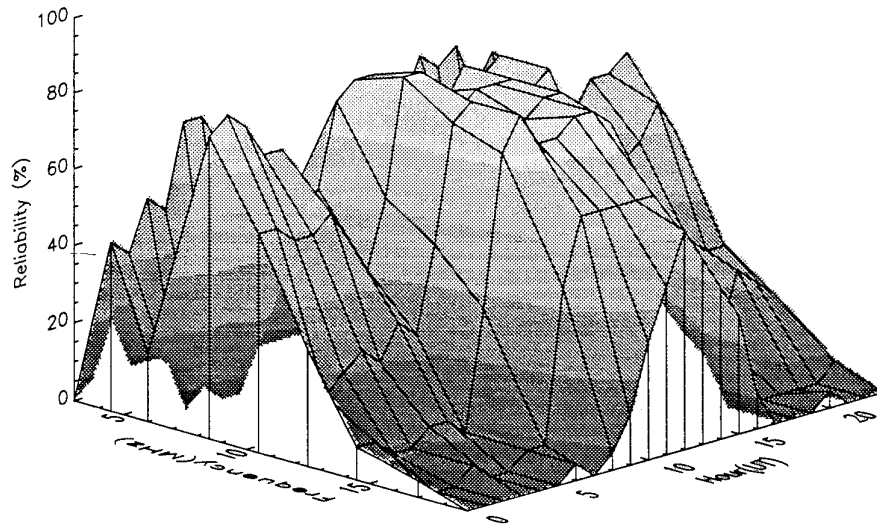
Q=3:
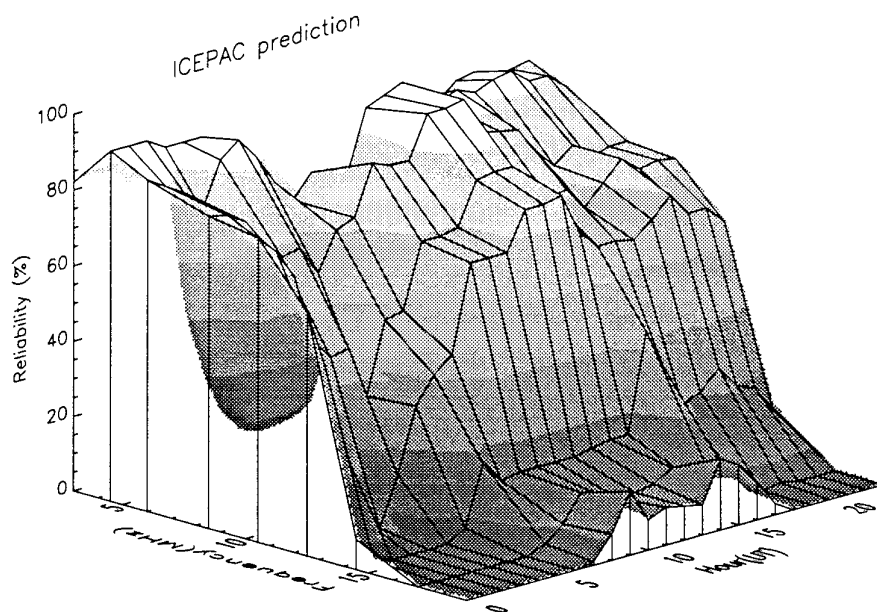
Figure A14   Reliability of data for September/November 1990 above, prediction for
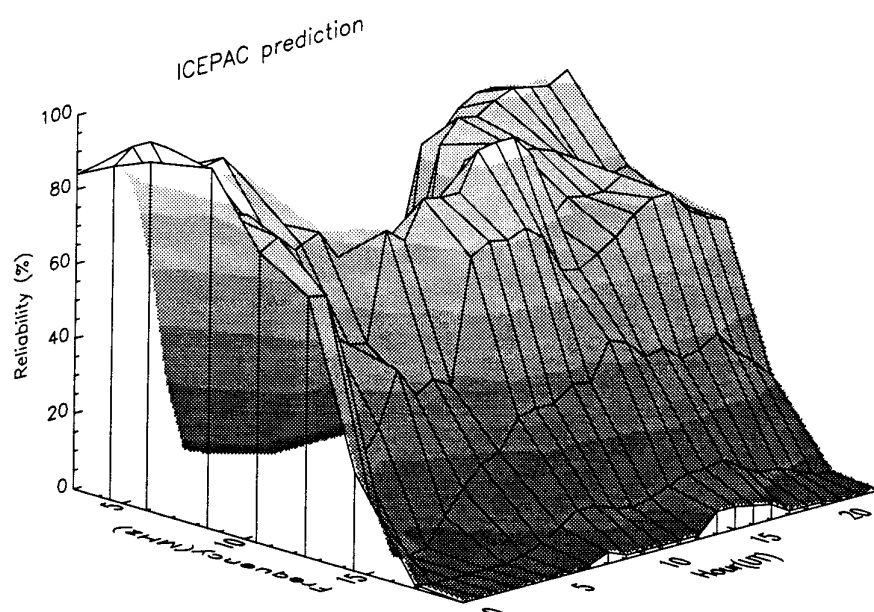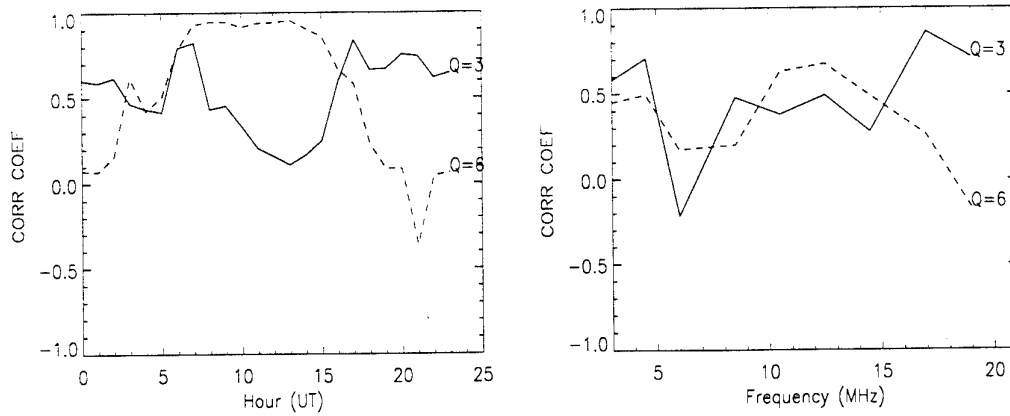*November below (SSN=142). Kløfta-Alta (1230 km)*

Q>4:
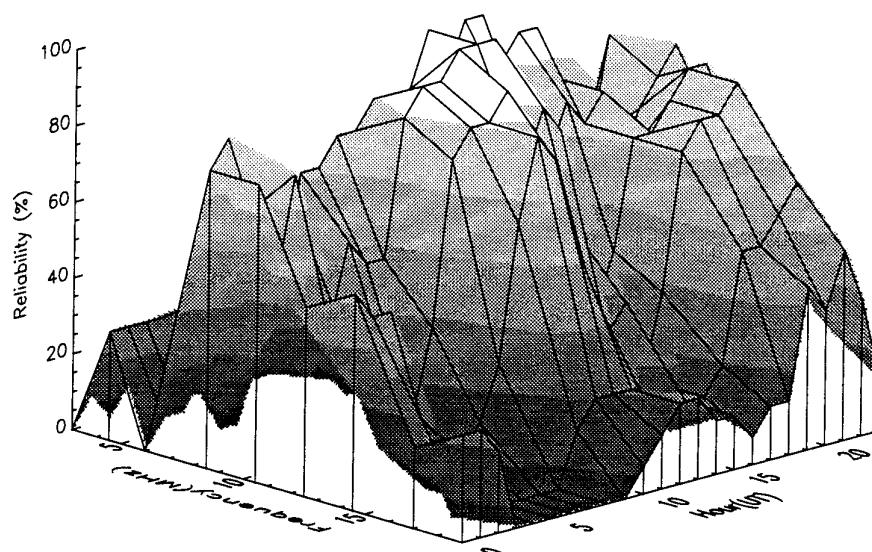
Q=6:

Figure A15   Reliability of data for September/November 1990 above, prediction for
September below (SSN=142). Kløfta-Alta (1230 km)

Figure A16   Similarity coefficients (corr coef) between reliability of measured data and reliability predicted by ICEPAC. Kløfta-Alta (1230 km), September/ November 1990, SSN=142

FORSVARETS FORSKNINGSINSTITUTT
Norwegian Defence Research Establishment
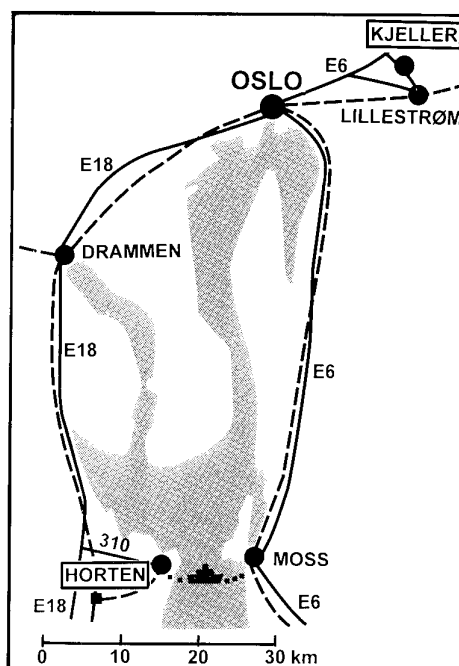
Facts about NDRE:

NDRE is a research establishment reporting directly to Ministry of Defence. Its primary task is to conduct research and development to meet the requirements of the armed forces. It acts as an adviser to the political and military leadership of Norwegian Defence on pertinent issues.

NDRE is a multi-discipline establishment covering such fields as engineering, physics, biology, medicine, economics and political sciences. It co-operates closely with industry and with other institutions, both in Norway and abroad. Is has approximately 500 employees. In addition to the Administration Department there are five divisions.

Publications from NDRE:

NDRE issues a number of technical and scientific publications each year. The publications cover various aspects of the activities. A summary of unclassified publications may be obtained directly from the Library, which also can provide additional information.

Telephone no.: + 47 63 80 71 28   Telefax no.: + 47 63 80 71 59

FORSVARETS FORSKNINGSINSTITUTT
Norwegian Defence Research Establishment